Clustering in bubbly liquids
(formación de agregados en líquidos burbujeantes)

Bernardo Figueroa
Instituto de Investigaciones en Materiales
Universidad Nacional Autónoma de México,
Apdo. Postal 70-360, México D.F. 04510, México

Thesis Advisor: Dr. Roberto Zenit Camacho

July 31, 2006

Contents

Resumen

Se llevaron a cabo experimentos para determinar las condiciones bajo las cuales se presenta la formación de agregados de burbujas ascendentes en agua pura. Se tiene particular interés en flujos cuyo movimiento alrededor de las burbujas puede ser descrito, hasta cierto punto, por medio de la teoría del flujo potencial. Esta teoría es aplicable para el caso de líquidos burbujeantes donde el número de Reynolds es grande, y el número de Weber es pequeño.

Se ha reportado en investigaciones previas que un flujo de burbujas monodisperso a alto número de Reynolds y bajo número de Weber es inestable, pues tiende a reorganizarse en agregados de burbujas (clusters) que muestran una orientación horizontal.

Para observar claramente la formación de agregados proponemos el uso de un canal delgado (parecido a una celda Hele-Shaw). En este canal las burbujas no pueden traslaparse en la dirección de observación, por lo que la identificación de los agregados no puede ser malinterpretada. Se utiliza análisis directo de imágenes digitales para calcular las velocidades y tamaños de las burbujas, así como la formación de los agregados. A pesar de que las paredes afectan el movimiento de las burbujas, el fenómeno de formación de agregados (clustering) ocurre y tiene el mismo comportamiento cualitativo que en un flujo tridimensional.

A pesar de la fuerte influencia de las paredes en el canal delgado, se encontró que efectivamente se forman agregados de burbujas con una tendencia a orientarse en dirección horizontal. La estructura del flujo fué analizada por medio de la distribución radial de probabilidad y la distribución condicional de probabilidad de los ángulos entre centroides de burbujas. Se encontraron evidencias que apoyan la hipótesis de la formación de agregados.

Se investigó experimental y numéricamente el efecto del confinamiento sobre el coeficiente de arrastre de la burbuja fué investigado experimental y numéricamente. Los experimentos con una sola burbuja se realizaron con líquidos no polares, de tal manera que la superficie de la burbuja se pudiese considerar limpia. Se llevaron a cabo experimentos y simulaciones para diferentes números de Reynolds y confinamientos (dados por la relación entre el radio de la burbuja a y la distancia entre paredes R: $s = a/R$). Se mostró que el efecto del confinamiento sobre el coeficiente de arrastre es muy fuerte, y puede llegar a duplicar el correspondiente arrastre de una burbuja no confinada. También se observó que para Re grandes la trayectoria de la burbuja se vuelve inestable, pues se presenta una transición de trayectorias rectilíneas a oscilatorias por encima de cierto número de Reynolds crítico de $O(100)$. Se observa que las burbujas pueden llegar a rebotar en las paredes en algunos casos. Para números de Reynolds debajo del valor crítico, se encontró que los resultados numéricos pueden predecir razonablemente bien el efecto del confinamiento. Las trayectorias oscilatorias dan como resultado un aumento en el arrastre, calculado con la velocidad de ascenso promedio. La inestabilidad de la trayectoria difiere de aquella presente en burbujas no confinadas (*path instability*), pues ahora existe una fuerte influencia de las paredes, la cual se puede explicar como sigue: para Re bajos, las paredes tienen un efecto estabilizador debido a las fuerzas hidrodinámicas de repulsión entre las paredes y la burbuja, mientras que para Re altos, dichas fuerzas cambian de signo, desestabilizando la trayectoria de la burbuja que se mueve entre las paredes. Como resultado de dichas interacciones, el número de Reynolds crítico es menor en el caso confinado que en el caso de inestabilidad de trayectoria para burbujas no confinadas.

Abstract

Experiments were conducted to determine the amount of clustering that occurs in bubbly flows for which the liquid motion can be described, with a certain degree of accuracy, using potential flow theory. A Hele-Shaw-type channel was used in which bubble overlap was avoided. Direct video image analysis was performed to calculate bubbles properties and identify cluster formation. Despite the significant wall influence of this configuration, it was found that bubbles do form aggregates with a statistical horizontal tendency. The bubbles relative positions were also analyzed using the angular conditional probability distribution and radial distribution function. For small radial distances, the bubbles tend to align horizontally, while for larger radial distances between bubbles the angular distribution seems more uniform. The radial probability distribution was also calculated, showing differences with that of randomly distributed bubbles for the same volume fraction.

The effect of confinement on the drag over a gas bubble was investigated both experimentally and numerically. The experiments were performed with non-polar liquids such that the bubble surface could be considered clean; hence, shear free. Single bubble experiments and numerical simulations were performed for different Reynolds numbers Re and the relative confinement distances $s = a/R$, where a is the bubble radius and R the distance between walls. It was found that the effect of confinement on the drag coefficient is very strong and can reach as much as two times the drag of a free rising bubble. It was also observed that for large Re the bubble trajectory became unstable in the sense that oscillations were observed above certain critical Reynolds number of $O(100)$. Bouncing against the walls was observed for some cases. For Reynolds numbers below the critical Re, we found good agreement between experimental and numerical results. Unstable trajectories showed a strong effect on the drag coefficient, which increases by a factor of two in the most confined case. The instability of the trajectory was found to be different from that observed in freely rising bubbles. The influence of the walls can be summarized as follows: for low Re the walls have a stabilizing effect due to the repulsive nature of the lift force between the walls and the bubble. For high Re the lift is attractive, and trajectories become more unstable, compared to the unconfined case.

Chapter 1

Introduction

1.1 Motivation

Multiphase flows can be found in numerous fields in engineering, e.g. aerospace, biomedical, chemical, electrical, environmental, mechanical, nuclear and naval engineering, rocket engines, chemical reactors, contamination spreading, multiphase mixture transport, cavitation, sonoluminescence, ink-jet printing, particle transport in blood, crystallisation, multiphase cooling, fluidized beds, drying of gases, air entrainment in oceans/rivers and anti-icing fluids. The number of papers on multiphase flow is enormous and still growing. The diversity of flow types makes a general description almost impossible. This makes fundamental research necessary. Especially, controlled experiments are needed for a better physical understanding and as test cases for numerical and theoretical work [17].

Recently, there have been significant advances in the theory of inertial suspensions, in particular those that describe the rheology of bubble suspensions. For the case of a bubbly suspension in which the Reynolds number is large and the Weber number is small, a complete set of governing equations can be composed from first principles [27, 65]. The extent of the validity of these theories could only be assessed if comparisons with detailed experimental measurements are performed.

A distinctive feature that has been observed in the models and simulations of bubbly liquids in potential flow is the appearance of horizontally oriented clusters of bubbles [61, 63]. In a recent investigation Zenit *et al.* [80] were able to observe the formation of clusters experimentally. By performing a simple image analysis of images of a nearly mono-dispersed gravity driven bubbly flow, they were able to measure a preference for the bubbles to orient horizontally. The strength and size of the clusters was much more modest than those reported in the computer simulations. Since the image analysis was performed on two-dimensional images from three dimensional flows, there was some uncertainty about extent of the detected clustering. Other effects not considered in the potential flow formulation, such as the appearance of the bubble path instability [45] or the cluster induced agitation [80], could prevent or limit the formation of clusters.

In this investigation we used an alternative experimental technique to observe and measure the extent of clustering that appears in these type of bubbly flows. Since the

geometry of the experiment involves bubble-wall interactions, it is important to evaluate the effect they have on the flow parameters and field, such as the drag coefficient and bubble trajectories. We studied these effects through theoretical modeling and numerical simulations.

1.2 Historical Framework

The study of the hydrodynamics of bubbly flows has a long history, which cannot be totally aquainted here for space and time limitations. The theoretical difficulties arising from the motion of many bodies in a fluid was first discussed by Stokes, in a paper read before the Cambridge Philosophical Society in 1843, entitled *On some cases of Fluid Motion* [66], where the author, amongst other problems, considered the case of the motion of two spheres in a perfect liquid, and the limiting case of a sphere moving in the presence of a plane. Many other authors should be mentioned, such as Thomson and Tait [68], Kirchhoff [29], Basset [2], or Lamb[36], just to mention a few contributors.

Referring to the calculation of hydrodynamic forces and interactions, the work of Levich [42, 43] and Moore [47, 48] is very important. Based on the boundary layer assumptions given by Prandtl and Blasius [52, 7], Levich considered that some external flows around slender bodies (at high Reynolds numbers) are essentially irrotational and that the drag could be calculated from the dissipation in a nearly inviscid flow, establishing an analytic expression for the drag coefficient of a spherical bubble. Moore analysed the problem of steady uniform flow past a spherical bubble and showed that the velocity field to leading order can be considered to be irrotational or potential everywhere in the liquid, and that the correction to this is $O(Re^{-1/2})$ in the boundary layer of thickness $O(Re^{-1/2})$ near the surface of the bubble. He also showed that the wake behind the bubble is small, of diameter $O(Re^{-1/4})$, in contrast with the flow past a solid sphere for which there is a boundary-layer separation causing a finite region of recirculation.

Unfortunately, only a small number of bodies can be analytically solved by the mathematical methods given by the aforementioned authors compared to real bubbly flows.

Attempts had been made to develop an approximate theory for bubbly liquids, based on pair-wise interactions that can be described analytically from potential theory [5, 33, 34, 54, 40], and then extrapolated by means of statistical analysis to describe the behavior of a suspension of bubbles (consisting of a large number of bubbles in a liquid).

There is a special case of an inertial suspension that is particularly amenable to theoretical analysis: a suspension of surfactant-free, spherical, high-Reynolds-number bubbles. In this case, the vorticity produced by the bubble motion is small [47] and the fluid velocity can be expressed as the gradient of a potential obtained from solving Laplace's equation.

It is possible to derive, from first principles, equations of motion for this type of bubble suspension [61, 27, 5]. The potential flow approximation is applicable in the limits of high bubble Reynolds number an low bubble Weber number. Comparison between measured rise velocities for gas bubbles in water and theoretical predictions indicate that the potential flow theory for spherical bubbles is reasonably accurate for bubble diameters of about

1 mm (in water) and the agreement between theory and experiment can be improved by including the effects of bubble deformation [48, 18]. Although the development of these theories represents a significant step towards the understanding of inertial suspensions, the extent of their applicability must be determined by comparison with experimental measurements [80].

Another approach is to perform simulations based on these potential analytical models, where a large number of bubbles is considered, and then evaluate the average properties of such suspensions. As already mentioned, the appearance of horizontally oriented clusters of bubbles have been observed in such simulations[61, 63].

A large amount of work has been published on the subject recently, and a complete description of it would be too extensive. A summary of the research papers mostly related to this work is presented next.

1.3 Related Work

Biesheuvel and Van Wijngaarden [5] studied the problem of the interaction between two spheres in a perfect liquid, as an element of the more general theory addressed recently by Van Wijngaarden [71]. They used twin spherical expansions in Legendre polynomials to solve the Laplace equation, with boundary conditions given by two bubbles immersed in a liquid that is instantaneously accelerated. The trajectories described by their separation vector in the course of time were numerically computed with use of the analytically obtained flow potential. An approximate theory was developed, and qualitative properties of these trajectories were obtained. The authors used these results to derive an approximate theory for the regions of hydrodynamic attraction and repulsion between two adjacent bubbles, and compared these numerical results. These results predict that an initially random distributed bubbly flow will continue to be so after t=0, and the order of this effect would be $O(a/R)^9$ (where a is the bubbles radius and R is the distance along their line centers).

Kumaran and Koch [33] also solved the potential problem of two bubbles with twin spherical expansions. They considered two bubbles of different radius moving at given velocities, and used the potential flow solution to calculate the pressure on the surface of each bubble with the Bernoulli equation. The pressure was used to evaluate the forces and acceleration, which was found to decrease as $O(a_i/R)^4$. They also calculated the mean-square fluctuating velocity in a uniform suspension and the hydrodynamic diffusivities in a nonuniform one, for interactions where collisions do not occur, by performing an ensemble average over pair interactions. The pair averaging procedure is valid for dilute suspensions ($\alpha << 18/Re$, where α is the volume fraction of the bubbles and Re is the Reynolds number based on the bubble radius and the terminal velocity).

Smereka [63] studied the motion of spherical bubbles in a box containing a perfect liquid with periodic boundary conditions. The author performed Lyapunov stability analysis to conclude that, when the bubbles have approximately the same velocity and are arranged in such a way so as to minimize the effective conductivity of a composite material (where

the bubbles are treated as insulators), asymptotic stability is achieved with the addition of gravity and liquid viscosity. This suggests that a randomly arranged configuration of bubbles, all with approximately the same velocity, cannot be stable. Explicit equations of motion for two bubbles are deduced using Rayleigh's method for solving Laplace's equation in a periodic domain. The results are extended for more than two bubbles by considering pairwise interactions. Numerical simulations with zero gravity and viscosity show that the bubbles form clusters if they are initially randomly arranged with identical velocities. The clustering is inhibited, however, if the initial velocities are sufficiently different. The variance of the bubbles' velocities is observed to act like a temperature; a lesser amount of clustering occurs with increasing temperature. When the effect of viscosity and gravity are considered, the clustering phenomenon is again evidenced.

Sangani and Didwania [61] performed similar dynamic simulations of bubbles rising through an irrotational liquid, for Reynolds number (also based on the radius and terminal speed of the bubbles) large compared to unity, and small Weber number (which is the ratio of inertial to surface tension forces). The viscous force is estimated from the rate of viscous energy dissipation, following the methodology given by Levich [42, 43]. It is assumed that the bubbles do not coalesce, but rather bounce instantaneously, conserving momentum and the kinetic energy of the system. The flow of the liquid is determined by solving the many-bubble interaction problem exactly. It is shown that the random state of bubbly liquids under these conditions is unstable and that the bubbles form aggregates in planes transverse to gravity. This instability results primarily from the nature of inertial interaction among pairs of bubbles, and it is also noticed that the presence of viscous forces facilitates the process.

Yurkovetsky and Brady [79] studied the dynamics of bubbles at high Reynolds numbers from the viewpoint of statistical mechanics. They described the cluster formation as a phase transition (from the so called *dispersed* to the *condensed* phase), depending on parameters like the distance between bubbles, the bubble temperature (analog to the granular temperature in granular flow) and volume fraction, that determine the transition or cluster appearance. Individual bubbles are treated as dipoles in potential flow. A virtual mass matrix of the system of bubbles was introduced (which depends on the instantaneous positions of the bubbles), and was used to calculate the energy of the bubbly flow as a quadratic form of the bubbles' velocities. The energy was shown to be the system's Hamiltonian and was used to construct a canonical ensemble partition function. An effective bubble temperature -a measure of the relative importance of the bubbles' relative to collective motion- was derived with the help of an impulse-dependent partition function. Two effective potentials were shown to operate: one due to the mean motion of the bubbles, which dominates at low bubble temperatures, (in that case it leads to grouping in flat clusters normal to the direction of the collective motion), while the other, temperature-invariant, is due to the bubbles' position-dependent virtual mass and results in their mutual repulsion. Numerical evidence was presented for the existence of the effective potentials, the condensed and dispersed phases, and a phase transition.

Legendre and Magnaudet [40] investigated, by solving numerically the full Navier-

Stokes equations, the interactions between two bubbles immersed in a viscous incompressible fluid, over a wide range of Reynolds number ($0.02 \leq Re \leq 500, Re$ being based on the bubble diameter and rise velocity), and separation distance S ($2.25 \leq S \leq 20$, the distance between the bubbles centres normalized by the bubble radius). The magnitude and sign of the drag and lift forces (among other quantities) were analyzed; in particular the latter is compared with analytical expressions available in the potential flow limit and in the limit of low-but-finite Reynolds number. Based on the numerical results and the aforementioned expressions, conditions for the sign of the transverse force are established, as well as empirical expressions for the drag and lift forces in the moderate-to-large Reynolds number regime.

Tzeng et al [69] used a 2-D column, similar to that proposed for this study, to investigate the macroscopic flow structures and mechanisms of liquid circulation. They found that there are four distinct flow regions for high gas flow rates regimes, namely central plume region, fast bubble flow region, vortical flow region and descending flow region. Their study showed that similar flow regions exist in the 2-D and 3-D bubble columns. One interesting feature of such regions is that spiral motion in 3-D corresponds to a wave-like motion in 2-D that can be characterized a wavelength and frequency. Lin, Reese, Hong and Fan [44] conducted experiments to quantify the macroscopic hydrodynamic characteristics of various scale 2-D bubble columns, which include dispersed and coalesced bubble regimes. The latter was found to be characterized by two flow conditions (referred to as 4- and 3-region flow) with coherent flow structures. The demarcations of these regimes is directly related to gas holdup, and column width. A qualitative description of the coalesced regime transition was given, and the vortex size, wavelength and frequency importance was discussed. The instantaneous and time-averaged liquid velocity and holdup profiles provided by a PIV system were presented, and comparison of computational results were evaluated.

1.4 Objectives

The objectives of this project are:

- To propose a new experimental technique to observe and measure the extent of clustering that appears in this type of bubbly flows.
- To demonstrate statistically (from the experiments data) that horizontal clusters do form, as predicted by potential flow theory.
- To solve the potential flow problem of a bubble confined between two parallel walls in order to evaluate the drag coefficient and the bubble-wall attraction.
- Perform direct numerical simulations to corroborate the theoretical results and validate them with the experimental data.
- Study the effect of confinement on the drag and stability of a single bubble.

1.5 Relevance

Flows of gas-liquid dispersions occur in a variety of industrial and natural processes, and therefore the problem of describing them quantitatively is relevant from the viewpoint of engineering and basic science [80]. The problem of obtaining a set of averaged equations that govern the flow of liquids in which the bubbles are uniformly dispersed, and to predict the conditions that determine its stability, is relevant to many aspects of applied and theoretical studies in many fields of human knowledge.

From the basic research point of view, it would be very important to corroborate the occurrence of the clustering phenomenon because it would confirm that the high Reynolds number description of hydrodynamic interactions is appropriate for certain flow conditions, which are to be also established using experimental and theoretical analysis.

On the other hand, from a more general point of view, the formation of clusters would contribute to the generation of velocity fluctuations in the flow, enhanced interactions that would lead to instabilities and a transition to a new flow regime. This new regime cannot be analyzed by the potential pairwise bubble interactions previously addressed. This is precisely the transition form one monodisperse bubbly flow to a different regime where the fluctuations provoked by these clusters have a much wider extent, generating vorticity and instabilities that may lead the way to the so called *condensed phase* (Yurkovetsky [79]).

Another aspect of the flow to be brought to mind is coalescence, which is of crucial importance in the transition [44], since it generates important velocity and pressure fluctuations that result in the formation of polidisperse bubbles and vortical regions that comprise complex macroscopical flow regimes. This fact justifies our attention to hydrodynamic attractive forces, the clustering phenomenon, and their importance in bubbly flow research.

1.6 Important variables

The regimes of flow, as mentioned earlier, can be characterized by a set of dimensionless numbers. The relevant variables in bubbly flow analysis are ρ_f, μ_f, σ, d, g, v_b and L which are the continuous phase density and viscosity, surface tension, characteristic distance, gravity and velocity (like rise terminal velocity of a bubble) and the distance between walls, respectively. If the equations of motion are expressed in terms of dimentionless variables, suitable dimensional analysis leads to four independent parameters:

$$Re = \frac{\rho_f v_b d_b}{\mu_f} \tag{1.1}$$

$$M = \frac{g\mu^4}{\rho\sigma^3} \tag{1.2}$$

$$Eo = \frac{g\Delta\rho d^2}{\sigma} \tag{1.3}$$

$$\Pi_4 = \frac{d}{L} \tag{1.4}$$

These are the combined Reynolds, Morton, Eötvos and size ratio numbers. These numbers can be operated to obtain other more commonly used dimensionless numbers e.g.

$$We = (\frac{M}{Eo})^{1/2} Re^2 = \frac{\rho v_b^2 d_b}{\sigma} \tag{1.5}$$

$$Ca = (\frac{M}{Eo})^{1/2} Re = \frac{\mu v_b}{\sigma} \tag{1.6}$$

which are the Weber and Capilary numbers. We represents the ratio between the inertial and surface tension forces, Ca is the comparison between viscous and surface tension forces. The Weber number is very important since it establishes conditions for the bubbles to keep their spherical shape. When the Weber number is small, surface tension forces are dominant and the bubbles remain nearly spherical. Also, both We and Re determine the transition from linear to oscilatory trajectory [18].

Another effect that can arise in this type of experiments is *coalescence*. This is an important phenomenon that affects the overall behavior of the flow, since larger bubbles have a higher terminal velocity and a large wake that affects other bubbles downstream. This situation can be avoided to some extent by adding a small amount of salt[80], causing an ionic short range repulsion effect to counter-act coalescence (without changing surface tension) and maintaining the monodispersity of the flow. In our case, the salt utilized for this purpose was Magnesium sulfate ($MgSO_4$ 5% solution). Additionally, the liquid must be clean, specially from *surfactants*, which are substances consisting of large molecules with hydrophobic and hydrophilic ends that cause surface tension gradients on the surfaces. This effect, caused by small amounts of grease, oil, or any other mineral or organic contaminant, must be carefully avoided during the experiments.

Another important variable that should be mentioned is the volume fraction α. This is the ratio between the total gas volume and the total liquid volume, and as mentioned earlier, it has been recognized in various experimental[69] and theoretical[70] works to be of fundamental importance in liquid-gas mixtures phenomena.

Chapter 2

Theoretical Framework

2.1 Conservation Laws and Constitutive Equations

The purpose of this section is establish the set of equations which results from invoking the physical laws of conservation of mass, momentum, and energy. The point of view adopted here is based on the *continuum* concept, which assumes that the fluid consists of continuous matter. At each point of this (continuous) fluid, a unique value of the velocity, pressure and density (*field variables*) is assumed. This matter is then required to obey the conservation laws that give rise to a set of differential equations governing the variations of the aforedmentioned variables in space and time.

There are two choices for the reference frame adopted, before the developement of any conservation equation: the Eulerian and the Lagrangian coordinates.

In the eulerian framework the independent variables are the spatial coordinates x, y and z, and time t. This is the familiar framework in which most problems are solved. In order to derive the basic conservation equations in this framework, attention is focused on the fluid which passes through a control volume fixed in space. In the Lagrangian approach, attention is fixed on a particular mass of fluid as it flows. In this reference frame x, y z and t are no longer independent variables since, as soon as an initial time and position of the particule are specified, the coordinate changes $(x-x_0)$, $(y-y_0)$, and $(z-z_0)$ are uniquely determined, so x, y, z and t are no longer independent. The independent variables in the Lagrangian system are x_0, y_0, z_0 and t, where the first three components define the position of the particule at a given time t_0.

The choice of which coordinate system to employ is largely a matter of pragmatism, since it depends on the nature of the problem. For the purpose of deriving the conservation principles, the Lagrangian point of view will be adopted, since following the same fluid particules in a flow makes it easier to treat them as a thermodynamical system, and apply the conservation of principles to them as a whole. Nevertheless, the Eulerian system is the preferred one for solving the majority of problems.

2.1.1 Material Derivative

Consider α to be any field variable, such as the density or the temperature. Consider now a fluid particule P moving through the fluid: If it is followed for a short period of time δt as it flows, its position will change by amounts δx, δy and δz while its value of α will change by an amount $\delta\alpha$. The independent variables in this case are the original position given by x_0, y_0, z_0 and t, thus, the change in α during the time δt is given by:

$$\delta\alpha = \frac{\partial\alpha}{\partial t}\delta t + \frac{\partial\alpha}{\partial x}\delta x + \frac{\partial\alpha}{\partial y}\delta y + \frac{\partial\alpha}{\partial z}\delta z \tag{2.1}$$

dividing the above equation by the time difference δt, and taking the limit when $\delta t \to 0$ this expression becomes:

$$D\alpha = \frac{\partial\alpha}{\partial t} + \frac{\partial\alpha}{\partial x}u + \frac{\partial\alpha}{\partial y}v + \frac{\partial\alpha}{\partial z}w \tag{2.2}$$

where u, v and w are the velocities in the x, y and z directions. Alternatively, using the index summation convention, the tensor form may be written as:

$$\frac{D\alpha}{Dt} = \frac{\partial\alpha}{\partial t} + u_k\frac{\partial\alpha}{\partial x_k} \tag{2.3}$$

2.1.2 Conservation of Mass

Consider a specific mass of fluid whose volume V is arbitrarily chosen. If no mass generation processes are taking place, this given control mass will remain unchanged; if the mass contained in it is $\int_V \rho dV$, then:

$$\frac{D}{Dt}\int_V \rho dV = \int_V [\frac{\partial\rho}{\partial t} + \frac{\partial}{\partial x_k}(\rho u_k)]dV = 0 \tag{2.4}$$

Since the volume V was arbitrarily chosen, the only way in which the above equation can be satisfied for all possible choices of V is for the integrand to be zero. Then the equation expressing conservation of mass becomes:

$$\frac{\partial\rho}{\partial t} + \frac{\partial}{\partial x_k}(\rho u_k) = 0 \tag{2.5}$$

This equation is usually referred to as the *continuity equation*, since it is a partial differential equation of the velocity. One mixed form of equation 2.5 is useful for the derivation of other conservation principles, and will be given here as

$$\frac{D\rho}{Dt} + \rho\frac{\partial u_k}{\partial x_k} = 0 \tag{2.6}$$

One example of this is an incompressible fluid flow (or a stratified flow, with constant-density planes or lines) for which:

$$\frac{\partial u_k}{\partial x_k} = 0 \tag{2.7}$$

2.1.3 Conservation of Momentum

The principle of conservation of momentum is an application of Newton's second law of motion to an element of the fluid. Consider a given mass of fluid in a Lagrangian frame of reference: it is stated that the rate of change of momentum of the fluid mass is equal to the net external force acting on it. The external forces acting on a mass of the fluid may be classed as either body forces, such as gravitational or electromagnetic forces, or surface forces, such as pressure or viscous stresses.

$$\frac{D}{Dt}\int_V \rho\vec{u}dV = \int_S \vec{P}dS + \int_V \rho\vec{f}dV \tag{2.8}$$

The surface force will be given by $P_j = \sigma_{ij}n_j$, where i is summed from 1 to 3. That is, in tensor notation the equation expressing conservation of momentum becomes:

$$\frac{D}{Dt}\int_V \rho\vec{u}dV = \int_S \sigma_{ij}n_j dS + \int_V \rho\vec{f}dV = \int_V \left\{\frac{\partial}{\partial t}(\rho u_j) + \frac{\partial}{\partial x_k}(\rho u_j u_k)\right\} dV \tag{2.9}$$

The surface integral may be converted to a volume integral by use of Gauss theorem as given in Appendix A:

$$\int_S \sigma_{ij}n_j dS = \int_V \sigma_{ij}dV \tag{2.10}$$

Substitution of 2.10 into 2.9 gives:

$$\rho\frac{\partial u_j}{\partial t} + u_j\frac{\partial \rho}{\partial t} + u_j\frac{\partial}{\partial x_k}(\rho u_k) + \rho u_k\frac{\partial u_j}{\partial x_k} = \frac{\partial \sigma_{ij}}{\partial x_i} + \rho f_j \tag{2.11}$$

The second and third terms on the left-hand side of this equation are now seen to sum zero, since they amount to the continuity equation 2.5 multiplied by the velocity u_j. With this simplification, the momentum equation becomes:

$$\rho\frac{\partial u_j}{\partial t} + \rho u_k\frac{\partial u_j}{\partial x_k} = \frac{\partial \sigma_{ij}}{\partial x_i} + \rho f_j \tag{2.12}$$

The first term is the familiar temporal acceleration term, while the second term is a convective acceleration and accounts for local accelerations (around obstacles, etc.) even when the flow is steady. Note also that this second term is nonlinear, since the velocity appears quadratically. On the right side of equation 2.12 the forces that are causing these accelerations appear. The tensor σ_{ij} is the surface stress tensor.

2.1.4 Conservation of Energy

The conservation of energy amounts to an application of the first law of thermodynamics to a fluid element as it flows. Althoug a specified mass of fluid in a Lagrangian frame of reference may be considered to be a thermodynamic system, it is, in general, never at rest and therefore never in equilibrium. However, in the thermodynamic sense, a flowing fluid is seldom far from a state of equilibrium, and the apparent difficulty may be overcome by considering the instantaneous energy of the fluid to consist of two parts

intrinsic or internal energy and kinetic energy. That is, when applying the first law o thermodynamics, the energy referred to is considered to be the sum of the internal energy per unit mass e and the kinetic energy per unit mass $\frac{1}{2}\vec{u}\cdot\vec{u}$. In this way the modified form of the first law of thermodynamics which will be applied to an element of the fluid states that the rate of change of the total energy of the fluid as it flows is equal to the sum o the rate at which work is being done on the fluid by external forces and the rate at which heat is being added by conduction.

The total energy of this mass of fluid per unit volume is $\int_V(\rho e+\frac{1}{2}\vec{u}\cdot\vec{u})dV$. The rate of change of this quantity is equal to the sum of the work done on the fluid by surface and volume forces, minus the heat leaving the surface area per unit time:

$$\frac{D}{Dt}\int_V(\rho e+\frac{1}{2}\vec{u}\cdot\vec{u})dV=\int_S\vec{u}\cdot\vec{P}dS+\int_V\vec{u}\cdot\rho\vec{f}dV-\int_S\vec{q}\cdot\vec{n}dS \tag{2.13}$$

Converting the two surface integrals into volume integrals, it is possible to exploit the arbitrariness of V to obtain a differential equation only.

$$\int_S\vec{u}\cdot\vec{P}dS=\int_S u_j\sigma_{ij}n_i dS = \int_V\frac{\partial}{\partial x_i}(u_j\sigma_{ij})dV \tag{2.14}$$

$$\int_S\vec{q}\cdot\vec{n}dS=\int_S q_j n_j dS = \int_V\frac{\partial q_j}{\partial x_j}dV \tag{2.15}$$

Having converted each term to volume integrals, the conservation equation may be considered to be of the form $\int_V[\cdot]dV=0$, where the choice of V is arbitrary. Then the quantity inside the brackets in the integrand must be zero, which results in the following differential equation:

$$\frac{\partial}{\partial t}(\rho e+\frac{1}{2}u_ju_j)+\frac{\partial}{\partial x_k}[(\rho e+\frac{1}{2}u_ju_j)u_k]=\frac{\partial}{\partial x_i}(u_j\sigma_{ij})+u_j\rho f_j-\frac{\partial q_j}{\partial x_j} \tag{2.16}$$

Expanding the first and second terms of the left side of the last equation, replacing the quantity $\frac{\partial}{\partial x_k}(\rho u_k)$ by $-\partial\rho/\partial t$ in view of the continuity equation 2.5, and noting that

$$\frac{\partial}{\partial x_i}(u_j\sigma_{ij})=u_j\frac{\partial\sigma_{ij}}{\partial x_i}+\sigma_{ij}\frac{\partial u_j}{\partial x_i} \tag{2.17}$$

The expression that states conservation of energy becomes:

$$\rho\frac{\partial e}{\partial t}+\rho u_k\frac{\partial e}{\partial x_k}+\rho u_j\frac{\partial u_j}{\partial t}+\rho u_ju_k\frac{\partial u_j}{\partial x_k}=u_j\frac{\partial\sigma_{ij}}{\partial x_i}+\sigma_{ij}\frac{\partial u_j}{\partial x_i}+u_j\rho f_j-\frac{\partial q_j}{\partial x_j} \tag{2.18}$$

Now it can be seen that the third and fourth terms on the left-hand side are canceled by the first and third terms on the right hand side, since these terms collectively amount to the product of u_j with the momentum equation 2.12. Thus the equation which expresses conservation of thermal energy becomes:

$$\rho\frac{\partial e}{\partial t}+\rho u_k\frac{\partial e}{\partial x_k}=\sigma_{ij}\frac{\partial u_j}{\partial x_i}-\frac{\partial q_j}{\partial x_j} \tag{2.19}$$

This equation is known simply as the *energy* equation, and is a balance of thermal energy. The left hand represents the rate of change of internal energy, the first term being the temporal change while the second is due to local convective changes caused by the fluid flowing from one area to another. The entire right-hand side represents the cause of the change in internal energy. The first of these terms is the conversion of mechanical energy into thermal energy due to the action of the surface stresses (part of it may be reversible). The final term in the equation represents the rate at which heat is being added by conduction from outside.

2.1.5 Discussion of conservation equations

The basic conservation laws (2.5, 2.12 and 2.19), represent five scalar equations which the fluid properties must satisfy as it flows. The continuity and energy equations are scalar, while the momentum equation is a vector equation which represents three scalar equations. Two equations of state may be added to bring the number of equations up to seven, but our basic conservation laws have introduced seventeen unknowns. These are the scalars ρ and e, the density and the internal energy, respectively; the vectors u_j and q_j, the velocity and heat flux, respectively, each vector having three components; and the stress tensor σ_{ij}, which has, in general, nine independent components.

In order to obtain a complete set of equations, the stress tensor σ_{ij} and the heat-flux vector q_j must be further specified. This leads to the so-called *constitutive equations* in which the stress tensor is related to the deformation tensor and the heat-flux vector is related to temperature gradients. Although the latter relation is very simple, the former is quite complicated and requires physical interpretation of certain tensor quantities.

2.1.6 Equations of motion

The simplest non-trivial case of a stress-strain constitutive relation is the Newtonian fluid, where the deformation-rate tensor is linearly related to the stress tensor in an isotropic material:

$$\sigma_{ij} = -p\delta_{ij} + \lambda\delta_{ij}\frac{\partial u_k}{\partial x_j} + \mu(\frac{\partial u_i}{\partial x_j} + \frac{\partial u_j}{\partial x_i}) \tag{2.20}$$

where σ is the stress tensor, x_k is the position vector and u_i the velocity. The coefficients λ and μ must be determined experimentally. The latter is the dynamic viscosity, which is the proportionality factor between the shear stress and the velocity gradient in a simple shear flow ($\sigma_{12} = \mu\frac{du_1}{dx_2}$). The parameter λ is usually referred to as the *second viscosity coefficient*, and is related to the *The bulk viscosity* K through the linear combination $K = \lambda + \frac{2}{3}\mu$. The parameter K relates the difference between the thermodynamic pressure and the mechanical pressure to the divergence of the velocity vector ($p - \bar{p} = K\frac{\partial u_k}{\partial x_k}$).

Equation 2.20 arises from the observation of common fluids behavior. Careful experiments have been carried out that corroborate this hypothesis for many common fluids such as water (Poiseuille [51]), glycerine and many lubricant oils. This behavior can be summarized as follows:

1. When the fluid is at rest, the stress is hydrostatic and the pressure exerted by the fluid is the thermodynamic pressure

2. The stress tensor is linearly related to the deformation-rate tensor

3. Since there is no shearing action in a solid-body rotation of the fluid, no shear stresses will act during such a motion

4. There are no preferred directions in the fluid, so that the fluid properties are point functions

Item (2) can be inferred from suitable experiments, and is due to Newton, who established it in his **principia**: *BOOK II. OF THE MOTION OF BODIES (1687) "The resistance of sphærical bodies in fluids arises partly from the tenacity, partly from the attrition, and partly from the density of the medium. And that part of the resistance, which arises from the density of the fluid, is, as I said, in a duplicate ratio of the velocity, the other part, which arises from the tenacity of the fluid, is uniform, or as the moment of the time:..."*.

When the equation of conservation of momentum is combined with the constitutive relation for stress in a newtonian fluid, the Navier-Stokes equations are obtained. Next the complete set of differential equations that govern the motion of a Newtonian fluid are presented:

$$\frac{\partial \rho}{\partial t} + \frac{\partial}{\partial x_k}(\rho u_k) = 0 \tag{2.21}$$

$$\rho\frac{\partial u_j}{\partial t} + \rho u_k \frac{\partial u_j}{\partial x_k} = -\frac{\partial p}{\partial x_j} + \frac{\partial}{\partial x_j}(\lambda \frac{\partial u_k}{\partial x_k}) + \frac{\partial}{\partial x_i}[\mu(\frac{\partial u_i}{\partial x_j} + \frac{\partial u_j}{\partial x_i})] + \rho f_j \tag{2.22}$$

$$\rho\frac{\partial e}{\partial t} + \rho u_k \frac{\partial e}{\partial x_k} = -p\frac{\partial u_k}{\partial x_k} + \frac{\partial}{\partial x_j}(k\frac{\partial T}{\partial x_j}) + \lambda(\frac{\partial u_k}{\partial x_k})^2 + \mu(\frac{\partial u_i}{\partial x_j} + \frac{\partial u_j}{\partial x_i})\frac{\partial u_j}{\partial x_i} \tag{2.23}$$

$$p = p(\rho, T) \tag{2.24}$$

$$e = e(\rho, T) \tag{2.25}$$

Expression 2.21 is the mass balance equation, 2.22 the Navier-Stokes equations, 2.23 is the energy equation, and the last two relations are general representations of the thermal and caloric equations of state, respectively. The most frequently encountered form of the thermal equation of state is the ideal-gas law $p = \rho RT$, while the most frequently encountered form of the caloric equation of state is $e = C_v T$, where C_v is the specific heat at constant volume. This system of equations represents seven equations which are to be satisfied by seven unknowns, that is: p, ρ, e, T, and u_j. The parameters λ, μ and k are assumed to be known from experimental data, and they may be constants or specified functions of the temperature and pressure.

Even though the Navier-Stokes equations are closed in the sense that they have the same number of unknowns and equations, its use is severely limited only to a few extremely simple cases where the symmetry and geometry of the problem allows for an analytical

solution. One alternative to this difficulty is to consider reasonable simplifications, based on the nature of the flow, such as considering the compressibility to be negligible. This is a fair approximation in most liquids, for numerous applications. This simplification uncouples the equations of conservation of momentum and mass to the energy equation which implies that they can be solved separately, resulting in the following expressions in vectorial notation:

$$\nabla \cdot \vec{v} = 0 \tag{2.26}$$

$$\rho \frac{D\vec{v}}{Dt} = \rho \vec{f} - \nabla P + \mu \nabla^2 \vec{v} \tag{2.27}$$

where $\frac{D\vec{v}}{Dt} = \frac{\partial \vec{v}}{\partial t} + (\vec{v} \cdot \nabla)\vec{v}$ is the total derivative of the velocity $\vec{v}$.

This form of the Navier-Stokes equations and its corresponding boundary conditions describe the motion of an incompressible fluid. Normalization of these expressions can be useful in order to generalize their applicability by means of a new set of dimensionless equations, whose solution would be valid for any situation with the same geometry and dimensionless numbers (dynamic similarity).

The Navier-Stokes equations can be normalized by changing variables as follows:

$$(x^*, y^*, z^*) = (x/L, y/L, z/L) \tag{2.28}$$

$$\vec{v}^* = \vec{v}/V_0 \tag{2.29}$$

$$P^* = P/(\rho V_0^2) \tag{2.30}$$

$$t^* = t/(L/V_0) \tag{2.31}$$

where L and V_0 are the characteristic distance and velocity of the flow. The dimensionless Navier-Stokes equations are then:

$$\frac{D\vec{v}^*}{Dt^*} = Fr - \nabla P^* + \frac{1}{Re}(\nabla^*)^2 \vec{v}^* \tag{2.32}$$

where $Re = \frac{LV_0\rho}{\mu}$ is the Reynolds number, and $Fr = \frac{\vec{f}}{V_0 L}$ is the Froude number. $\vec{f}$ is the vector of body forces that act on the fluid, usually considered to be solely the effect of gravity.

The Reynolds number is the comparative ratio between inertial and viscous effects. When $Re < 1$, the latter dominate, resulting in a flow regime where inertial forces can be neglected and thus the motion equations can be simplified and solved. Conversely, when $Re >> 1$, inertial forces dominate, and viscous effects are excluded from the equations resulting in the *ideal fluid* flow equations:

$$\nabla \cdot \vec{v} = 0 \tag{2.33}$$

$$\frac{\partial \vec{v}}{\partial t} + (\vec{v} \cdot \nabla)\vec{v} = -\frac{1}{\rho}\nabla P + \vec{f} \tag{2.34}$$

This approximation is useful only for specific conditions, one of which will be explored in section 2.2.

Boundary conditions

The boundary conditions that must be fulfilled can be divided into the following groups:

- No-slip boundary condition:

$$\vec{v}|_{wall} = \vec{U} \tag{2.35}$$

  where $\vec{U}$ is the velocity of the wall.

- Continuous stress distribution:

$$\tau_1 = \tau_2 \tag{2.36}$$

  τ_1 and τ_2 are the stresses on different surfaces that come into contact. Free surfaces have no surface stresses ($\tau = 0$).

When viscosity is disregarded (*ideal flow*) the no-slip boundary condition cannot be fulfilled, resulting in *unreal* behavior of the solutions. Care must be taken if this simplification is to be considered.

2.2 Ideal Fluid Flow

The complexity of describing deformable materials often leads to analytically untractable equations, which have to be simplified to some extent in order to have applicability [16]. One alternative to this difficulty is to consider reasonable simplifications, based on the nature of the flow, such as considering the compressibility to be negligible. This is a fair approximation in most liquids, for numerous applications. The equations that describe the motion of a Newtonian fluid (stress is linearly related to the rate of deformation) are the Navier-Stokes equations. If the fluid is considered inviscid (zero viscosity), the equations 2.33 are usually referred to as the Euler equations. Under certain flow conditions, where the inertial forces are dominant compared to viscous forces (high Reynolds number), the flow can be treated as an *ideal fluid flow*, which means that viscous effects are neglected. This apparently unrealistic model is very useful for some practical situations, provided dimensional (dynamic similarity) and flow regime considerations are taken into account.

If the flow of an ideal fluid about a body originates in an irrotational flow, such as a uniform flow, then Kelvin's theorem[16] guarantees that the flow will remain irrotational even near the body. That is, the vorticity vector $\vec{\omega} = \nabla \times \vec{v}$ will be zero everywhere in the fluid. Then, since $\nabla \times \nabla\phi = 0$ for any scalar function ϕ, the condition of irrotationality will be satisfied identically by choosing

$$\vec{v} = \nabla\phi \tag{2.37}$$

The function ϕ is called the velocity potential. Flow fields which are irrotational, can be represented in the form of Eq. 2.37, referred to as potential flows. If the expression for $\vec{v}$ is substituted in the mass conservation (or continuity equation), we find

$$\nabla^2\phi = 0 \tag{2.38}$$

This equation is the Laplace equation. By solving 2.38, the velocity field may be established without directly using the equations of motion. This is so because the condition of irrotationality has been used, and this condition is justified by Kelvin's theorem. However, the information given by these equations must be used to obtain the pressure distribution Rather than using the Euler equations directly, the Bernoulli equation, can be used:

$$\frac{\partial \phi}{\partial t} + \frac{p}{\rho} + \frac{1}{2}\nabla\phi \cdot \nabla\phi - G = F(t) \tag{2.39}$$

where G is such that $\vec{f}$ is its gradient ($\vec{f} = \nabla G$), and $F(t)$ is some function of time which may be added after integrating over the space coordinates. $F(t)$ is usually referred to as the unsteady Bernoulli constant, even though it is not strictly a constant. For steady flow conditions $\frac{\partial \phi}{\partial t} = 0$ and $F(t) = constant$.

The boundary condition to be fulfilled when solving equation 2.38 is the non-penetration condition, that states that the normal velocity on a solid surface is zero:

$$\vec{v} \cdot \vec{n} = \vec{U} \cdot \vec{n} \tag{2.40}$$

Here $\vec{U}$ is the velocity vector of the body, $\vec{n}$ is the unit normal to the surface. For this kind flows, the *no-slip* boundary condition is not necessarily satisfied. Another type of boundary conditions for these flows is when the velocity vector upstream, far from the body is known.

2.3 Solutions for the Laplace equation in spherical polar coordinates

Since we are dealing with spherical bodies, their mathematical description is more easily achieved in a polar spherical coordinate system, with the corresponding radial and angular components given by the position vector $\vec{r} = r \cdot \vec{e_r} + \theta \cdot \vec{e_\theta} + \omega \cdot \vec{e_\omega}$, as shown in Fig.2.1.

Laplace equation 2.38, expressed in polar coordinates r, θ, ω becomes:

$$\frac{\partial}{\partial r}(r^2 \frac{\partial \phi}{\partial r}) + \frac{1}{sin(\theta)}\frac{\partial}{\partial \theta}(sin(\theta)\frac{\partial \phi}{\partial \theta}) + \frac{1}{sin^2(\theta)}\frac{\partial^2 \phi}{\partial \omega^2} = 0 \tag{2.41}$$

Any homogeneous solution of this equation is called a *spherical harmonic*. Assuming a solution of the form $\phi = R\Theta\Omega$, where R, Θ, and Ω are finctions of r, θ and ω respectively; substituting in the equation and dividing by $R\Theta\Omega$ we have:

$$\frac{1}{R}\frac{d}{dr}(r^2 \frac{dR}{dr}) + \frac{1}{\Theta sin(\theta)}\frac{d}{d\theta}(sin(\theta)\frac{d\Theta}{d\theta}) + \frac{1}{sin^2(\theta)\Omega}\frac{d^2\Omega}{d\Omega^2} = 0 \tag{2.42}$$

Since the first term in this equation is the only one that involves r, it is impossible that it satisfies the equation 2.42 unless

$$\frac{1}{R}\frac{d}{dr}(r^2 \frac{dR}{dr}) = k \tag{2.43}$$

Where k is a constant. The solution of the equation

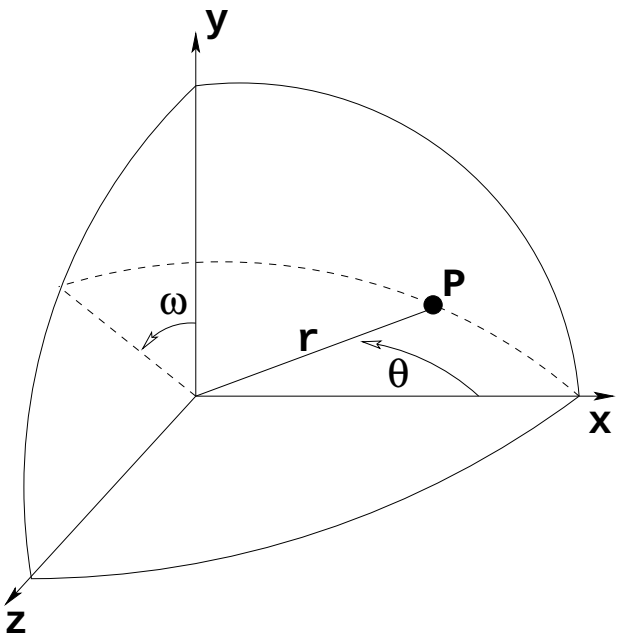

Figure 2.1: Spherical curvilinear coordinates.

$$r^2\frac{d^2R}{dr^2} + 2R\frac{dR}{dr} - kR = 0 \tag{2.44}$$

is[1]:

$$R = Ar^n + Br^{-n-1} \tag{2.45}$$

where A, B are arbitrary constants, and k was substituted by $n(n+1)$ in order to simplify the solution for R. Substitution of eq. 2.43 into 2.42, and proceeding in the same manner, it is possible to obtain a solution for Ω of the form:

$$\Omega = C\cos m\omega + D\sin m\omega \tag{2.46}$$

Which in turn, can be replaced in 2.42 to obtain:

$$\frac{d}{d\mu}\left\{(1-\mu^2)\frac{du}{d\mu}\right\} + \left\{n(n+1) - \frac{m^2}{1-\mu^2}\right\}u = 0 \tag{2.47}$$

Where $\mu = \theta$, $u = \Theta$, and m is a constant that comes from the separation of variables process on ω. The form of u being unknown at the moment, it is possible to write normal forms of the solution of the Laplace equation, say:

$$(Ar^n + Br^{-n-1})(C\cos m\omega + D\sin m\omega)u \tag{2.48}$$

The most important applications of these solutions to potential problems require the normal forms to be those in which n and m are positive integers; we shall accordingly in this chapter confine ourselves to this special case.

Let us consider the case of the equation 2.47, when $m = 0$. The equation then becomes

$$\frac{d}{d\mu}\left\{(1-\mu^2)\frac{du}{d\mu}\right\} + n(n+1)u = 0 \tag{2.49}$$

This differential equation is known as Legendre's equation, and its solution (u) depends on μ, which has already been introduced as the cosine of an angle, and would consequently have only values between $[-1, 1]$. The complete solution of this equation is:

$$u = A \cdot P_n(\cos\theta) + B \cdot Q_n(\cos\theta) \tag{2.50}$$

The functions $P_n(\cos\theta)$ are the Legendre polynomials or functions of the *nth* order. The functions $Q_n(\cos\theta)$ are the Legendre functions of the second kind, which will not be treated here because they are divergent at $\cos\theta = \pm 1$ (for a complete explanation on the subject, see [24]).

2.4 Legendre Coefficients

The velocity potential of a simple source $\phi = m/r$ is a spherical harmonic, as is immediately verified by substitution in 2.41. If the source is at a point A on the x axis, distant c from the origin as shown in fig 2.2, we have $\phi = m/R$, where $R = AP$, and this, being a velocity potential, must satisfy Laplace's equation, for it was derived from the equation of continuity. Now

$$R^2 = r^2 + c^2 - 2cr\cos\theta = r^2(1 - \frac{2c}{r}\cos\theta + \frac{c^2}{r^2}) = c^2(1 - \frac{2r}{c}\cos\theta + \frac{r^2}{c^2}) \tag{2.51}$$

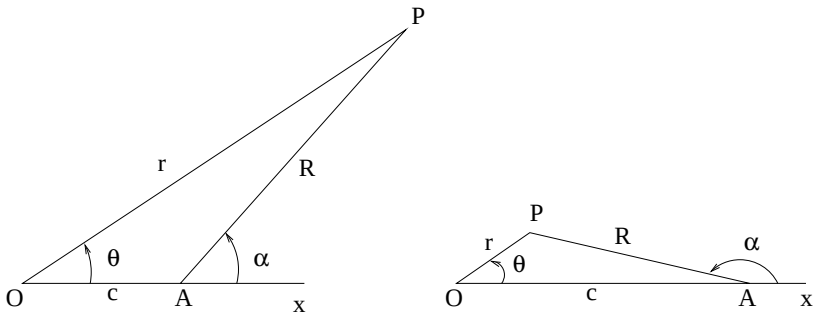

Figure 2.2: Different setups for an off-centered harmonic along the x axis

The structure 2.51 allows us for the use of the following expansion

$$(1 - 2\lambda\cos\theta + \lambda^2)^{\frac{1}{2}} = 1 + \lambda P_1(\cos\theta) + \lambda^2 P_2(\cos\theta) + ... \tag{2.52}$$

for $|\lambda| < 1$, where the coefficients $P_1(\cos\theta), P_2(\cos\theta), ...$ are independent of λ.
Thus, if $r < c$, putting $\lambda = r/c$, we have

$$\frac{1}{R} = \frac{1}{c} + \frac{r}{c^2}P_1(\cos\theta) + \frac{r^2}{c^3}P_2(\cos\theta) + ... \tag{2.53}$$

while, if $r > c$,

$$\frac{1}{R} = \frac{1}{r} + \frac{c}{r^2}P_1(\cos\theta) + \frac{c^2}{r^3}P_2(\cos\theta) + ... \tag{2.54}$$

Since the terms in $r, r^2, ..., r^{-1}, r^{-2}, ...$ of these expansions are homogeneous but o different degrees, as remarked above, each must be a spherical harmonic. Thus we have the two sets of spherical harmonics (ignoring the constants c),

$$1, rP_1(\cos\theta), r^2P_2(\cos\theta), ..., \tag{2.55}$$

$$\frac{1}{r}, \frac{P_1(\cos\theta)}{r^2}, \frac{P_2(\cos\theta)}{r^3}, ..., \tag{2.56}$$

each of which satisfies Laplace's equation identically. It can be proved, using the binomia theorem [24], that

$$P_1(\cos\theta) = \cos\theta, P_2(\cos\theta) = \frac{1}{2}(3\cos\theta^2 - 1), \tag{2.57}$$

and so on. The functions $P_n(\cos\theta), n = 1, 2, 3, ...,$ are precisely the Legendre function or *zonal harmonics*(of the first kind) [46]. These functions are appropriate to problem dealing with spherical boundaries.

2.4.1 Expansion of an off-centered dipole in series of Legendre polynomials

In the case of a doublet of strength μ at A, we have:

$$\phi = \frac{\mu\cos\alpha}{R^2} = \frac{\mu(r\cos\theta - c)}{(r^2 + c^2 - 2cr\cos\theta)^{3/2}} = \mu\frac{\partial}{\partial c}\frac{1}{(r^2 + c^2 - 2c\cos\theta)^{1/2}} \tag{2.58}$$

Thus, if $r < c$,

$$\frac{\cos\alpha}{R^2} = -\left\{\frac{1}{c^2} + \frac{2rP_1(\cos\theta)}{c^3} + \frac{3r^2P_2(\cos\theta)}{c^4} + ...\right\} \tag{2.59}$$

while if $r > c$

$$\frac{\cos\alpha}{R^2} = \frac{1}{r^2}P_1(\cos\theta) + \frac{2c}{r^3}P_2(\cos\theta) + \frac{3c^2}{r^4}P_3(\cos\theta) + ... \tag{2.60}$$

These expansions give the velocity potential of a doublet in terms of the zonal harmonics. We may add the following observation. If ϕ is a spherical harmonic, so are all its partial differential coefficients of any order with respect to x, y, z.

2.5 The associated Legendre functions

It has been shown in 2.3 that Laplace's equation is satisfied by some function u, which has the structure given by

$$\phi = \left.\begin{matrix} \mathrm{r}^n \\ \mathrm{r}^{-n-1} \end{matrix}\right\} \cdot \begin{matrix} \cos \\ \sin \end{matrix} m\omega \cdot u_n^m \tag{2.61}$$

for two arbitrary numbers n and m, in principle subject to no restriction. The mos important case which we shall consider is when n and m are positive integers such tha $n \geq m$.

Let $u = (\mu^2 - 1)^{\frac{1}{2}m} v$, then, by substitution in 2.47, it is found that v satisfies th equation

$$(1-\mu^2)\frac{d^2u}{d\mu^2} - 2(m+1)\mu\frac{dv}{d\mu} + (n-m)(n+m+1)v = 0 \tag{2.62}$$

Differentiating m times Legrendre's equation 2.49 we find that

$$(1-\mu^2)\frac{d^{m+2}u}{d\mu^{m+2}} - 2(m+1)\mu\frac{d^{m+1}v}{d\mu^{m+1}} + (n-m)(n+m+1)v = 0 \tag{2.63}$$

It follows that $\frac{d^m u}{d\mu^m}$ satisfies the equation 2.62; the complete integral of that equatio is therefore

$$v = A\frac{d^m P_n(\mu)}{d\mu^m} + B\frac{d^m Q_n(\mu)}{d\mu^m} \tag{2.64}$$

where A, B are arbitrary constants. The complete solution of 2.47 is consequently:

$$v = A(\mu^2-1)^{\frac{1}{2}m}\frac{d^m P_n(\mu)}{d\mu^m} + B(\mu^2-1)^{\frac{1}{2}m}\frac{d^m Q_n(\mu)}{d\mu^m} \tag{2.65}$$

The functions

$$P_n^m(\mu) = (\mu^2-1)^{\frac{1}{2}m}\frac{d^m P_n(\mu)}{d\mu^m}, Q_n^m(\mu) = (\mu^2-1)^{\frac{1}{2}m}\frac{d^m Q_n(\mu)}{d\mu^m} \tag{2.66}$$

are the associated Legendre functions of the first and second kind respectively. This se of functions, alltogether with the Legendre functions of the first and second kind, form a complete orthogonal set of functions that have very useful properties that can help us t solve the Laplace (and also the Poisson) equation for different boundary conditions relate to spherical geometries.

2.6 Viscous Dissipation

The last two terms of the energy equation 2.23 constitute the so called *dissipation functio* Φ. The reason for this is that they represent the rate at which mechanical energy is bein converted into heat:

$$\Phi = \lambda(\frac{\partial u_k}{\partial x_k})^2 + \mu(\frac{\partial u_i}{\partial x_j} + \frac{\partial u_j}{\partial x_i})\frac{\partial u_j}{\partial x_i} \tag{2.67}$$

The second term of the right-side of 2.67 can be expressed as:

$$\mu(\frac{\partial u_i}{\partial x_j} + \frac{\partial u_j}{\partial x_i})\frac{\partial u_j}{\partial x_i} = \mu\frac{1}{2}(\frac{\partial u_i}{\partial x_j} + \frac{\partial u_j}{\partial x_i})^2 \tag{2.68}$$

Equation 2.67 and 2.68 show that Φ is a positive definite quantity, which means that the dissipation function always increases the internal energy in an irreversible manner.

In terms of the dissipation function, the total work done by the surface stresses is given by

$$\sigma_{ij}\frac{\partial u_j}{\partial x_i} = -p\frac{\partial u_k}{\partial x_k} + \Phi \tag{2.69}$$

Where Φ is defined by equation 2.67. The first term of the right hand side of eq. 2.69 represent the reversible fraction of this work, while the second term is irreversible. This second term is of interest for calculating the work done by a moving object immersed in a viscous incompressible liquid.

2.6.1 Drag coefficient for a nearly inviscid flow

Forces arising from the motion of a body immersed in a fluid are the subject of the theoretical part of this work, and their analysis is a basic problem in fluid dynamics of great practical importance in several engineering fields. The nature of such forces depends greatly on the structure of the flow, that in the simplest case can be described by the Reynolds number and the geometry.

In the case of steady irrotational flow the total force over an immersed body can be proved to be zero. This result is referred to as d'Alembert's Paradox, since rigid bodies do experience a resistance to motion through real fluid. This inconsistency comes from the fact that irrotational flows cannot fulfill the no-slip condition, since viscous forces are excluded from this kind of flow. Nevertheless, there are flow structures that resemble very closely the behavior of a potential flow, that is, some cases of slender bodies moving through a liquid at high Reynolds number, where the streamlines are parallel far from the body, and proceed from an attachment point or points on the forward side of the body to some detachment point or points on the downstream side, apparently not causing a sensible wake or vortices behind it. Under these conditions, it could be argued that the viscous effects are confined to a thin layer attached to the body surface, outside which the flow behaves as irrotational.

In 1905, Prandtl [52] postulated his celebrated theory of boundary layers, which states that, under rather broad conditions, viscosity effects are significant (and comparable in magnitude with convection and other manifestations of inertial forces) in layers adjoining solid boundaries and in certain other layers, the thicknesses of which approach zero as the Reynolds number of the flow approaches infinity, and are small outside these layers. This hypothesis has been applied to very many different kinds of flow fields since it was first advanced. No general mathematical proof of the boundary-layer hypothesis is available but it is supported by many observations of particular flow systems [4], as well as by several of the known particular solutions of the complete equations of motion. The notion of a thin layer close to a solid boundary within which vorticity varies rapidly as a result of the combined effects of viscosity, and outside which the vorticity is zero (varies slowly), allows for the methodologies that utilize potential flow theory to calculate the field outside the

boundary layer, and then use the viscous dissipation to calculate the work done against the fluid. This calculation leads us to the mean force exerted on the fluid. This technique was used first by Levich [42] for the computation of the drag force on a sphere immersed in a uniform flow, giving

$$D = 12\pi\mu a U \tag{2.70}$$

where a is the radius of the sphere, U is the uniform velocity of the flow, and D is the drag force. Given the force, a *drag coefficient* can be calculated for different geometries. From dimensional considerations, the drag coefficient is defined as

$$C_D = \frac{D}{\frac{1}{2}\rho U^2 \pi a^2} \tag{2.71}$$

which, for the sphere analyzed by Levich is

$$C_D = \frac{48}{Re} \tag{2.72}$$

where $Re = 2aU\rho/\mu$.

If the force balance between the buoyancy and the drag forces is performed, the final rise velocity of a bubble can be calculated and compared with experiments. This task was performed by Duineveld [18] (among others), whose results are shown in figure 2.3-a. It should be noted that the data fits reasonably well the experimental results.

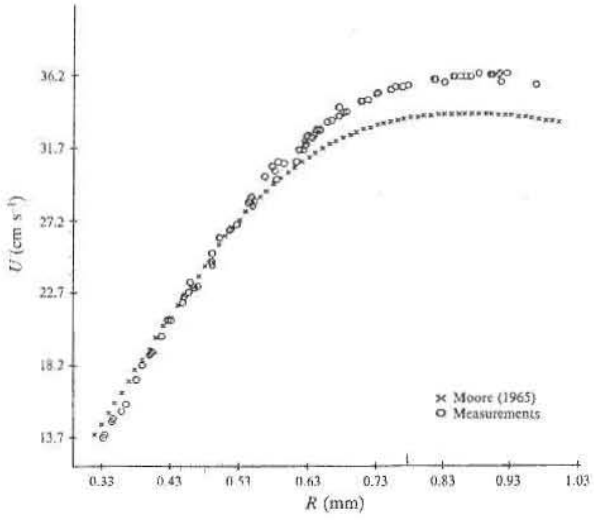

Figure 2.3: Vertical terminal velocity versus equivalent radius R. Crosses represent the analytical calculation from Moore[48]. Circles are experimental data from Duineveld[18].

2.6.2 The method of Levich

The calculation of the force exerted by the fluid on the bubble requires precise knowledge of the velocity and pressure fields. Nevertheless, it is possible to calculate the work done by the bubble on the fluid by means of energy considerations. This was the approach used by Levich [43] to calculate de drag coefficient of a bubble moving stationarily through a liquid for the dual limit of high Reynolds and low Weber numbers.

The total friction exerted over the entire surface of the bubble, as stated by Levich, is composed of two parts: resistance that acts on the bubble surface up to the separation point, and the forces that act in the turbulent zone or wake. Resistance in the first zone is viscous in nature. It can be derived most simply by computing the energy dissipated.

Since the tangential components of the stress tensor must remain continuous at the interface, and the viscosity of the gas can be disregarded in comparison with that of the liquid, the tangential force must be zero on the surface of the bubble. This fact establishes that the tangential velocity at the surface of the bubble will be constant, but it does not assure that it is zero. Thus, Levich establishes that viscous effects should become significant in a certain thin layer near the gas-liquid interface, in which a manifestation of viscosity, in the case of a real liquid, is inevitable.

The calculation of the thickness of this layer was made assuming that the velocity and pressure fields consist of an inviscid and a viscous contribution for each variable, being the viscous parts very small compared to their corresponding inviscid counterparts. A more detailed analysis of this boundary layer can be found in [47, 43]. This layer is attached to practically the whole surface of the bubble. It is possible to show that its thickness δ_s is of order $O(Re^{-1/2})$, while the order for the velocity difference between the potential flow solution and the real flow δ_v is $O(Re^{-1})$. The radius of the wake δ_r is of $O(Re^{-1/4})$, and the corresponding order for the detachment point δ_d is $O(Re^{-1/6})$, as illustrated in fig. 2.4.

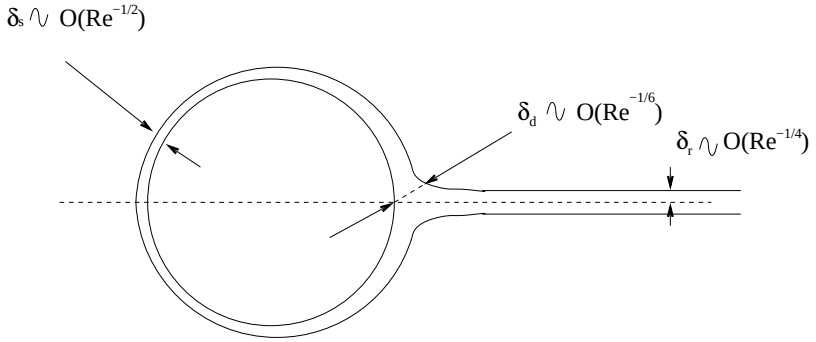

Figure 2.4: Geometric characteristics of the boundary layer of a bubble at high Reynolds and low Weber numbers

As a consequence, the velocity field arising from the solution of the potential problem (ideal fluid) is very close to the real one outside the boundary layer. It would be then convenient to think of a method of calculation for the forces based on the velocity field outside the boundary layer. That method exists, if the principle of conservation of energy is suitably applied.

If the whole liquid (ideally extending to infinity, where its velocity is zero) containing the bubble is considered as a thermodynamical system, the total work done by the bubble must equal the total change of internal energy of the liquid, since there are no other sources of work or heat in the entire system. For the stationary state,($\frac{\partial}{\partial t} = 0$) eq. 2.19 gives:

$$\int_V \Phi_{in} dV + \int_V \Phi_{out} dV = \Delta E = -W = -\vec{D} \cdot \vec{U}_P \tag{2.73}$$

where W is the work done by the bubble on the fluid, ΔE is the total change of interna energy of the system, $\vec{D}$ is the mean force acting on the bubble (drag), and $\vec{U}_P$ is the velocity difference between the bubble and the surrounding liquid. The functions Φ_{in} and Φ_{out} are the dissipative terms inside and outside the boundary layer and wake, being the latter negligeable, compared to the former ($\int_V \Phi_{in} dV << \int_V \Phi_{out} dV$).

If the dissipation inside the boundary layer is disregarded, it is possible to calculate the work using the potential flow velocity field, which is a very good approximation to the real one, and then to calculate the force.

Expressing the dissipation function in terms of the deformation rate tensor

$$S_{ij} = \frac{1}{2}(\frac{\partial u_i}{\partial u_j} + \frac{\partial u_u}{\partial u_i}) \tag{2.74}$$

and taking the velocity field to be the gradient of a potential ϕ (not to be confused with capital Φ),we have:

$$\vec{F}_D \cdot \vec{U}_P = -2\mu \int_V S_{ij} S_{ij} dV = -2\mu \int_V \frac{\partial^2 \phi}{\partial x_i \partial x_j} \frac{\partial^2 \phi}{\partial x_i \partial x_j} dV \tag{2.75}$$

The last term can be expressed as:

$$\frac{\partial^2 \phi}{\partial x_i \partial x_j} \frac{\partial^2 \phi}{\partial x_i \partial x_j} = \frac{\partial}{\partial x_j} \left\{ \frac{1}{2} \frac{\partial}{\partial x_j} [\frac{\partial \phi}{\partial x_i} \frac{\partial \phi}{\partial x_j}] \right\} = \frac{1}{2} \frac{\partial^2}{\partial x_i \partial x_j} \left\{ \frac{\partial \phi}{\partial x_i} \frac{\partial \phi}{\partial x_j} \right\} \tag{2.76}$$

It is now clear that this term is the Laplacian of the squared velocity $\Delta(\vec{u}_f \cdot \vec{u}_f)$, where $\Delta = \frac{\partial^2}{\partial x_i \partial x_j}$ is the Laplacian operator, and $\frac{\partial \phi}{\partial x_i} \frac{\partial \phi}{\partial x_j} = \vec{u}_f$ is the squared of the velocity. The work (and then the force) can be calculated, according to

$$\vec{D} \cdot \vec{U}_p = -\mu \int_V \Delta(\vec{u}_f \cdot \vec{u}_f) dV = -\mu \int_A \frac{\partial u_f^2}{\partial x_j} n_j dA \tag{2.77}$$

The volume integral expressed as a surface integral in virtue of the Gauss theorem (Appendix A).

For a single bubble moving with constant velocity U in a quiescent liquid ($u_f = 0$ at infinity), the potential is:

$$\phi = \frac{1}{2} U \frac{a^3}{r^2} cos(\theta) \tag{2.78}$$

where r is the radius for a spherical coordinate system whose origin is at the center of the bubble, θ is the polar angle and a is the sphere's radius. Substitution into 2.77 gives finally:

$$\vec{D} \cdot \vec{U}_P = -12\pi\mu a U^2 \Rightarrow C_D = \frac{48}{Re} \tag{2.79}$$

As previously stated in equation 2.70. It must be outlined that the Levich drag is a first order approximation of the drag, where the contribution of the boundary layer is

considered to be a correction of smaller order. Moore's analysis [47] allowed for a correction of this formula, taking into account the dissipation in the boundary layer and the wake:

$$C_D = \frac{48}{Re}\left\{1 - 2.211Re^{-1/2} + O(Re^{-5/6})\right\} \tag{2.80}$$

This result is theoretically valid in the limit $Re >> 1$, and is in fact an excellent estimation for the drag at $Re > 50$, as has been shown by several numerical simulations, theoretical and experimental studies [40, 18, 39].

Chapter 3

Hydrodynamic Interactions between two bubbles

As already discussed in previous sections (see 1.1), the dual limit of high Re and low We number in multiphase flows has been addressed in many previous investigations. The theoretical analysis of their properties can be achieved, for low gas volume fractions, using mathematical tools similar to those used by statistical physicists to obtain the state equation of an ideal gas from fundamental microscopic scale assumptions. The molecules present in such a gas interact unfrequently, so the overall behavior at the macroscopic scale can be inferred from the analysis of binary interactions. The simple microscopic scale assumption of perfectly elastic collisions between particle pairs, altogether with the knowledge of the thermodynamics of equilibrum in macroscopic systems, lead to a description of the state of the system in the form of the equation of state of an ideal gas[8]. The key feature to this achievement was *Boltzman's hypothesis*: The entropy of the system -a macroscopic property- is related to the probability of its state -microscopic structure-. The knowledge of this microscopic-to-macroscopic functional relation has originated several important advances in many different fields, like Einstein's description of the photoelectric effect, Plank's *Ultraviolet catastrophe* explanation, Debye's model for the thermal capacity of some elements, etc. An analogy suitably adapted to the physics of dilute bubble suspensions can be made, in order to obtain useful models of such flows. The fundamental relations between pairs of bubbles are analog to the microscopic elastic collisions among molecules. These interactions are the fundamental "microscopic" knowledge that shall be extrapolated, by means of statistical tools, to obtain constitutive equations for dilute monodispersed regime of bubbly flows.

3.1 Consequences of pairwise hydrodynamic interactions

The interactions among bubble pairs in a liquid are far more complex than perfectly elastic collisions. Since the bubbles mass is negligeable compared to that of the surrounding liquid, the kinetic energy of the system is almost entirely contained in the latter. Whenever two bubbles collide, the normal component of the relative motion reverses upon collision,

just as in the case of two elastic spherical particules. Contrary to the particules behavior in the case of a bubbly liquid all other bubbles experience a change in their velocities[60]. Another interesting effect of the interaction between many bubbles in a liquid, is that the mean bubble rise velocity in a bubbly monodispersed suspension of the corresponding characteristics is smaller than the rise velocity of a single bubble rising freely in an unconfined liquid. This peculiar behavior was analysed by Van Wijngaarden[70]. The author realized that the interactions among bubbles were primarily governed by added mass effects. If a single bubble moves in an unbounded perfect liquid, it would accelerate as if its mass was $m/2$, being m the mass of the liquid displaced by the bubble. This is referred to as the virtual or added mass. If there were more bubbles in the liquid, the flow field induced by one bubble would be distorted by the one induced by other bubbles, so the added mass now depends on the configuration of the entire bubbly flow. Van Wijngaarden used a statistical technique developed by Batchelor[4] to obtain an expression for the added mass coeficcient C_a for a bubbly flow uniformly distributed and impulsively set to motion. He found that:

$$C_a = 1 + 2.76\alpha + O(\alpha^2) \tag{3.1}$$

This coefficient affects the single bubble virtual mass multiplicatively, in order to obtain an estimate of the average added mass $\langle m_a \rangle = C_a m/2$. These results were based on pairwise interactions calculated from a random distribution of spherical bubbles. The Laplace equation was solved using the technique of twin spherical expansions. This mathematical solution was obtained using the analysis proposed by Jeffrey[25] for heat conduction. The way these interactions can affect the added mass was illustrated by calculating the added mass m_a of a single bubble, when only two bubbles move, with velocities parallel and perpendicular to the liquid flow. In the former case (parallel), the velocity induced by each bubble on the center of the other is in the direction of the flow velocity, giving

$$m_a = \frac{1}{2}\rho V\{1 - 3(\frac{a}{R})^3 + O((\frac{a}{R})^6)\} \tag{3.2}$$

whilst for the latter case we have

$$m_a = \frac{1}{2}\rho V\{1 + \frac{3}{2}(\frac{a}{R})^3 + O((\frac{a}{R})^6)\} \tag{3.3}$$

In this situation (bubbles aligned perpendicular to the fluid velocity) the added mass of each bubble in the pair is larger than that of a single bubble, because the velocity induced at the centre of one sphere by the other one is opposed to the main flow velocity. This qualitative explanation gives insight of the phenomena that occurs when several bodies interact, moving while immersed in a liquid.

Posterior studies conducted by Biesheuvel and Van Wijngaarden[5], and later by Kok[31], showed that it is possible to obtain a model for the trajectories of a pair of bubbles moving in a perfect fluid, solving the Laplace equation with the aforementioned techniques (see figure 3.1). A dynamical model of the trajectories was obtained, using the Lagalli theorem of multipoles[37] in the former case and Lagrange's formalism in the

latter. Both investigations reveal that, depending on the angle of orientation of the axis that joins the bubbles centers, regions of attraction and repulsion can be found. Pairs of bubbles aligned within an approximate angle of $\theta_c \approx cos^{-1}\sqrt{1/3}$ to the direction of the mean bubble motion (parallel to motion) are repelled by each other due to a Bernoulli effect, while those aligned in a plane perpendicular to that same direction (perpendicular to motion) are attracted towards each other, as shown in figure 3.2. As a consequence of such interaction, bubbles should tend to reorganize themselves in bubbly aggregates, as has already been verified by several numerical and theoretical studies (see section 1.3). This is the clustering theoretical prediction that shall be verified experimentally in chapter 4.

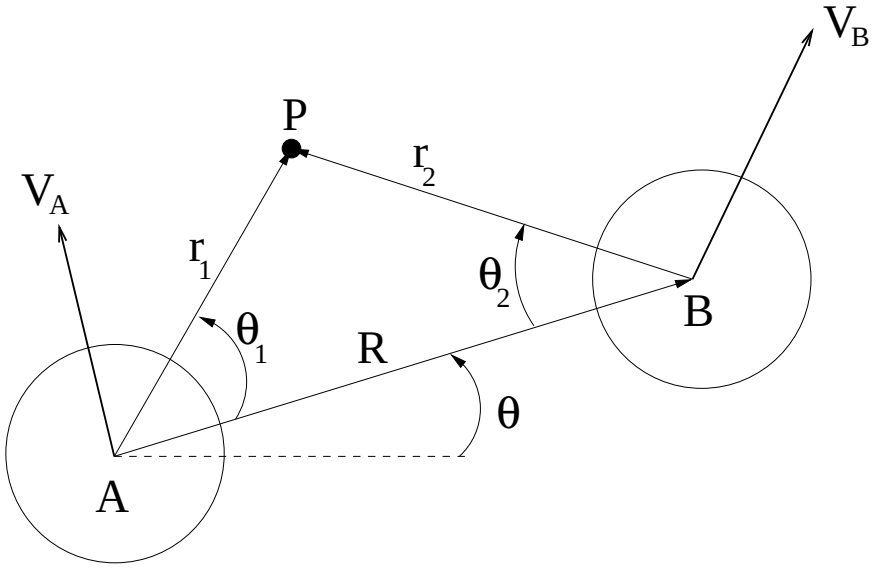

Figure 3.1: Spherical curvilinear coordinates used by Biesheuvel and Van Wijngaarden[5]. The picture shows two spheres A and B moving at speeds V_A and V_B in an inviscid liquid. The polar coordinates r_1, r_2, θ_1 and θ_2 define any position P with respect to each bubble center.

If anyone observes a single millimetric air bubble rising through water, one notices that its trajectory is a straight line for bubbles of less than a critical diameter of about one millimeter. If a cloud of bubbles of the same characteristics are released in the same liquid, the trajectories will oscilate in a very complicated manner. For the case of binary interactions, the trajectories of two bubbles ascending in a quiescent liquid were calculated, and compared with careful experiments[31]. The actual trajectories were fairly well predicted by the theory, based on velocities calculated from a potential and a set of dynamical equations for the relative velocities and the center of mass of the two bubbles array. These trajectories are complex, but in general terms, the bubbles tend to come together and collide along the line $\theta = 1/2\pi$ if their initial orientation is not close to a vertical alignment between bubbles centers. If the liquid is free of surfactants, the bubbles coalesce, but if a small amount of contamination is present in the liquid, they bounce. In the case of a cloud of bubbles, the motion of other bubbles generates pressure forces and viscous forces

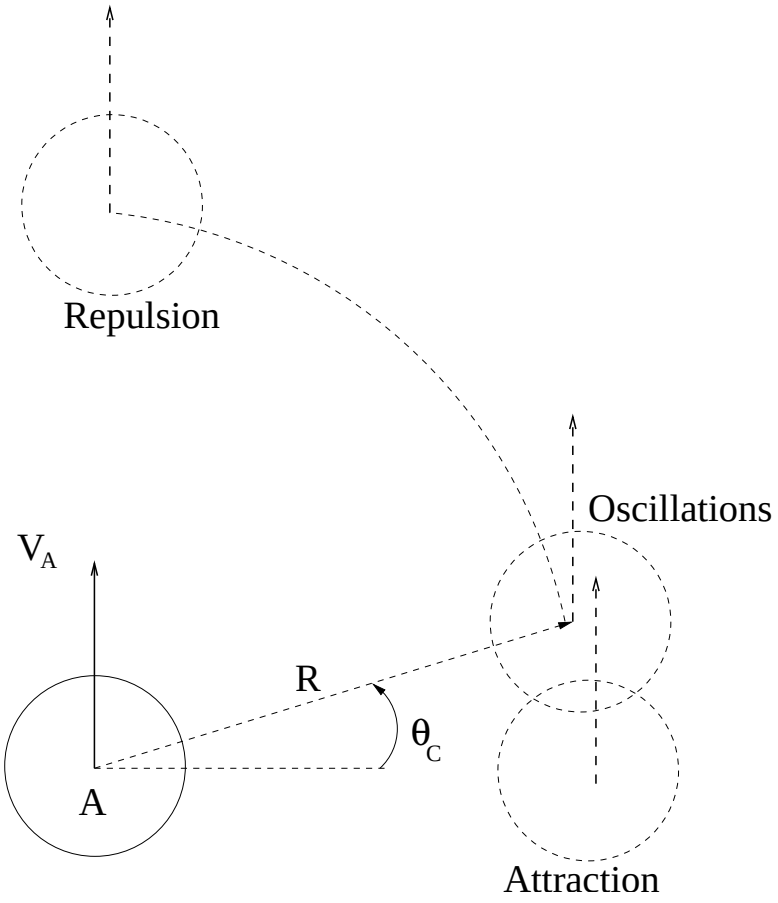

Figure 3.2: Regions of attraction between bubbles, depending on the angle θ_0 between the axis among bubble centers and their mean velocity (see Biesheuvel and Van Wijngaarden[5]).

on each test bubble, and these forces lead to deformations on the bubbles sufaces. These complex interactions between the flow field, forces and deformations are complicated, if not impossible, to describe mathematically in a deterministic manner. This situation lead Van Wijngaarden[74] to treat the problem as a stochastic one, obtaining the conditional probability density $P(R, R_m)$, based on a set of simplified equations of motion for a pair of bubbles that resulted from the work of Kok[31]. This $P(R, R_m)$ is the probability of finding a pair of bubbles at a distance $2R$ between them, given the maximum separation to be from $2R_m$ to $2(R_m + dR_m)$, and served the purpose of calculating an ensemble average for the velocity $\langle v \rangle$:

$$\langle v \rangle = U_\infty \{1 - 1.56\alpha + O(\alpha^2) + ...\} \tag{3.4}$$

where $\langle v \rangle$ is the mean rise velocity of the bubbles and U_∞ is the terminal rise velocity of a free bubble. This equation 3.1 states that at higher volume fractions the mean bubble velocity decreases. This result agrees with the actual qualitative behavior of bubble suspensions. Mean rise velocity decreases with volume fraction, as verified by some experimental studies[73, 14, 80].

Binary hydrodynamic interactions can also be used to calculate properties and averaged equations for bubbly liquids, as done by Spelt and Sangani[65]. They determined average properties in the limit of large Reynolds and small Weber numbers, as function of the volume fraction, mean relative velocity and velocity variance of the bubbles, using numerical simulationss and pair interaction theory. Kok[32], also calculated the mean-square fluctuating velocity in a uniform suspension and the hydrodynamic diffusivities in a nonuniform one, by performing an ensemble average over pair interactions. This pair averaging procedure is valid for dilute suspensions ($\alpha \ll 18/Re$). These statistical techniques are beyond the scope of the present investigation, nevertheless it should be mentioned that they are a powerful tool for modeling complex systems like multiphase flows.

Chapter 4

Experimental determination of clusters in a narrow channel

4.1 Introduction

As mentioned in previous sections (see 3.1), the interaction between more than two bubbles is complex, and it is difficult to calculate their positions and velocities. For real bubbly flows the experimental approach is often adopted, in order to ellaborate on models that describe the flow quantitatively. Although mathematical tools like differential and integral equations of motion can be very useful to describe such flows, it is always necessary to validate them experimentally. For the case of bubbly flows at high Reynolds ($Re > 30$) and low Weber numbers($We < 1$), potential flow theory can be used to calculate velocity fields in the case of binary interactions (low volume fractions). Previous theoretical and numerical investigations reported that monodispersed bubbly flows of such characteristics are unstable, in the sense that the flow tends to reorganize itself into horizontal bubbly aggregates or clusters. These clusters may have a very different dynamical behavior than clouds of bubbles uniformly distributed. Clusters could influence the surrounding flow field[58], introducing enhanced velocity fluctuations and hydrodynamic interactions that could affect the overall flow structure. One possible mechanism of this phenomena is depicted in Fig. 4.1. On the left, a uniform bubbly flow is shown. The wakes and velocity differences between these individual bubbles are not very significant. On the other hand, if the bubbles are clustered, these agglomerations could act as single large objects, as in the rightmost image of the same figure, and the wakes and velocity fluctuations could be very important, leading to a different behaviour than the one predicted by the theory, based on the uniformity assumption. The way clusters interact with the overall flow is not yet well understood, but the importance of certain flow parameters on their formation and dynamics has already been identified: the effect of the volume fraction, α, on the added mass coefficient was first theoretically calculated by Van Wijngaarden[70] for uniformly distributed bubbly flows. Spelt and Sangani[65] noted that the added mass coefficient for clustered bubbly liquids was much greater than the theoretical predictions for uniformly distributed bubbles. They also showed that the tendency to form aggregates is diminished

when the velocity fluctuations in the bubbly liquids are increased. The formation o clusters was not observed for sufficiently low values of the ratio between the magnitude of the mean relative velocity of the bubbles and their root-mean-squared velocity. I the bubble aggregate's contribution to the velocity fluctuations is important, then they may contribute to their own breakup, so it would be reasonable to expect their *lifetime* to be very short. This was observed by Bunner and Tryggvason[10]. Zenit *et al.* [80] performed experiments with monodispersed gravity driven bubbly flows, and obtained direct observations of clusters. They measured a preferential tendency to the horizontal orientation of the bubbly aggregates. The strength and size of such clusters was much more modest than those reported in the computer simulations. These differences were attributed to other effects not considered in the potential flow formulation, such as the bubble path instability [45] or the cluster induced agitation [80]. Since the image analysis was performed on three dimensional (3D) flows, there was some uncertainty about the extent of the detected clustering.

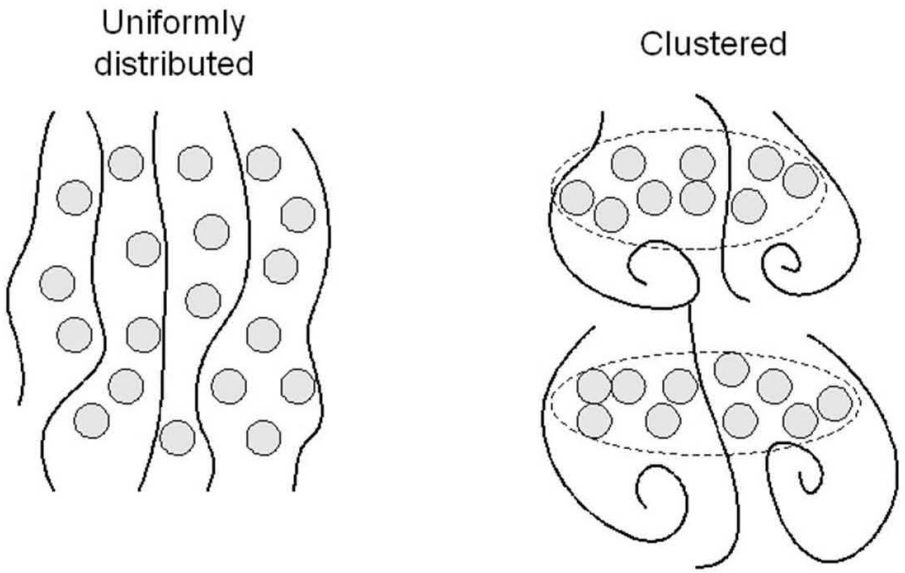

Figure 4.1: Sketch of clusters acting as single large objects, generating large velocity fluctuations in the flow.

4.2 Experimental Investigation

In this investigation a new alternative experimental technique was used to observe and measure the extent of clustering that appears in these type of bubbly flows. A thin channel was built, in order to generate a two-dimensional bubbly flow where bubbles were not allowed to superpose in the depth direction. As a result, we were able to perform direct image analysis of the 2D bubbly flow and structures present therein. It must be emphasized that there are strong wall-effects that must be taken into account. It is expected, however, that the qualitative behavior of the 2D experiment will be the same as

% Weight	$\rho(kg/m^3)$	$\mu(\times 10^{-3} Pas)$
0 %	9.98230	1.005
15%	1.03450	1.53
20%	1.04690	1.76
22%	1.05210	1.91
30%	1.07270	2.5
50%	1.12630	6.0

Table 4.1: Fluid properties for different Glycerine percentage in weight (20^oC)

its 3D equivalent, since the channel width is such that inertial effects are not negligible, being dominant in the direction of the mean bubble velocity. Further verification of the qualitative behavior of the flow was obtained experimentally (see section 4.5.5), by comparing the behavior of the mean terminal velocity of the bubbles with the theoretical prediction of Van Wijngaarden[70].

Experiments were performed with liquids of different viscosities. The ranges of Reynold and Weber numbers tested were $90 < Re < 250$ and $0.4 < We < 0.6$ respectively. The liquids used were deionized water and glycerine mixtures, with a small amount of $MgSO_4$ in order to reduce coalescence[80]. Millimetric size bubbles were produced with an array of capillaries; each capillary tube was separated about six bubble radii. Special care was taken in order to avoid contamination, since the presence of surfactants may drastically alter the boundary conditions at the bubble surface. The water resistivity, prior the mixture preparation was at least $11 M\Omega$cm; nevertheless, our experiments could not be considered to be ultra pure as in Duineveld's case[18]. A properties table is presented for different mixtures of glycerine and water (table 4.1).

4.3 Experimental setup

The experimental setup used in this investigation is shown schematically in Fig.4.2. It consists of a tall thin channel of 30cm width and 120cm height, fabricated with two glass sheets, separated by two glass strips of thickness 3mm. An array of 10 identical capillaries, through which nitrogen gas flows, was located at the channel base. With this array a nearly mono-dispersed stream of bubbles was formed. The gas volume fraction α is calculated as follows:

$$\alpha = \frac{V_g}{V_l} = \frac{\Delta H}{H} \tag{4.1}$$

where V_l and V_g are the volume occupied by the liquid and gaseous phases, H is the level of liquid in the channel, and ΔH is the increase in height. Since the channel is very narrow, a small volume difference causes the level to increase considerably.

A high speed video camera, able to capture high resolution images at up to 1000 fps was used. These images were processed digitally to obtain measurements of the bubbles

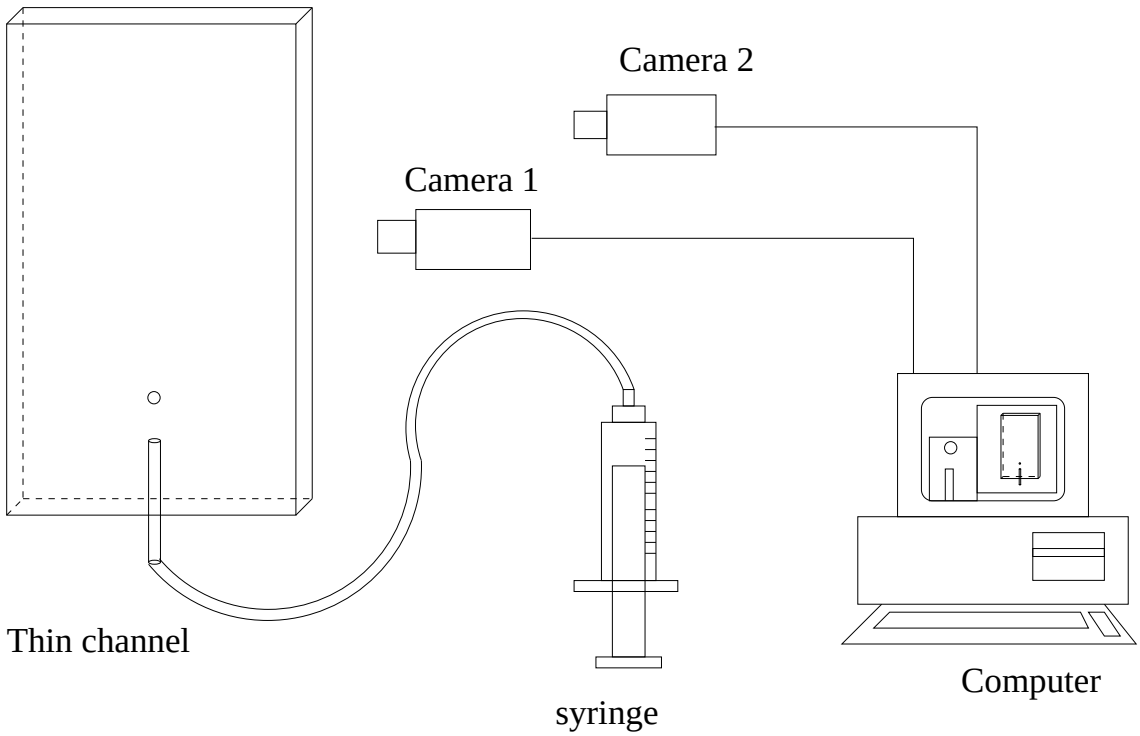

Figure 4.2: Experimental setup. Nitrogen is injected through the capillary bank to produce the bubbles

properties, such as mean bubble size and velocity. More importantly, groups of neighboring bubbles could also be recognized. Figure 4.3 shows several typical images obtained from the experiment. The clustering phenomena can already be noticed by simple inspection.

4.4 Digital Image Analysis

To quantify the extent of clustering, a program was developed using the Matlab Image Processing Toolbox© to process the images. The procedure to determine the size, position and orientation of the clusters is as follows: the digital images from the high velocity camera were loaded and equalized, in order to separate the background from the bubbles; the neighboring objects were related by a separation distance criteria and then "glued" on a single cluster; the resulting images were transformed to binary format (see Fig. 4.4), and then processed to identify the clusters and measure their properties (area, position, centroid, orientation). The clusters angle was obtained from the angle of the major axis of an equivalent ellipse with the same first and second area moments as the detected objects. The program stores the orientations and calculates the histogram of the angles of many images, at least 100 for each case.

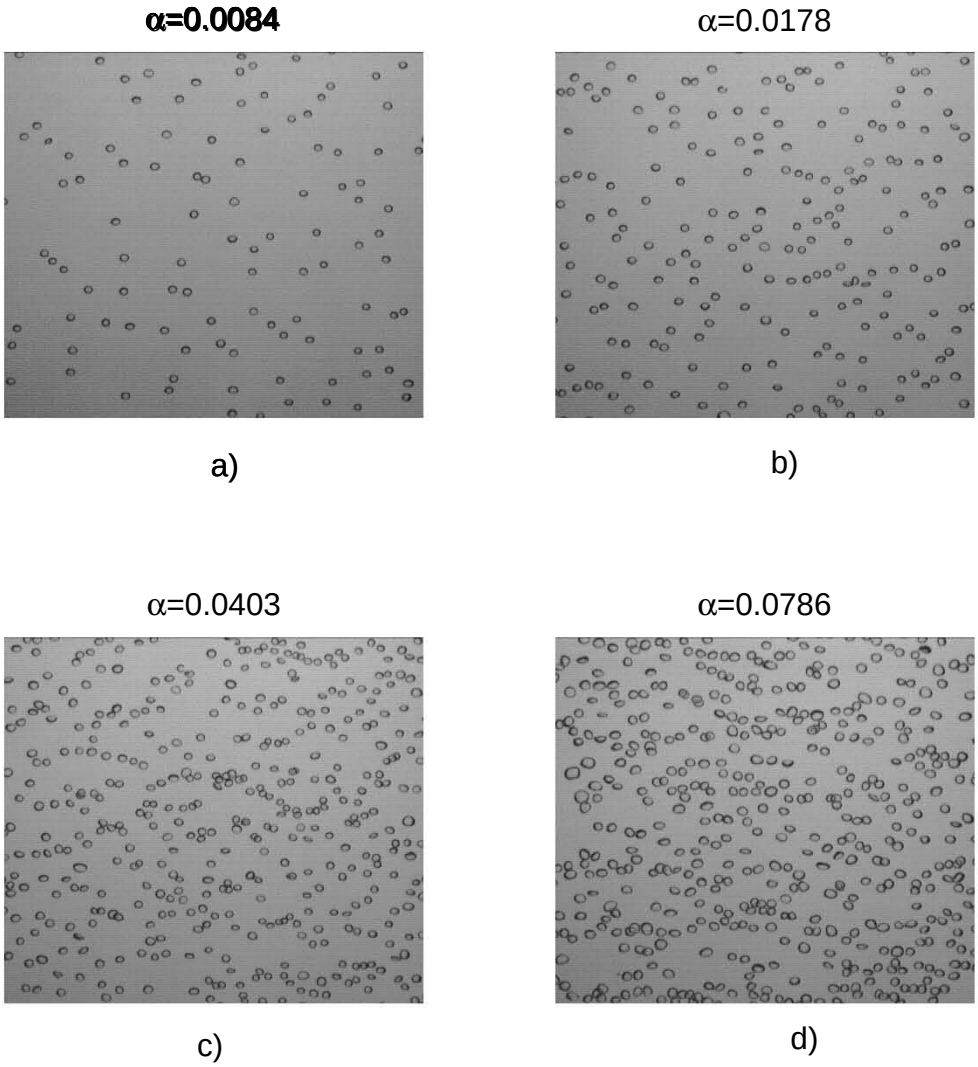

Figure 4.3: Typical images captured by the digital high speed camera for different volum fractions α. Nitrogen bubbles in water. a)$\alpha = 0.0084$ b)$\alpha = 0.0178$ c)$\alpha = 0403$ d)α = 0.0786.

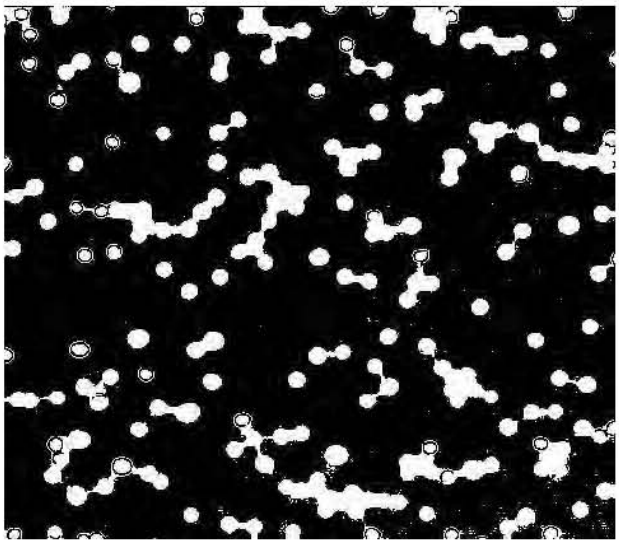

Figure 4.4: Bubbly flow picture as a binary image

4.5 Results

The experimental results obtained using digital image analysis are presented next, organized into sub-sections. The commercial software Matlab©, and the image processing toolbox (also part of that software) were used to develop different routines that allowed for the calculation of bubble positions, velocities, relative distances and angles. It was also possible to identify clusters of bubbles, based on their size and aspect ratios, so a comparison between clusters and individual bubbles is presented in order to evaluate the effect of clustering on the flow. The angular measurements can be directly related to the theoretical predictions mentioned in previous chapters (1.3).

4.5.1 Clusters Angles

Figures 4.5, 4.6, 4.7 and 4.8 show typical normalized histograms of the clusters angles. The statistical tendency to the horizontal is evident. As the volume fraction increases, the clusters area also grows, a fact that was later verified using the radial distribution function. Figures 4.9, 4.10 and 4.11 show the clusters mean area, normalized with respect to the mean bubble area for each volume fraction. As α grows, the mean number of bubbles in each cluster increases. The experimental conditions did not allow us to test this tendency for volume fractions higher than 0.13.

Performing a t-test at significance level 0.05 to determine whether a sample from a normal distribution could have zero mean (considering unknown standard deviation) we concluded that for the experiments previously shown, the null hypothesis cannot be rejected. A 95% typical confidence interval would be $-0.5639° < \overline{\theta} < 3.0166°$. Performing a similar test on all other experiments at different volume fractions, we could conclude with 95% of certainty, that the mean angle is always in the range

$$-5^\circ < \overline{\theta} < 5^\circ \tag{4.2}$$

which proves a clear tendency to horizontal. This tendency was obtained for a limited range of distances, since the clusters were identified by grouping neighboring bubbles only. This limitation will be overcome in the next two sections, where far reaching interactions will be evidenced using the radial and conditional angular distribution functions.

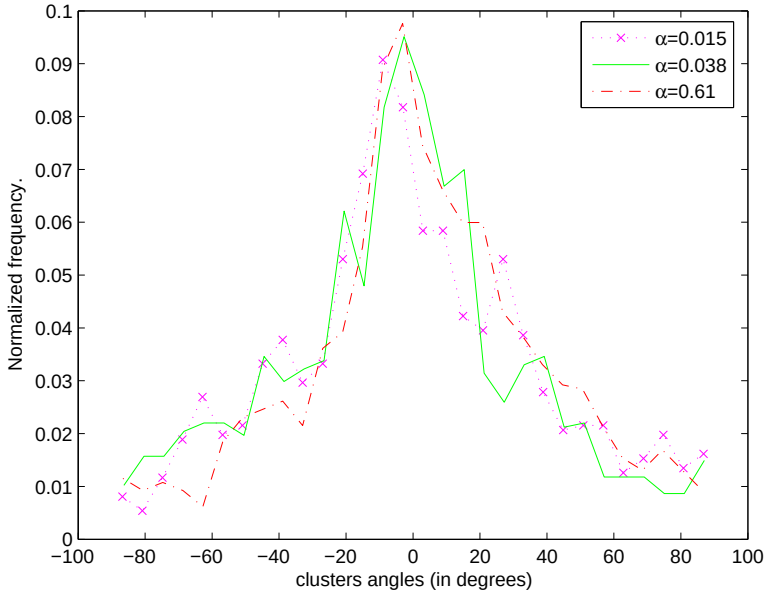

Figure 4.5: PDF of clusters angle for different volume fraction α. Water.

4.5.2 Radial Distribution Function

To complement the analysis of the angular distribution, the digital image analysis data permitted the calculation of the radial distribution function $g(r)$, which is an average measure of the probability of finding one bubble located at a given radial distance r from another reference bubble. The calculation procedure is similar to the one used by Younge *et al.*[78]. They defined the radial distribution function as the ratio between the probability of finding a particle in a given subvolume dV, and the probability of finding a particle in dV if the particles were uniformly distributed:

$$g(r) = \frac{dN/dV}{N/V} = \frac{(dN/N)}{(dV/V)} \tag{4.3}$$

where N is the total number of bubbles and V the total volume of the region of interest. Since our experiment is two-dimensional, V represents the image's total area and dV represents certain element of area with a given value for r (the region contained between the circles $r = r$ and $r = r + dr$).

If the bubbles were points in space, a uniform distribution would have $g(r) = 1$. The finite volume of the bubbles causes an excluded volume effect that modifies the form or

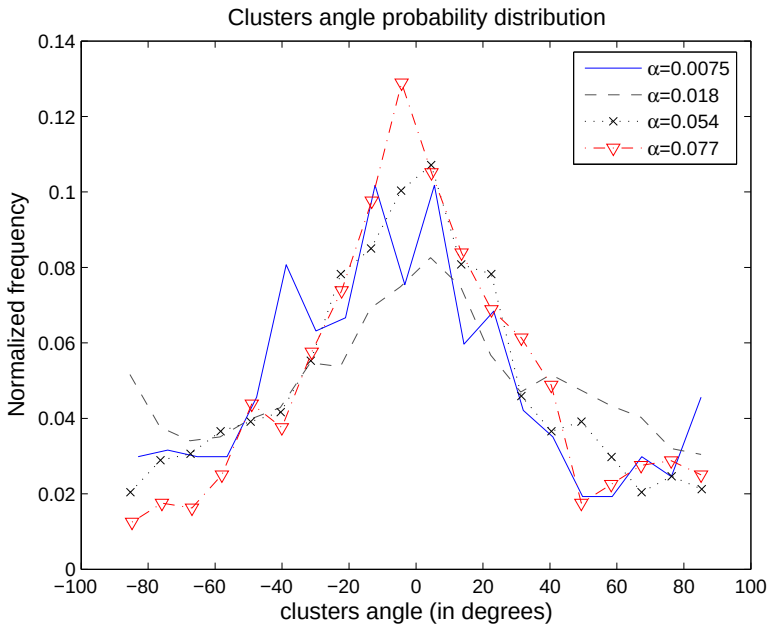

Figure 4.6: PDF of clusters angle for different volume fraction α. Water-glycerine 15%.

$g(r)$. In order to properly compare the experimental distributions with a corresponding array of particles with no hydrodynamic interacion, a theoretical $g(r)$ was calculated, using the Percus-Yevick pair distribution function for hard spheres[50]. This theoretical distribution is exact, and considers a potential defined by:

$$\phi = \begin{cases} \infty; r \leq a \\ 0 \ ; \ \mathrm{r} > \mathrm{a} \end{cases} \quad (4.4)$$

where ϕ is the force potential and a is a particle radius. For radial distances greater than one particle radius, the force is zero, while for $r = a$ (contact between spheres), the force is infinite.

This distribution has a peak near the value $r/r_m = 2$, which means that rigid spheres cannot penetrate each other. For low concentrations the initial slope of these curves is almost vertical, reaching rapidly the unitary value $g(r) = 1$. Random arrays of bubbles of finite size were also numerically produced and their radial distribution functions were computed (dash-dotted lines in figures 4.13, 4.15, 4.16, and 4.17, and 4.18). These random radial distribution functions are qualitatively similar to those obtained by Yurkovetski and Brady[79] for bubbles in random motion.

Since the digital image processing permitted us to obtain the centroids for each bubble in every picture taken, it was possible to measure the number of bubbles contained in the differential areas dA, composed by ring-shaped subregions between the radius r and $r+dr$ (see figure 4.12). The values for dr were small radial increments of the order of one bubble's mean radius. Every frame was swept by these subregions, using increasing radii, starting from the centermost bubble, until the limit of the corresponding picture was reached. The radial distribution function $g(r)$ was obtained for each frame, and then averaged, providing

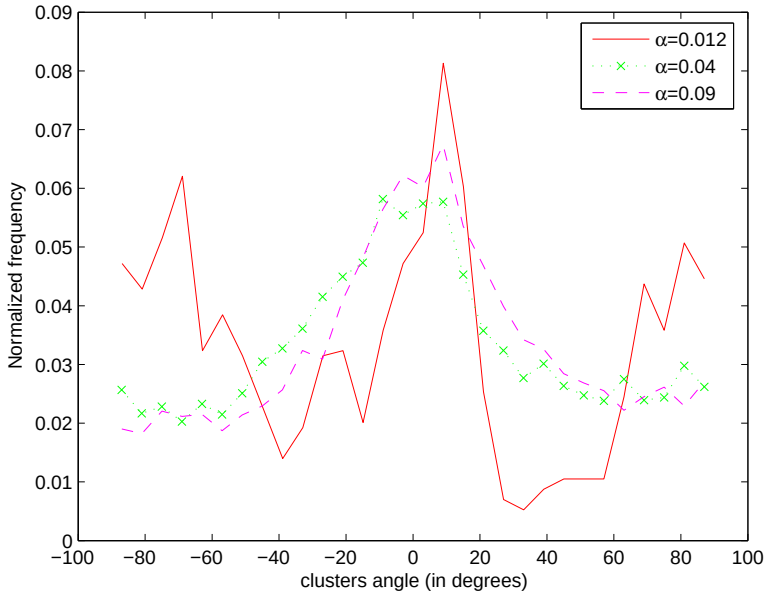

Figure 4.7: PDF of clusters angle for different volume fraction α. Water-glycerine 30%.

a time independent description of the system's structure.

The radial distribution function for different values of α is shown on the left of Fig. 4.13. The results are presented in terms of $r^* = r/r_m$, where r_m is the mean bubble radius for each experiment. The dotted lines are the corresponding theoretical $g(r)$ calculated using the Percus-Yevick pair distribution function for hard spheres. For $r^* < 2$, $g(r^*) = 0$, because the minimum distance between bubbles centers is approximately two times r_m. When the volume fraction is very low (for $\alpha = 0.0084$ and $\alpha = 0.40$), the value of $g(r^*)$ for small values of r^* is less than one, which implies that there is a region of low probability of occupation around the vicinity of any bubble. As the volume fraction increases, the probability of finding neighboring bubbles at closer distances increases. For $\alpha = 0.079$, a peak can be observed for $r^* \approx 5$, showing a slight tendency that differs from the corresponding hard-sphere array, without being conclusive.

4.5.3 Conditional Orientation PDF

The clustering tendency can be further corroborated by calculating the conditional probability distribution, similar to that obtained by Bunner and Tryggvason[10], for a given radius r. This conditional probability was calculated from the digital images using a method similar to the one used to obtained $g(r)$: differential ring-shaped elements were constructed, centered on each bubble (see Fig. 4.14), and the θ-dependent frequency histograms for given radial values were obtained. The circle was divided into discrete angular sectors$\Delta\theta$ and the bubbles centers located in the range $r_2 - r_1$ within $\Delta\theta$ were counted.

The curves on the right in Fig. 4.13 show the conditional probability distributions of the angle θ with respect to the horizontal, obtained for different ranges of normalized bubble distances r^*. For low values of volume fraction ($\alpha = 0.0084$) the distribution does

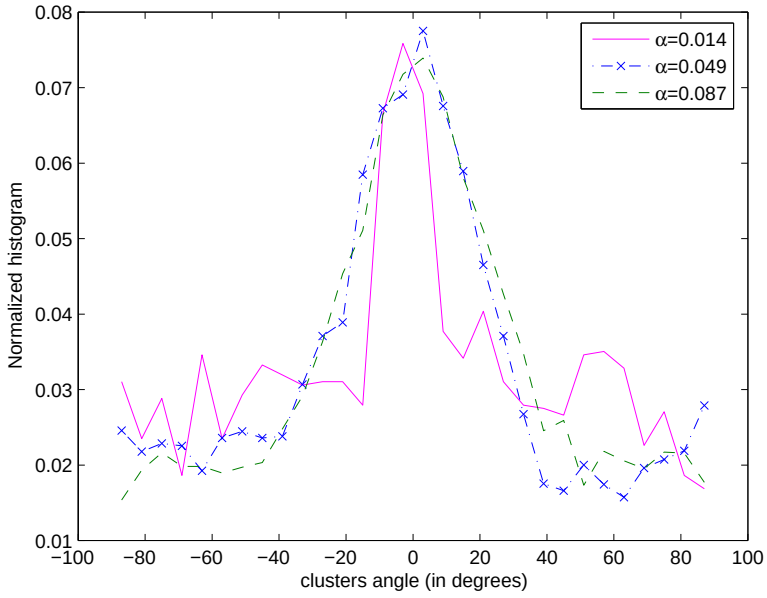

Figure 4.8: PDF of clusters angle for different volume fraction α. Water-glycerine 50%.

not exhibit any clear tendency because the bubbles are relatively far from each other; hence the interactions are weak and the distribution is almost uniform. For $\alpha = 0.040$ and $\alpha = 0.079$, it can be observed a clear tendency for small distances to align around $\theta = 0$, while for larger values of r^* ($20 < r^* < 25$), this behavior is less apparent. This is an evidence that these distance-dependent forces have a preferential horizontal orientation.

4.5.4 Conditional orientation PDF dependence on Re.

The way viscous effects can influence clustering is not clear for the moment, but we can hipothesize three ways in which the flow could be affected: the first one is due to the hydrodynamic interaction dependency on the Reynolds number. Lift forces are dependent on both the Reynolds number and the radial distance between bubbles. It can be shown that lift even changes its sign for certain Reynolds number (for a given radial separation) for the case of two bubbles rising side by side in a liquid[40]. This suggests that the clustering tendency should decrease with the Reynolds number. The second kind of viscous effect is related to the bubble's wake. It has been observed that even for large Re, bubbles wakes do affect other bubbles motion (see [75] and references therein). This situation was also observed by us during our experiments; bubbles get trapped into other bubbles wake and follow its trajectory. These viscous effects will tend to brake horizontal clustering, since wakes are a source of attractive forces between vertically aligned bubbles. The third form of viscous effect is vorticity creation and diffusion. When bubbles rise in the liquid, their shape is that of an oblate ellipsoid. As the aspect ratio grows larger, a major amount of vorticity is created on the bubble's surface, and convected to the wake (see section 5.5.4). These three situations are a source of velocity fluctuations, which are discussed in the next section.

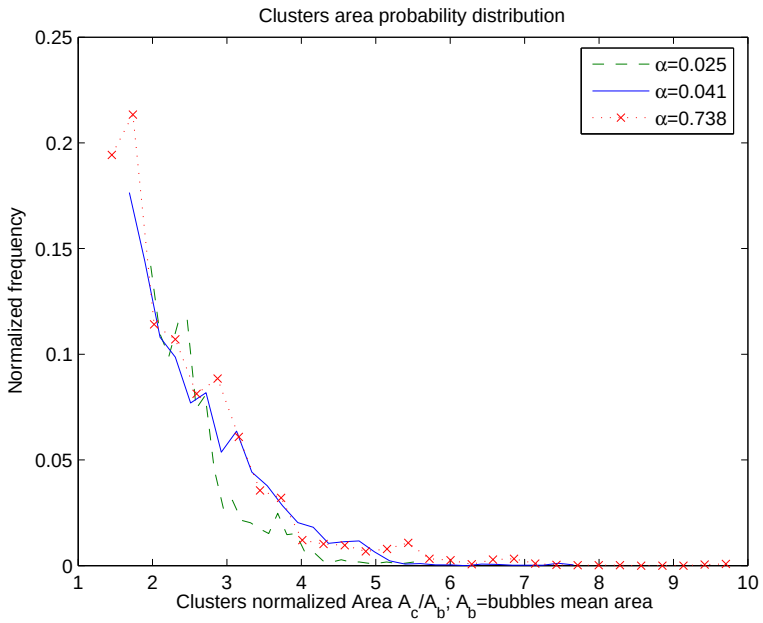

Figure 4.9: PDF of clusters normalized area with respect to the mean bubble area A_b for water

In order to measure the effect of viscosity on clustering, we performed the same type of measurements changing the liquid viscosity, i.e. for different Reynolds numbers. Experiments were conducted using various glycerine aqueous solutions. As the viscosity increases, the bubble terminal velocity decreases, resulting in a different mean Reynolds number.

Figures 4.15, 4.16, 4.17, and 4.18 are similar to Fig. 4.13, where both the radial distribution function and the conditional angular distribution are presented. The first one corresponds to water, the next figures correspond to glycerin aqueous solutions of 15%, 30% and 50% in weight respectively. In all the figures the effect of increasing the gas volume fraction is that the angle PDF tends to be more flat, showing that the short distance horizontal orientation tends to decreas with volume fraction, as expected. It can be observed that the radial distribution function differs from that of an array of solid spheres, as a result of hydrodynamic interactions, which act as a distance (and angular) dependent potential. Fig. 4.15 is interesting because it can be observed that, for $\alpha = 0.04, Re = 409$, horizontal orientation is less pronounced but similar to that in Fig. 4.14 (both peaks reach approximately 0.6), where the same gas volume fraction is shown for a lower $Re = 177$.

When the volume fraction is very small (less than 0.01), interactions between bubbles are unfrequent, and bubbles tend to be distributed randomly. As α increases, bubbles interact more frequently and hydrodynamic forces lead to horizontal clustering. This phenomenon has a peak, which happens approximately at $\alpha_{max} = 0.0112$ in the case of water, as can be seen in Figure 4.16. If the volume fractions continues to increase, then viscous effects tend to break horizontal clustering and the system seems to return

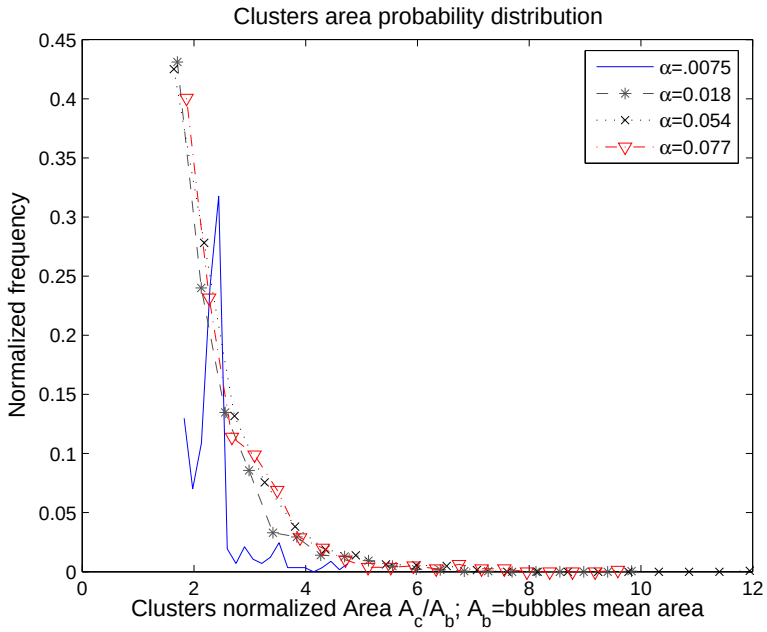

Figure 4.10: PDF of clusters normalized area with respect to the mean bubble area A_b for water-glycerine 15%.

to an almost random angular distribution again. In all cases the onset of this decline in orientation coicides with a large peak in the radial distribution functions, suggesting that $\alpha_{max} < 0.0125$ for a glycerin concentration of 30%, and also $\alpha_{max} < 0.013$ for the case of 50% glycerine concentration solution.

4.5.5 Mean rise velocity

The mean bubble velocity is another important characteristic of the flow that can be calculated from the same experiments. As mentioned earlier, the entire bubbly flow configuration (i.e. the positions and velocities of all bubbles) determines the final rise velocity for a given void fraction. In general, for inertial bubble suspensions, as the volume fraction α increases, the mean rise velocity decreases. This behavior was also experimentally observed in our experiments, and compared with equation 3.1, obtained by Van Wijngaarden[70] using potential flow theory, based on pairwise hydrodynamic interactions. A program was developed in matlab©to analyze each image sequence and identify individual bubbles to calculate their corresponding velocities (using a scale and the rate of frames per second). In spite of the fact that our experiment is confined between two walls, in a "2D" configuration, the qualitative behavior of these flows is consistent with the inertial 3D bubbly flow of Van Wijngaarden. The velocities are slower than Duinevield[18]'s experiments because of two main reasons: the confinement effect and an instability that makes the bubbles bounce from one wall to another. This oscillating effect will be further discussed later on the next two chapters.

The velocity probability distributions were obtained from a large set of bubbles for

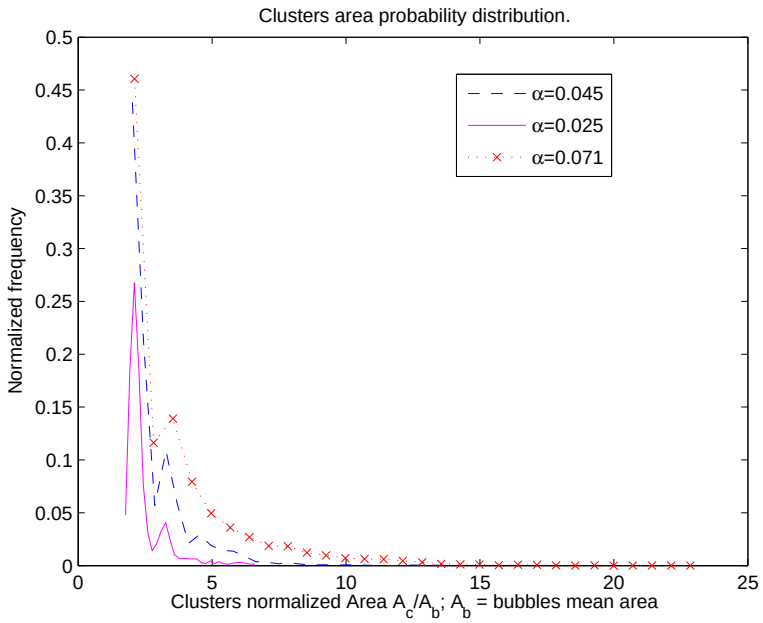

Figure 4.11: PDF of clusters normalized area with respect to the mean bubble area A_b for water-glycerine 30%.

each volume fraction. A plot of the probability distribution of the velocities for different values of the gas volume fraction is presented in figure 4.20.

It was also possible to compare velocity and size of bubbles and clusters separately. Figures 4.21, 4.21 and 4.21 are plots of bubbles and clusters velocities. The circles, squares and rhomboids represent bubbles mean rise velocity for different volume fractions, while the crosses are the corresponding mean rise velocities of the clusters. In this case the gas volume fraction was low, and as a result most of the clusters were formed by two bubbles only. For the case of two bubbles rising side by side, aligned perpendicular to gravity, it is possible to estimate the final rise velocity U_f using potential flow, by combining equations 3.1 and 5.3, which gives $Uf = 2g\tau/(1 + 3/2s^3 + ... + O(s^6))$. This final velocity is represented by stars for water-glycerine 15% and dots for water. The hydrodynamic interactions between both bubbles have the net effect of increasing the added mass and drag. As a result, the final velocity decreases. This inertial effect slows down clusters, compared to single bubbles. As can be seen from the figure, this can explain the behavior of the clusters, but there is still a small unexplained difference between measured data and the potential flow prediction. If the difference is due to velocity fluctuations, then the net effect of these would be to decrement the final rise velocity of the bubble cloud. Clusters breakup should also be reflected on their lifespan, which is the time bubbles remain close enough to be considered a single cluster. This lifespan can also be measured, and should decrease as velocity fluctuations grow. In Fig. 4.24 a plot of such time versus gas volume fraction is presented, for different test liquids. In this figure it is clear (with the exception of water measurements) that this tendency is verified. The strange behavior for water could not be explained at the present time. The criteria used to consider that

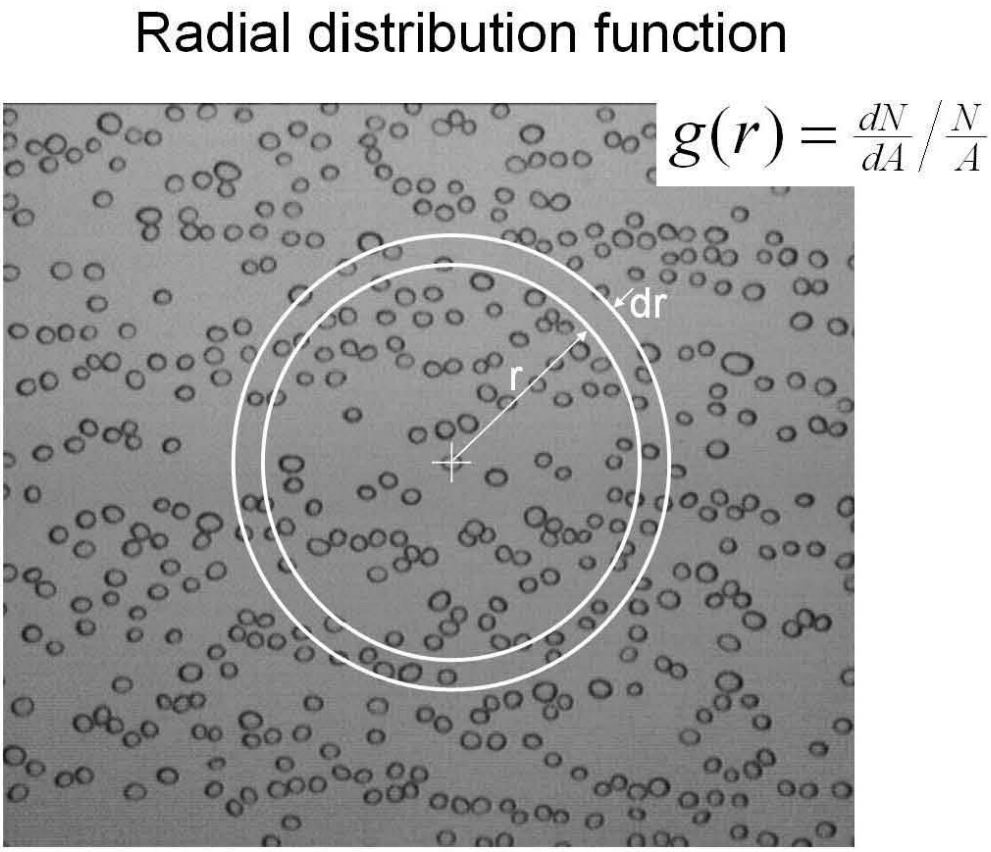

Figure 4.12: A radial element dr for a given radius r used in the calculation of the radial distribution function.

two bubbles are clustered is that the separation distance between bubbles in the line of contact direction is less or equal than two pixels (approximately 1/20 the bubbles mean diameter). This line-of-contact distance was varied up to one mean radius and the results for the lifespan did not show much sensibility to this parameter variations. Bubbles and clusters velocities are also represented dimentionless as an equivalent Reynolds number Re_{eq} in Fig. 4.25. This equivalent Reynolds was calculated with the equivalent radius and the terminal velocity. In the dimentionless representation the equivalent Reynolds does not decay with the volume fraction, and the effect of viscosity is to decrease it. It can be seen that the clusters are slower than individual bubbles from this representation too.

4.5.6 Liquid velocity fluctuations

Several attempts have been made in the past to model inertial bubbly flows, specifically monodispersed bubbly flows for which the dual limit of high Reynolds and low Weber numbers allows for the use of potential flow theory in modelling bubbles or liquid motion. The reason for focusing our attention on velocity fluctuations are numerous: whenever an attempt is made of obtaining averaged equations of motion for a bubbly flow, just as in the case of turbulent flows[72], some terms appear, (equivalent to the Reynolds stresses in turbulence models) that depend on velocity fluctuations. These terms are related to

the transport of momentum due to fluctations in the velocity of bubbles, collisions, and hydrodynamic interactions. Since these averaged equations are usually developed from the assumption that the velocity field is the sum of a deterministic part plus a stochastic part, the structure of the latter is of interest in many situations. There is a previous work which is closely related to our investigation: Zenit, Kock and Sangani[80] measured the liquid and bubble velocities for a bubble monodispersed suspension usin a dual impedance probe. They also calculated a first approximation for the liquid velocity variance, using the potential of a single bubble rising through a liquid at rest. By calculating the squared velocity disturbance on a single bubble, multiplying it by the number density and integrating over all the space, they obtained:

$$\langle u_x^2 \rangle = \frac{1}{5}\alpha u_b^2 \tag{4.5}$$

$$\langle u_y^2 \rangle = \frac{3}{20}\alpha u_b^2 \tag{4.6}$$

where u_b is the bubble velocity relative to the liquid.

There are other attempts to evaluate the velocity fluctuations, in order to obtain more accurate estimates for the quantities involved in calculations for averaged equations. Van Wijngaarden[72] also calculated expressions for the excess turbulent energy caused by the presence of the bubbles, and also found it to be dependent on αu_b^2. These quantities have units of energy, and usually are the only quantities that can be obtained in turbulence related experiments.

Velocity fluctuations for the thin channel were obtained using a PIV system, by generating a laser sheet in the middle plane between the two glass sheets that form the channel walls. This is the plane where the dominant components of the motion are located. We used fluorescent particles in order to avoid reflections from the bubbles surface. After an adaptive correlation and filtering, the velocity vectors were obtained, and the variances were calculated in a $60mm \times 60mm$ frame approximately, located at equal distances from the channel edges. The variance of the velocity for approximately 960 interior points in the frame were averaged to obtain the results shown in Figures 4.26 and 4.27. The vertical axis represents the velocity fluctuations for different values of the gas volume fraction normalized with the mean terminal velocity squared. The dotted lines are the equations 4.5.6. The vertical and horizontal velocity fluctuations are greater than the theoretical lower bound from these equations. The general tendency of the experimental data is in agreement with other authors[11]. Also note that the vertical fluctuations are bigger than the horizontal by a constant factor of two. In figures 4.28 and 4.29 the normalized velocity fluctuations for the vertical and horizontal orientations are presented. Bubbles velocity fluctuations are approximately two times larger than the liquid phase fluctuations. Sangani, Zhang and Prosperetti[59] studied the problem of a bubble mixture subjected to small-amplitude oscillatory motion. They calculated the normalized variance of the bubbles velocity to leading order in α as:

$$var(v_{vert})/v_b^2 = 0.275\alpha \tag{4.7}$$

where v_b is the bubble speed and v_{vert} is the bubbles vertical velocity.

The fluctuations obtained experimentaly are larger than expected from equation 4.5.6, and also larger than those reported by Bunner and Trygvasson[11] from 3D simulations. It seems that confinement has a strong effect on the bubbles velocity fluctuations. One possible reason for this is the instability of the trajectory influenced by the walls presence; a topic that will be covered more comprehensively on the next chapter.

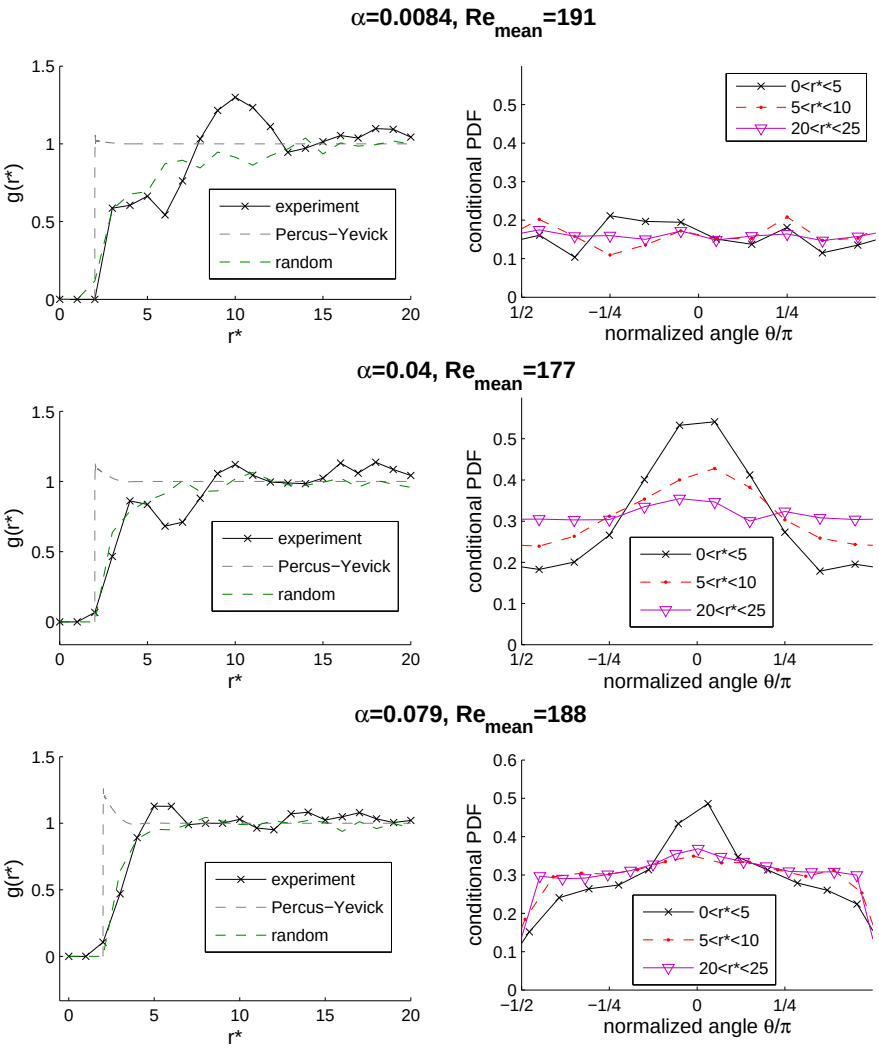

Figure 4.13: On the left, the normalized radial distribution function for increasing volume fractions. On the right, conditional PDF as function of the angle for different ranges of $r^* = r/r_m$, where r_m is the mean bubble radius. Nytrogen bubbles in water.

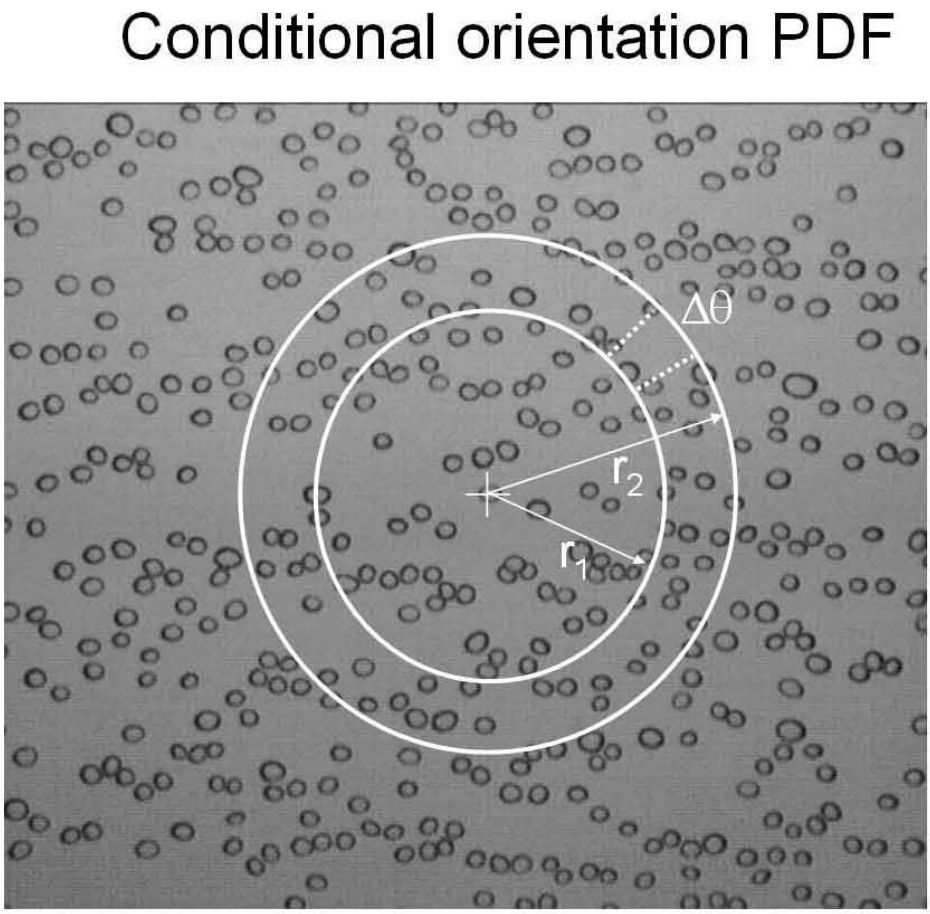

Figure 4.14: A radial element dr for a given radius r used in the calculation of the radial distribution function.

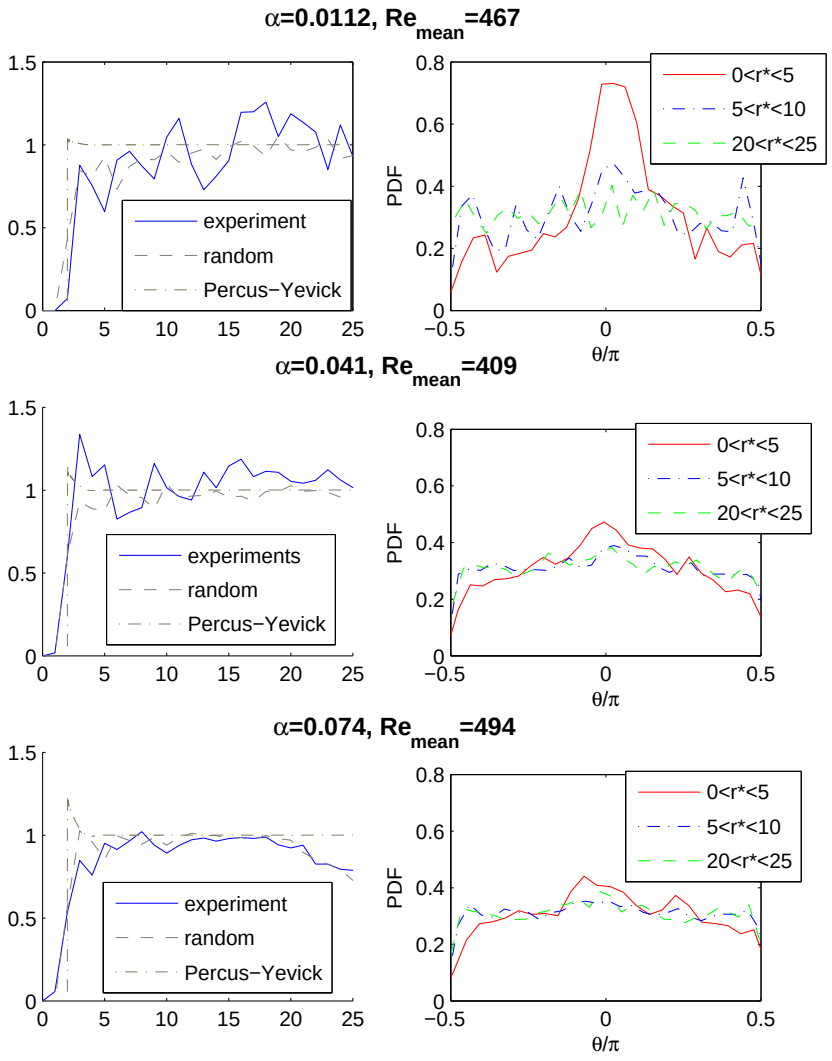

Figure 4.15: On the left, the normalized radial distribution function for increasing volume fractions. On the right, conditional PDF as function of the angle for different ranges of $r^* = r/r_m$, where r_m is the mean bubble radius. Nytrogen bubbles in water.

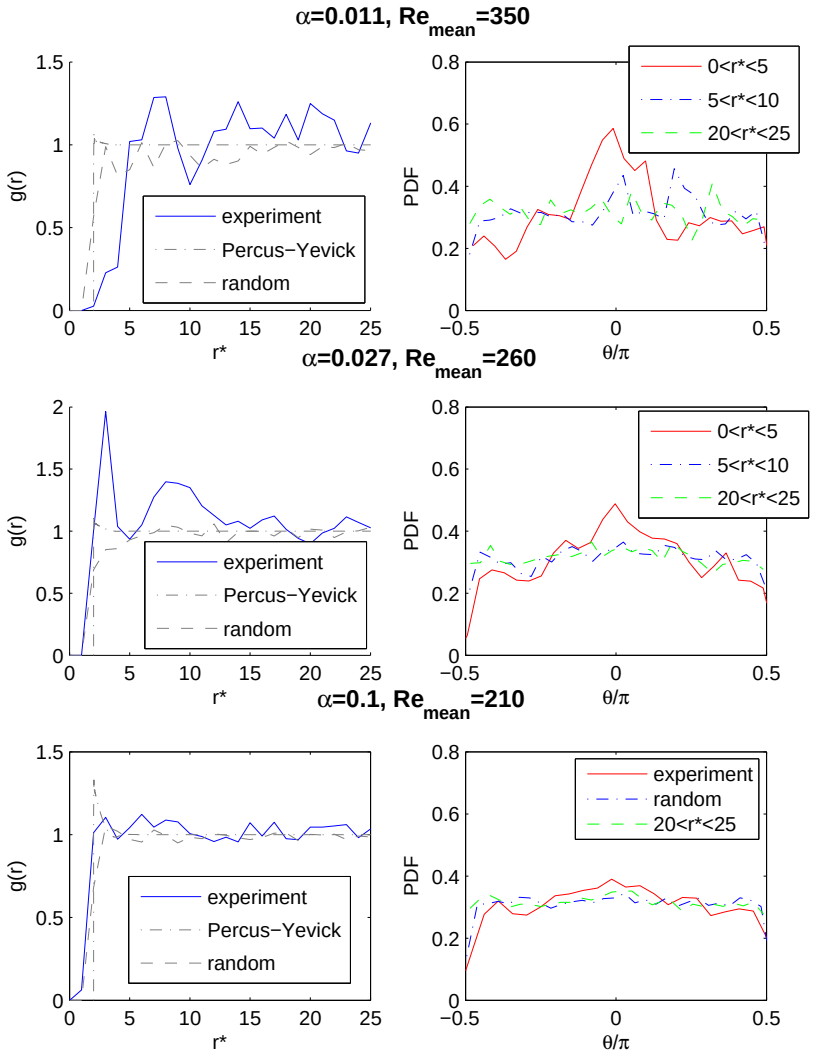

Figure 4.16: On the left, the normalized radial distribution function for increasing volume fractions. On the right, conditional PDF as function of the angle for different ranges of $r^* = r/r_m$, where r_m is the mean bubble radius. Nytrogen bubbles in a 15% weight solution in water.

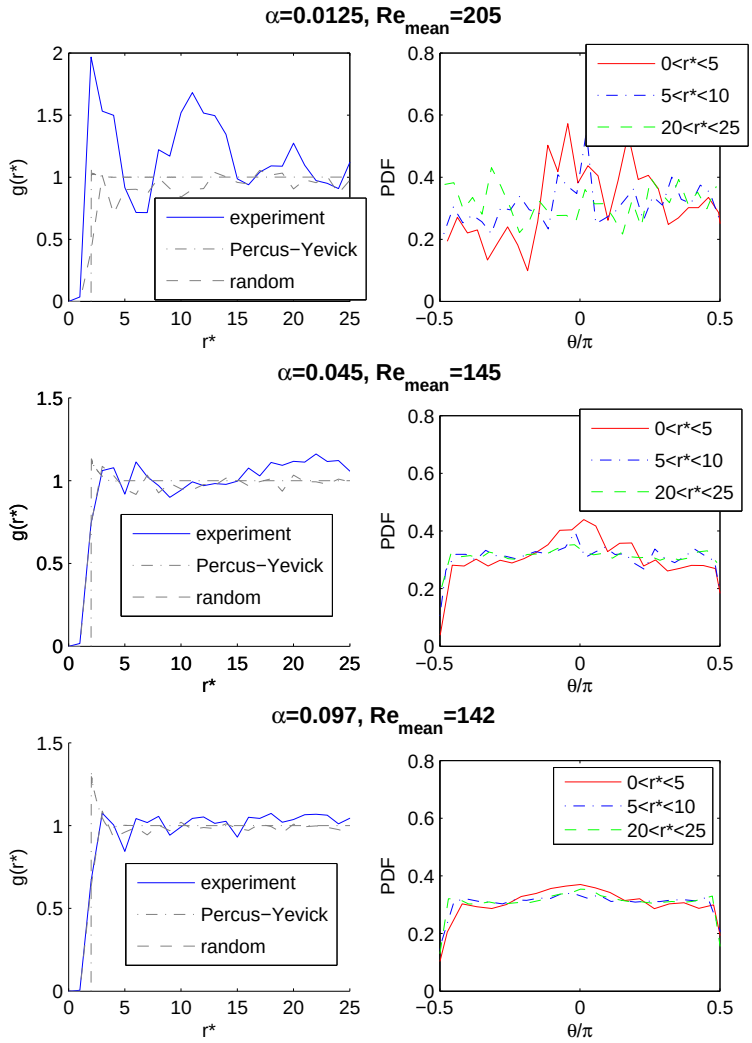

Figure 4.17: On the left, the normalized radial distribution function for increasing volume fractions. On the right, conditional PDF as function of the angle for different ranges of $r^* = r/r_m$, where r_m is the mean bubble radius. Nytrogen bubbles in a 30% weight solution in water.

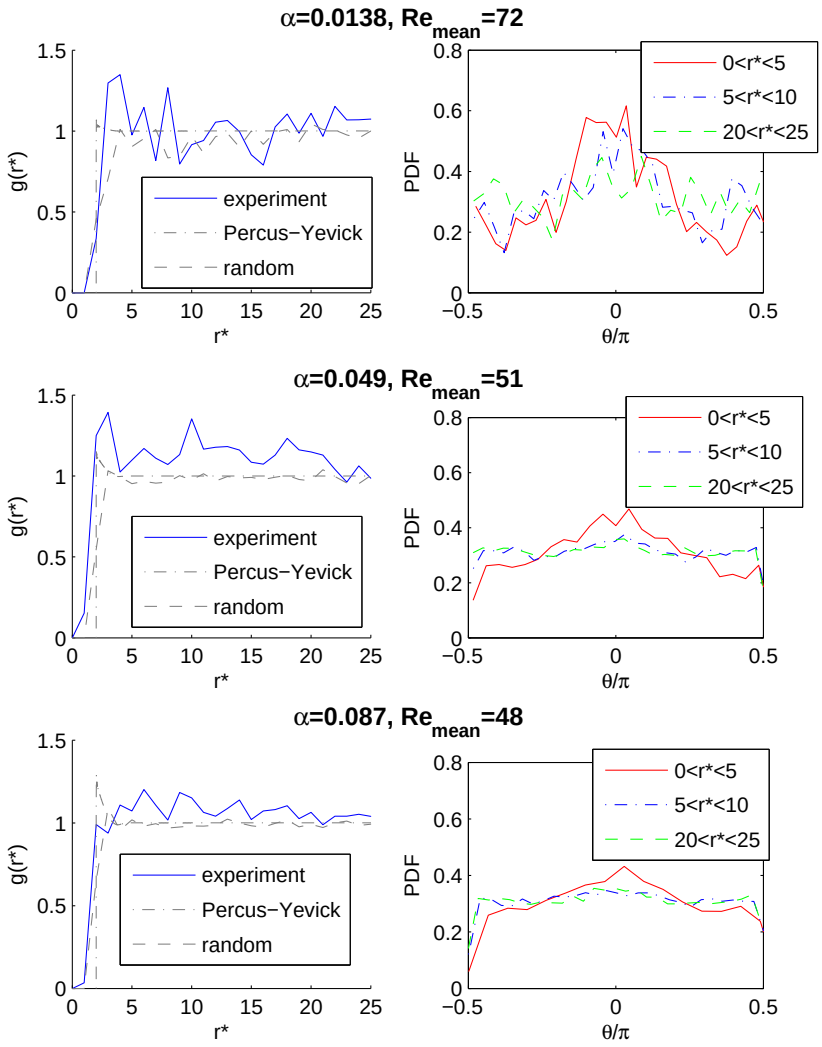

Figure 4.18: On the left, the normalized radial distribution function for increasing volume fractions. On the right, conditional PDF as function of the angle for different ranges of $r^* = r/r_m$, where r_m is the mean bubble radius. Nytrogen bubbles in a 50% weight solution in water.

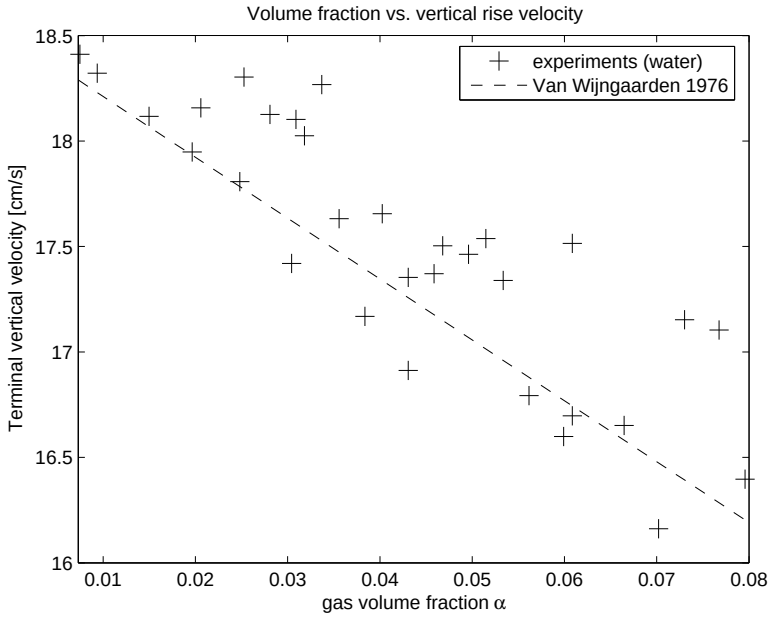

Figure 4.19: Bubble mean rise velocity versus gas volume fraction

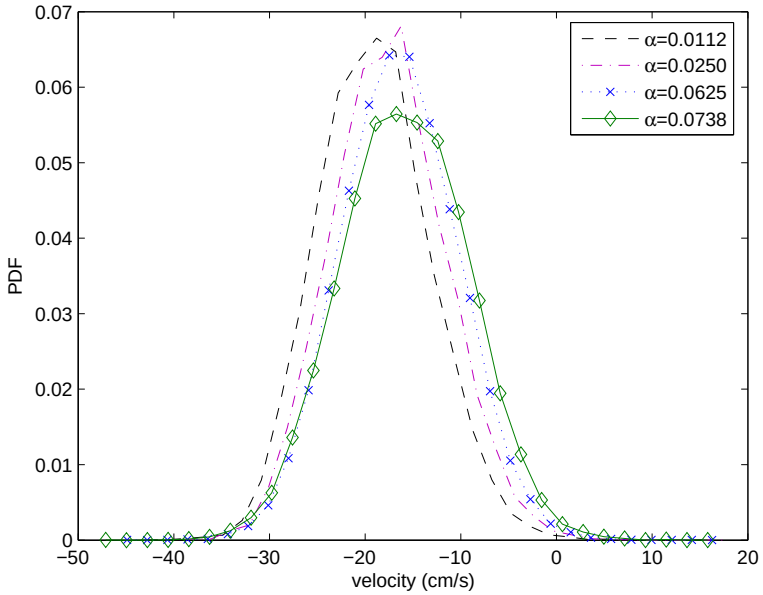

Figure 4.20: Bubble velocity PDF for different values of the gas volume fraction

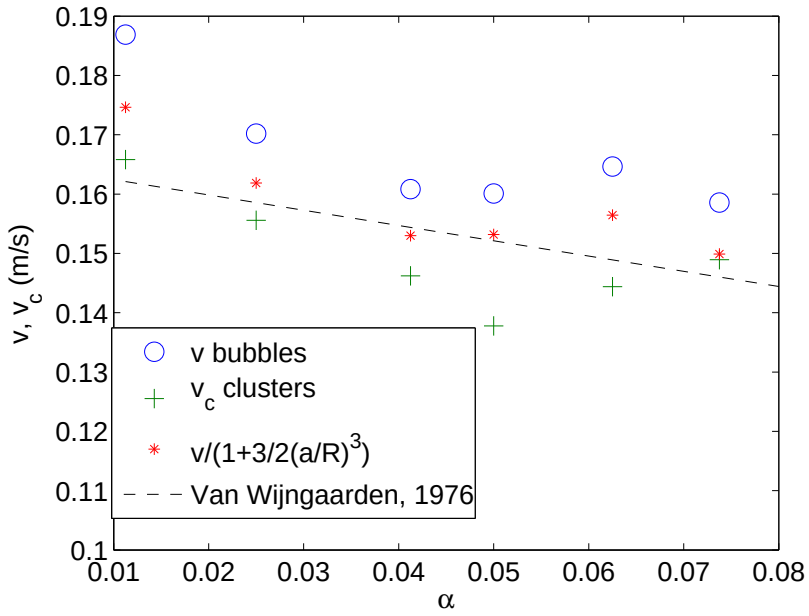

Figure 4.21: Bubbles velocity v, Clusters velocity v_c, and a prediction of the terminal velocity for a two-bubble cluster.

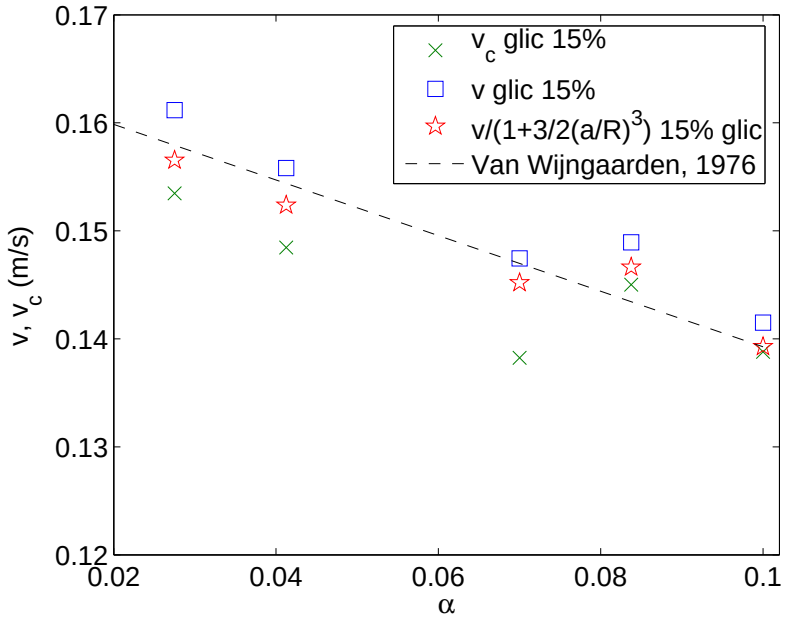

Figure 4.22: Bubbles velocity v, Clusters velocity v_c, and a prediction of the terminal velocity for a two-bubble cluster.

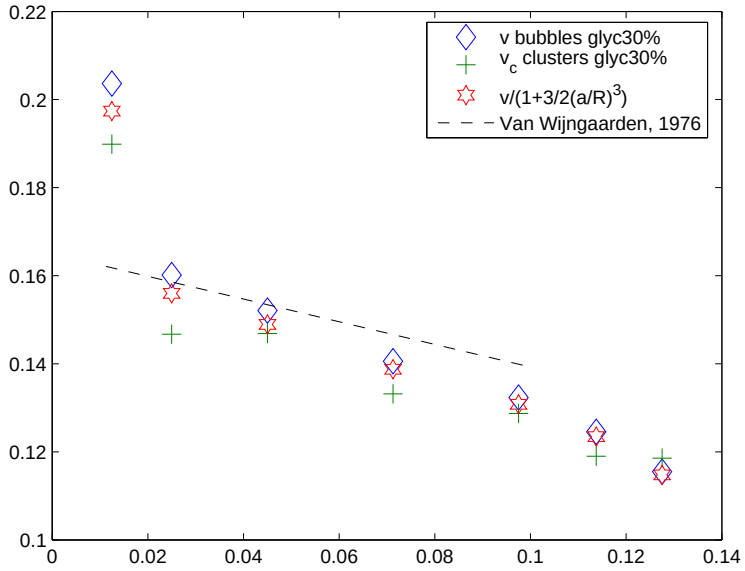

Figure 4.23: Bubbles velocity v, Clusters velocity v_c, and a prediction of the terminal velocity for a two-bubble cluster in water-glycerine 15%.

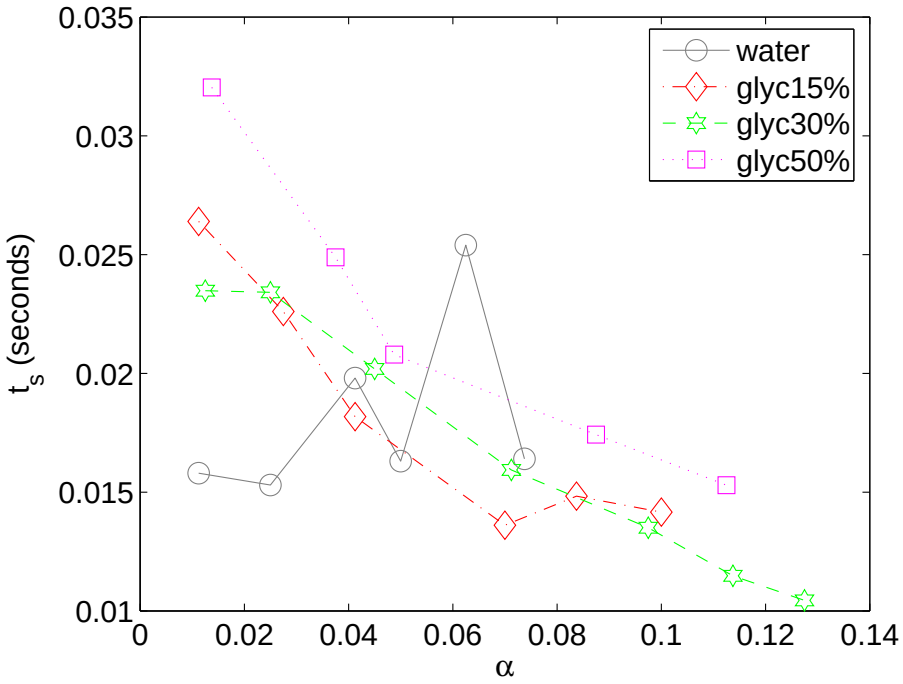

Figure 4.24: Clusters lifespan for different volume fraction α.

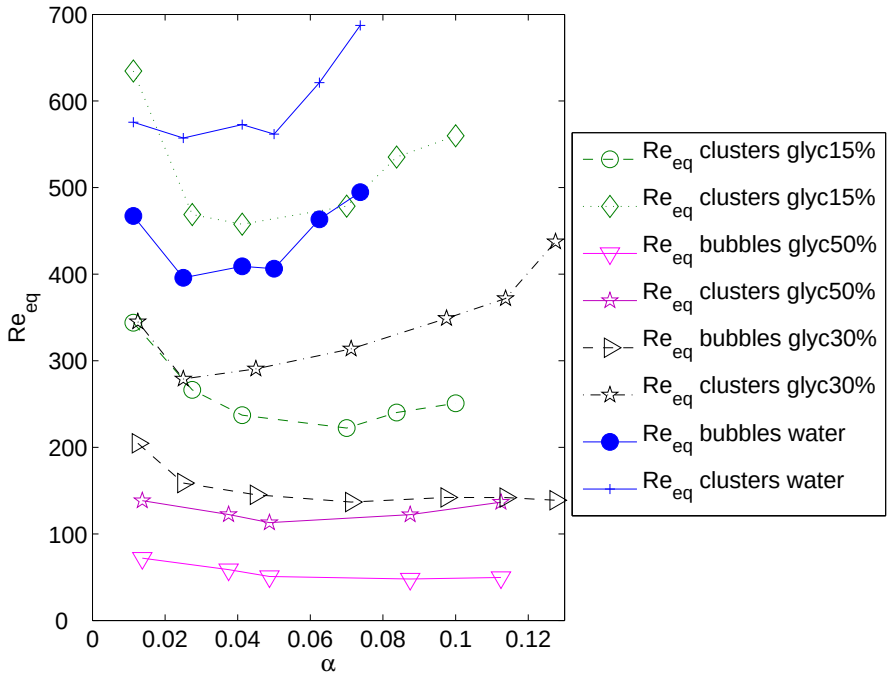

Figure 4.25: Equivalent Reynolds number for bubbles and clusters.

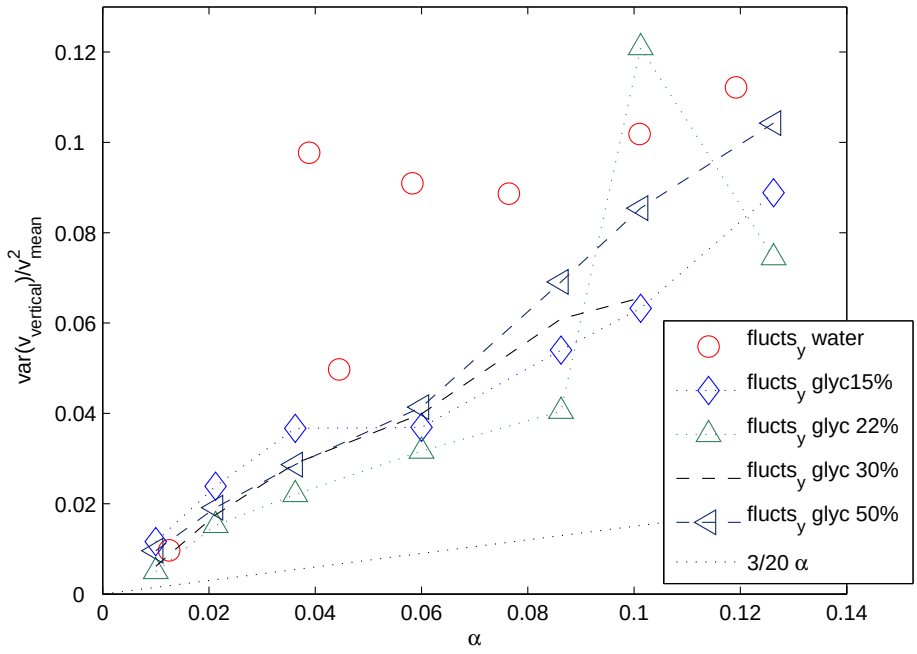

Figure 4.26: Vertical normalized velocity fluctuations.

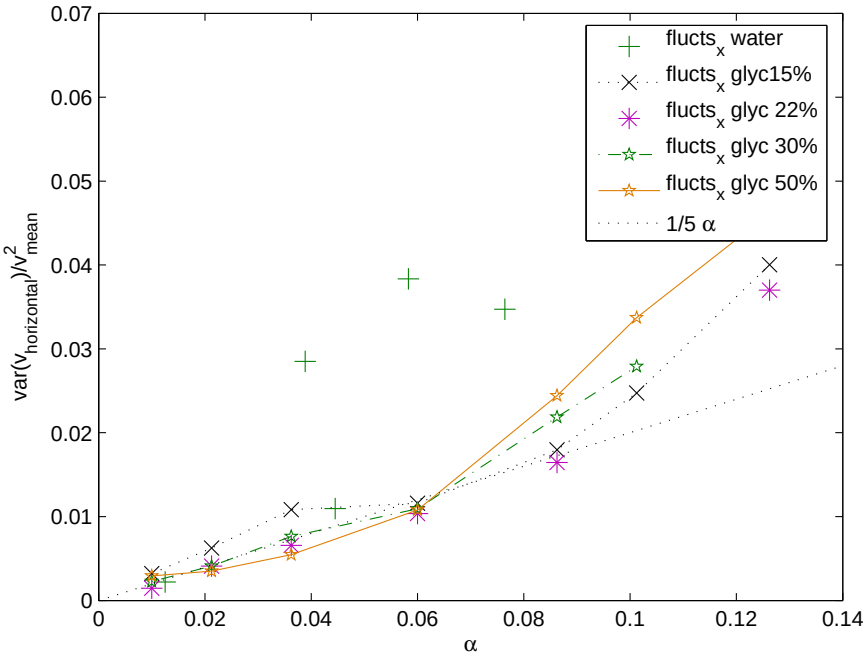

Figure 4.27: Horizontal normalized velocity fluctuations

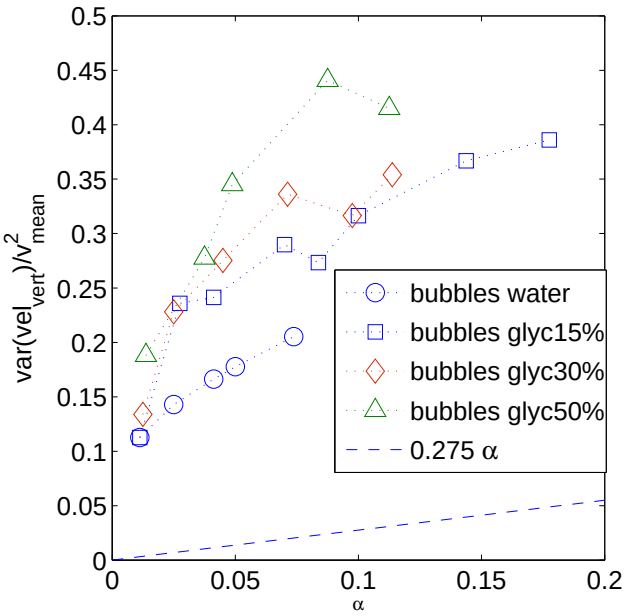

Figure 4.28: Vertical normalized bubble velocity fluctuations

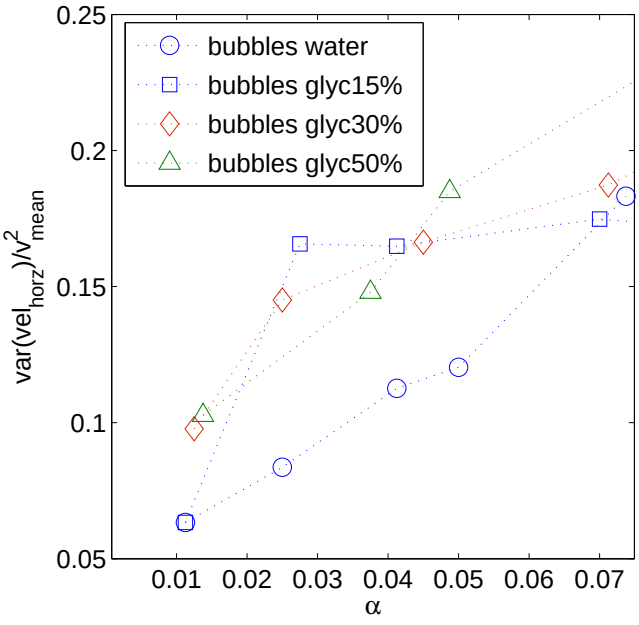

Figure 4.29: Horizontal normalized bubble velocity fluctuations

Chapter 5

The effect of confinement on the motion of a single bubble

5.1 Introduction

The motion of bubbles rising through a liquid due to buoyancy has been the subject of numerous studies. This apparently simple phenomenon has shown to be of enormous complexity, reflected in a variety of different bubble shapes and trajectories going from simple linear trajectories in the case of small spherical bubbles to zigzag and helical paths in the case of oblate ellipsoidal bubbles of slightly larger size [14]. The interest in understanding bubbly flows is widely justified by numerous engineering applications and natural phenomena. In most practical situations, bubbly flows are confined by walls or other geometrical boundaries, as is the case for underground multiphase flow in oil and gas reservoirs, where fluid motion is restricted to very confined geometries in the interior of fractures or cracks. There are many other examples of interest like microfluidics. Paradoxically, most studies have been performed for unconfined configurations. This work was motivated by the fact that thin Hele-Shaw-type channels were utilized in the past to study bubbly flow properties at the dual limit of high Reynolds and low Weber number (Chapter 4).

The effect of confinement on submerged objects has also a long history, that began with the study of slow motion of objects bearing simple geometries through liquids ($Re << 1$), while confined by walls or other physical boundaries. Bairstow, Misses, Cave and Lang[3] studied the motion of a viscous fluid through a circular cylinder confined between two parallel walls, as an application of a more general method developed therein for the solution of the biharmonic equation. The authors remark that according to their formulae, the drag for the confined cylinder, with a distance between walls five times greater than the cylinder's diameter is more than 60% greater than the unconfined drag (for $Re = 0.2$). Other similar confined problems were later addressed by Faxen[20, 21], who calculated the drag force on a sphere moving while confined between two parallel walls as:

$$\vec{F} = \frac{\vec{i_x} 6\pi\mu a U}{1 - 1.004(a/l) + 0.418(a/l)^3 - 0.21(a/l)^4 - ...} \tag{5.1}$$

Here $\vec{F}$ is the drag force, $\vec{i_x}$ is the unit vector parallel to the sphere's motion, a is the particle radius, U its velocity, and l is the distance from the walls to the center of the bubble. Let us note that the term $6\pi\mu aU$ corresponds to the unconfined drag for slow motion due to Stokes [66]. The difference between the confined and unconfined case is again greater than 60% (also for $a/l = 1/5$). These examples, among others, suggest that the effect of confining walls is of relevance, and should be further studied (see also [67]).

For high Reynolds number confined flows, there are no theoretical calculations for the drag experienced by a bubble moving between two vertical walls. The motion of a single bubble rising freely through a stationary liquid was previously studied by Levich [42, 43] and Moore[47, 48]. Based on the boundary layer assumptions, Levich considered that the flow was essentially irrotational and that the drag could be calculated from the dissipation in a nearly inviscid flow. In that way, an analytic expression for the drag coefficient C_D of a spherical bubble rising steadily through a quiescent liquid was established: $C_D = 48/Re$, where $Re = 2aU/\nu$ is the Reynolds number, a the bubble radius, U is the final velocity and the liquid's kinematic viscosity is ν. Moore[47] analysed the same problem and showed that the velocity field to leading order could be considered to be irrotational or potential everywhere in the liquid, and that the correction to this was $O(Re^{-1/2})$ in the boundary layer of thickness $O(Re^{-1/2})$ near the surface of the bubble. Moore also showed that the wake behind the bubble is small, of diameter $O(Re^{-1/4})$, in contrast to the flow past a solid sphere for which there is a boundary-layer separation causing a finite region of recirculation.

There are, however, some analytical results for the drag and lift forces acting on a bubble moving parallel to a single wall. Van Wijngaarden[70] used twin spherical expansions to calculate the velocity potential of a pair of bubbles moving through a liquid at high Reynolds number. Using similar techniques, Kok[32] calculated the potential and drag for a pair of bubbles rising through a liquid, which is equivalent to the calculation of the drag of a bubble in presence of a plane of symmetry or wall[32]:

$$C_D = \frac{48}{Re}(1 + s^3 + (3/4)s^6 + (11/3)s^8 + (39/4)s^{10} + ...) \tag{5.2}$$

where C_D is the drag coefficient and $s = a/R$ is the ratio between the bubble radius and the distance between walls R. Unfortunately single wall calculations cannot be simply added to calculate the drag for the two wall case, as was shown by Faxen, so these approximations shall not be applied without care if numerical precision is required. Moreover, for the potential flow case, the plane of symmetry assumption does not satisfy the non-slip condition at the solid wall.

The problem studied in this investigation is the motion of a single clean bubble of radius a, rising through a quiescent liquid of kinematic viscosity ν due to buoyancy, such that the drag coefficient could be calculated. The bubble is confined between two parallel walls separated by a distance R, and moves at its terminal velocity U (see Fig.5.1). This drag coefficient depends on the dimensionless distance between walls $s = a/R$, that varies from $s = 0$ in the unconfined case to $s = 1/2$ in the most confined configuration when the walls contact the bubble's surface on each side. The study focuses on the case for which

inertial forces are dominant over viscous forces ($Re >> 1$) and surface tension is dominant over inertia ($We = \rho v_b^2 d_b/\sigma < 1$), which result in nearly spherical bubbles[14].

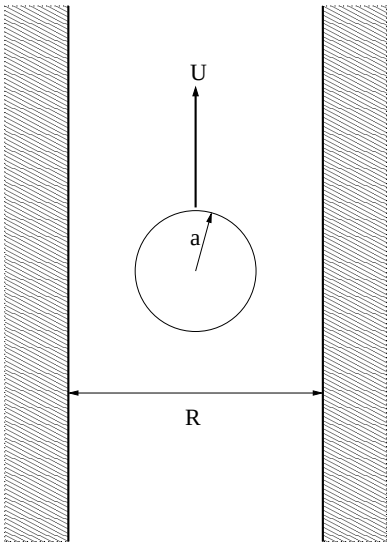

Figure 5.1: Bubble rising confined between two parallel walls.

In the following sections the theoretical and experimental investigations are discussed. The former corresponds to an analytical solution for the Laplace equation given the slip boundary conditions on an array of spheres, where symmetry planes correspond to (approximations of) plane walls. The method of Levich was used to obtain the drag as a function of infinite series of $(a/R)^n$. After a short discussion on these theoretical results, the experimental investigation is presented. The experimental setup, materials and methods to obtain the drag are discussed (section 5.3), as well as the numerical simulations (section 5.4). Results from both sections will be compared in order to attain a more complete understanding of their validity in section 5.5.1. A discussion of an unexpected phenomenon is presented in section 5.5.2.

5.2 The solution for the potential flow around a sphere confined between two walls

The problem of a confined bubble moving in a quiescent liquid is of interest for many reasons, as explained in section 1.1. The initial assumptions of $Re >> 1, We < 1$ allow for the potential flow formulation of the external velocity field. If the potential is known analytically, then it is possible to calculate a first-order approximation of the drag, as shown in section 2.6. Nevertheless, this solution is not an easy task. The symmetry of the problem will allow us to obtain an approximation from the equivalent geometry of a set of aligned spheres, separated by a regular distance R. The symmetry planes located at the middle of each pair of spheres are equivalent to the confining plane walls.

The technique employed for the solution of the Laplace equation is the same used by Kumaran in [33], where the velocity potential is initially set as an infinite series expansion

of spherical harmonics, whose coefficients are then obtained by imposing the boundary conditions.

To construct this approximation, a sphere of radius a is placed at the origin, with two image spheres aligned along a common axis crossing through their centers. This arrangement produces a potential almost equivalent to that of a sphere confined between two planes; the word almost being used because the apparent planes of symmetry between the spheres (see figure 5.2) are not real planes of symmetry. In order to be such (planes of symmetry) there would have to be an infinite arrangement of spheres aligned along the same axis, a case that will be treated in section 5.2.2.

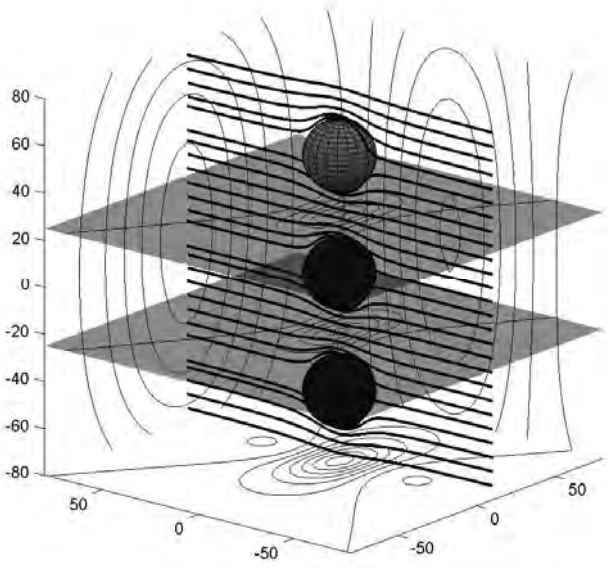

Figure 5.2: Streamlines for the flow perpendicular to three aligned spheres

5.2.1 Three spheres aligned perpendicular to the flow

Consider an arrangement of three spheres of radius a, aligned along the fixed axis z, the origin being at the center of the second sphere, as shown in the figure 5.3:

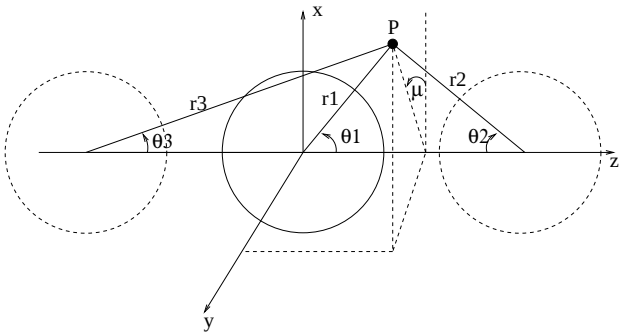

Figure 5.3: bubble with two images and corresponding spherical coordinates

The radial and azimuthal coordinates are θ_i and r_i, corresponding to a coordinate

system placed at the center of the sphere i. The three systems share the same meridional angle μ.

The velocities of the three spheres are considered to be the same, as well as their radii. The bubble's velocity is parallel to the x axis, represented by the vector $\vec{U} = U\vec{e}_x$.

Let us assume a solution of the form:

$$\phi = Ua \cdot \sum_{n=1}^{\infty} \left\{ B_n^1 (\frac{a}{r_1})^{n+1} P_n^1(\cos\theta_1) + B_n^2 (\frac{a}{r_2})^{n+1} P_n^1(\cos\theta_2) + B_n^3 (\frac{a}{r_3})^{n+1} P_n^1(\cos\theta_3) \right\} \cos\omega \tag{5.3}$$

Since the velocity decreases to zero at large distances from the bubbles, only the decaying harmonics are retained [33], and the potential is expressed as a function of the bubble separation and velocities. The constants B_n^1, B_n^2 and B_n^3 will be obtained by substitution on the non penetration boundary condition 2.40:

$$\frac{\partial \phi}{\partial r_i}|_{r_i=a} = U \sin\theta_i \tag{5.4}$$

where the projection of the bubble's velocity on the surface's normal vector has been calculated using the radial velocity in spherical coordinates, and the subscript i represents the surface of the bubble i, for the values $i = 1, 2, 3$.

This velocity potential is defined in terms of three different sets of coordinate systems $(r_i, \theta_i, \omega;\ i = 1, 2, 3)$. Depending on the boundary conditions to be satisfied at the surface of each bubble i, it is necessary to express the potential as a function of the corresponding set of variables (centered at the origin i). To do this, the series expansion derived by Hobson [24] can be used:

$$(\frac{1}{r_i})^{n+1} P_n^m(\cos\theta_i) = (\frac{1}{R})^{n+1} \sum_{q=m}^{\infty} \binom{n+q}{q+m} (\frac{r_j}{R})^q P_q^m(\cos\theta_j) \tag{5.5}$$

which is valid for any angles i, j opposite to each other, as is the case for the angles θ_1 and θ_2 in figure 5.3, for $r_j < R$. For angles with the same orientation (θ_1 and θ_3), an equivalent expression must be obtained as follows: consider the angle $\theta_4 = \pi - \theta_1$. Since this angle is opposite to θ_3, eq. 5.5 can be used.

$$(\frac{1}{r_1})^{n+1} P_n^m(\cos\theta_4) = (\frac{1}{R})^{n+1} \sum_{q=m}^{\infty} \binom{n+q}{q+m} (\frac{r_3}{R})^q P_q^m(\cos\theta_3) \tag{5.6}$$

where

$$\cos\theta_1 = -\cos\theta_4 \tag{5.7}$$

Since θ_1 and θ_4 are suplementary angles. Introducing the parity property ([1] pp. 725):

$$P_q^m(\cos\theta) = (-1)^{(m+q)} P_q^m(-\cos\theta) \tag{5.8}$$

and replacing equations 5.7 and 5.8 into the left hand side of equation 5.6 we have:

$$(\frac{1}{r_1})^{n+1}P_n^m(\cos\theta_1) = (\frac{1}{R})^{n+1}\sum_{q=m}^{\infty}\binom{n+q}{q+m}(\frac{r_3}{R})^q(-1)^{n+1}P_q^m(\cos\theta_3) \quad (5.9)$$

For the case of r_3, θ_3 as a function of r_1, θ_1 it can be shown, using the same procedure that the factor introduced is $(-1)^{q+1}$.

Substitution of 5.3, 5.5 into 5.4, for $i = 1, 2, 3$ leads to:

$$Ua \cdot \sum_{n=1}^{\infty}\left\{-B_n^1(n+1) + \sum_{q=1}^{\infty}(B_q^2 + (-1)^{(n+1)}B_q^3)\binom{n+q}{n+1}q(\frac{a}{R})^{n+q+1}\right\}Y_n^1(\theta,\omega)$$

$=\mathrm{U}\delta_{1n}Y_n^1(\theta,\omega)(5.10)$

$$Ua \cdot \sum_{n=1}^{\infty}\left\{-B_n^2(n+1) + \sum_{q=1}^{\infty}(B_q^1 + \frac{B_q^3}{2^{n+q+1}})\binom{n+q}{n+1}q(\frac{a}{R})^{n+q+1}\right\}Y_n^1(\theta,\omega)$$

$=\mathrm{U}\delta_{1n}Y_n^1(\theta,\omega)(5.11)$

$$Ua \cdot \sum_{n=1}^{\infty}\left\{-B_n^3(n+1) + \sum_{q=1}^{\infty}((-1)^{q+1}B_q^1 + \frac{B_q^2}{2^{n+q+1}})\binom{n+q}{n+1}q(\frac{a}{R})^{n+q+1}\right\}Y_n^1(\theta,\omega)$$

$=\mathrm{U}\delta_{1n}Y_n^1(\theta,\omega)(5.12)$

where s is the ratio $\frac{a}{R}$, a is the bubble's radius, R is the distance between the centers of the spheres, and $Y_n^1(\theta,\omega) = P_n^1(\cos\theta_1)\cos\omega$ (repeated indexes do not sum). The double sums in n and q allowed us for the interchange of indexes, so each side of every equation can be expressed as a function of harmonics of the same order and degree, and the following equations could be derived.

$$-B_n^1 + \sum_{q=1}^{\infty}(B_q^2 + (-1)^{(n+1)}B_q^3)\frac{n}{n+1}\binom{n+q}{n+1}s^{n+q+1} = \frac{\delta_{1n}}{2} \quad (5.13)$$

$$-B_n^2 + \sum_{q=1}^{\infty}(B_q^1 + \frac{B_q^3}{2^{n+q+1}})\frac{n}{n+1}\binom{n+q}{n+1}s^{n+q+1} = \frac{\delta_{1n}}{2} \quad (5.14)$$

$$-B_n^3 + \sum_{q=1}^{\infty}((-1)^{(q+1)}B_q^1 + \frac{B_q^2}{2^{n+q+1}})\frac{n}{n+1}\binom{n+q}{n+1}s^{n+q+1} = \frac{\delta_{1n}}{2} \quad (5.15)$$

Now, for each value n, the set of linear equations 5.13, 5.14, 5.15 establish the conditions that must be satisfied by the constants $B_{1,2,3\ldots}^{1,2,3}$ in order to give a solution that is consistent with the Laplace's equation and the boundary conditions given by eq. 5.4. An approximate solution of NQ equations by NQ unknowns can be reached if the sums for n and q are truncated, starting from the value 1 to some positive real integers N and Q respectively.

Example: For the simplest case, where $N = 1$, $Q = 1$, we have:

$$-B_1^1 + (B_1^2 + B_1^3)\frac{1}{2}s^3 = \frac{1}{2} \tag{5.16}$$

$$-B_1^2 + (B_1^1 + \frac{B_1^3}{2^3})\frac{1}{2}s^3 = \frac{1}{2} \tag{5.17}$$

$$-B_1^3 + (B_1^1 + \frac{B_1^2}{2^3})\frac{1}{2}s^3 = \frac{1}{2} \tag{5.18}$$

Then the values of $B_1^{1,2,3}$ can be readily obtained:

$$B_1^1 = -1/2\frac{(s^3-16)}{(8s^6+s^3-16)} + 8\frac{s^3}{(8s^6+s^3-16)} \tag{5.19}$$

$$B_1^2 = 4\frac{s^3}{(8s^6+s^3-16)} - 32\frac{(-4+s^6)}{(-256+129s^6+8s^9)} + 8\frac{s^3(1+4s^3)}{(-256+129s^6+8s^9)} \tag{5.20}$$

$$B_1^3 = B_1^2 \tag{5.21}$$

This constants are dependent of the $\frac{a}{R}$ ratio, in a rather complicated manner, as can be seen in this first approximation. Equations 5.19, 5.20, 5.21 will be used in section 5.2.3 to obtain the first order terms for the drag coefficient. The constats, expressed as series of s, are:

$$B_1^1 = -\frac{1}{2} - \frac{1}{2}s^3 - \frac{9}{32}s^6 + O(s^9) \tag{5.22}$$

$$B_1^2 = -\frac{1}{2} - \frac{9}{32}s^3 - \frac{137}{512}s^6 + O(s^9) \tag{5.23}$$

$$B_1^3 = B_1^2 \tag{5.24}$$

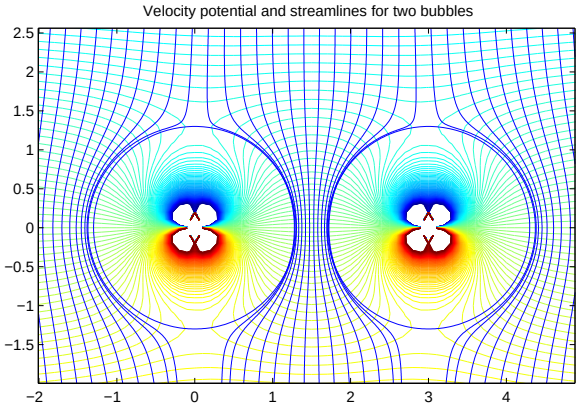

Figure 5.4: Velocity field and streamlines for two bubbles immersed in a uniform flow

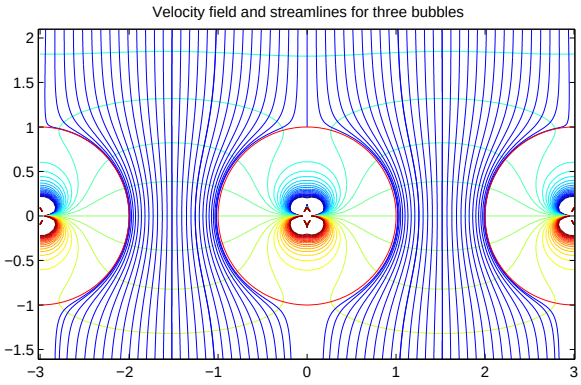

Figure 5.5: Typical velocity field and streamlines for three bubbles immersed in a uniform flow.

5.2.2 Infinite array of spheres aligned perpendicular to the flow

The generalization to the case of an infinite set of bubbles is straightforward, considering the three bubbles case. Let us consider the same geometry, being the center bubble indexed with the number zero, the next bubble to the right would be bubble one, the one to the left being bubble minus one, etc., as is shown in figure 5.6:

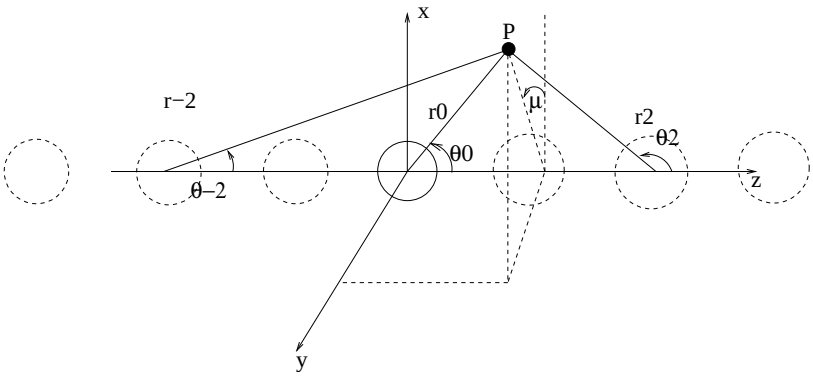

Figure 5.6: Infinite array of bubbles. The center bubble is number 0, positive and negative indexes to the right and left, respectively

The procedure would be the same as in the previous section, starting from a potential of the same form, with spherical harmonics centered at each bubble:

$$\phi = Ua \cdot \sum_{n=1}^{\infty} \left\{ \sum_{k=1}^{\infty} B_n^k (\frac{a}{r_k})^{n+1} P_n^1(\cos\theta_1) \right\} \cos\omega \tag{5.25}$$

where the index k represents the corresponding image sphere, having a spherical harmonic of order n associated to it.

Following the same steps as in section 5.2, it is possible obtain the equations for the

corresponding constants at bubble i:

$$-B_n^i = \frac{1}{2}\delta_{1n} - \frac{n}{n+1}\sum_{k\neq i}\sum_{q=1}^{\infty}\binom{n+q}{n+1}s^{q+n+1}\frac{B_q^k}{|i-k|^{n+q+1}}\xi_{ik} \tag{5.26}$$

where

$$\xi_{ik} = \begin{cases} (-1)^{n+1}; k < i \\ \\ (-1)^{q+1}; k > i \end{cases} \tag{5.27}$$

This is a linear set of NQ equations with the same number of unknowns. The velocity field coming from this solution has two real planes of symmetry at each side of the central bubble($i = 0$). If the calculation is truncated to a reasonable number of lateral bubbles, such planes of symmetry would be equivalent to plane walls. The three bubbles problem of the previous section is the case of having only the bubbles -1, 0 and 1, which can be verified by direct substitution in equation 5.26.

5.2.3 The drag as infinite series of $O[(\frac{R}{a})^n]$

In this section a first order approximation to the drag is to be obtained, by the use of series expansions of the solution for the velocity potential for three aligned bubbles. The corresponding flow is depicted in figure 5.2 and 5.5. Let us consider first the solution 5.3:

$$\phi = Ua\cdot\sum_{n=1}^{\infty}\left\{B_n^1(\frac{a}{r_1})^{n+1}P_n^1(\cos\theta_1) + B_n^2(\frac{a}{r_2})^{n+1}P_n^1(\cos\theta_2) + B_n^3(\frac{a}{r_3})^{n+1}P_n^1(\cos\theta_3)\right\}\cos\omega \tag{5.28}$$

where $r_1, r_2, r_3, \theta_1, \theta_2, \theta_3$ are the three bubbles radii and polar angles, according to fig. 5.3. Each of the lateral potentials must be evaluated in terms of the radius r_1 (and angle θ_1), in order to apply boundary condition 5.4. To that purpose the relation 5.5 is used:

$$\phi = Ua\cdot\sum_{n=1}^{\infty}\left\{B_n^1(\frac{a}{r_1})^{n+1}P_n^1(\cos\theta_1) + (B_n^2+B_n^3)(\frac{1}{R})^{n+1}\sum_{q=m}^{\infty}\binom{n+q}{q+m}(\frac{r_1}{R})^q P_q^m(\cos\theta_1)\right\}\cos\omega \tag{5.29}$$

The squared velocity is obtained performing the radial and angular derivatives of the potential from:

$$v_r = \frac{\partial\phi}{\partial r_1} \tag{5.30}$$

$$v_\theta = \frac{1}{r_1}\frac{\partial\phi}{\partial\theta_1} \tag{5.31}$$

$$v_\omega = \frac{1}{r\sin\theta}\frac{\partial\phi}{\partial\omega} \tag{5.32}$$

$$v_f^2 = v_r^2 + v_\theta^2 + v_\omega^2 \tag{5.33}$$

Performing the surface integral 2.77, and dividing by the Levich drag 2.79, it is possible to obtain a first order approximation of the relative or dimensionless drag:

	$\rho(kg/m^3)$	$\mu(\times 10^{-4} Pas)$	$\sigma(mN/m)$	Re range	We range
Fluid 1	761	4.947	16.036	$90 < Re < 470$	$0.05 < We < 2.68$
Fluid 2	818	7.771	15.455	$40 < Re < 300$	$0.05 < We < 2.06$
Fluid 3	841	17.71	12.455	$30 < Re < 100$	$0.05 < We < 1.39$

Table 5.1: Fluid properties for experimental samples.

$$C_D^{rel} = 4(B_1^1)^2 + 24(B_1^2)^2 + 16(B_2^1)^2 s^8 + 128 B_2^1 B_2^2 s^9 + ... \tag{5.34}$$

where $s = \frac{a}{R}$ is the ratio between the radius of the bubble and twice the distance to the wall (distance between adjacent bubbles), which varies from 0 to 0.5, since the minimal distance between bubbles is one bubble diameter. In the special case of a single bubble $B_1 = 0.5$, $s = 0$ and $B_{2,3}^i = 0; \forall i$, giving Levich's result.

This complicated expression can be expanded in a Taylor series as a function of s (s varies from 0 to 1/2):

$$C_D^{rel} = 1 + 2s^3 + \frac{17}{8} s^6 + ...O(s^8) \tag{5.35}$$

This expressions can be compared to eq. (8) in [40], a result obtained by Kok [32] for the drag in the case of two bubbles rising side by side under similar conditions (high Reynolds- low Weber limit). The most important contribution is precisely twice the effect of the additional bubble:

$$C_D^{Kok} = \frac{48}{Re}(1 + s^3 + \frac{3}{4} s^6 + ...O(s^9)) \tag{5.36}$$

Unfortunately expression 5.35 can not be expected to be valid for $s \to 0.5$, because the convergence of the series solution in that limit requires several terms, so this expression has validity only for $s \to 0$, in a range which is to be tested using numerical simulations.

Although eq. 5.35 may not be a good approximation for $s \to 0.5$, expression 5.34 can be used, since the values for B_i^j can be calculated numerically for any i, j, so it is possible, in principle, to improve eq. 5.35 precision and test its applicability.

5.3 Experimental investigation

The experimental setup is shown in figure 5.7. A thin channel was built using two glass sheets of approximately 20cm width and 40cm height, separated by a gap of 3.6mm. At the bottom of the channel bubbles were produced by blowing air through a capillary tube. The liquids used were silicon oil mixtures of different viscosities to avoid surface contamination. The Reynolds number ranged between 30 and 500 and the Weber numbers tested were in the range $0.05 \leq We \leq 2.7$. Properties of the used liquids are shown in table 5.1.

The shape and motion of the bubbles were captured using a high speed camera and a digital image processing software. The extent of the image was set in such a way as to

maximize the relative size of the bubble in the digital image frame, taking into account the minimum distance that the bubble would travel before attaining its final velocity.

This distance and the characteristic time needed to reach it can be calculated from a dynamic equation of motion considering the mass of the bubble to be the virtual mass and neglecting the history force. The forces on the bubble would then be the (Levich) drag force and buoyancy[19].

$$m_a \frac{dv}{dt} = \frac{4}{3}\pi a^2 \rho g - 12\pi\mu a v \tag{5.37}$$

where a is the bubble's radius, m_a is the added mass and g is the acceleration of gravity. Dividing both sides of equation 5.3 by m_a, and replacing the value for the added mass of a single bubble $m_a = 1/2(4/3\pi a^3\rho)$ leads to :

$$\frac{dv}{dt} + \frac{1}{\tau_r} v = 2g \tag{5.38}$$

here the characteristic time τ_r is defined as

$$\tau_r = \frac{1}{18}\frac{a^2}{\nu} \tag{5.39}$$

Finally, solving for the velocity gives

$$v = U_f(1 - \exp(-t/\tau_r)) \tag{5.40}$$

Being $U_f = 2g\tau_r$ the final rise velocity, and ν the kinematic viscosity of the fluid. This velocity can be integrated with respect to time to give the distance traversed by the bubble before reaching 95% of the final velocity U_f ($t = 3\tau_r$), which is shown in figure 5.8 for different values of the kinematic viscosity. This distance varies from a few centimeters (approximately 8 mm for a bubble with a diameter of 1.4mm and $\nu \approx 2.1$ cSt) to a few millimeters for smaller bubbles and viscosities.

Once the distances and focus were calibrated, the rise velocity was measured using sequences of images, such as the one depicted in figure 5.9. These images were digitally treated and transformed to binary images. A computer program was developed using *Matlab*© to identify the bubble and measure its shape and velocity.

Fig. 5.10 shows the rise velocity v as a function of the distance travelled by the bubble's centroid. It can be observed that the final rise velocity is attained before traversing 4mm (approximately $s = 1/4$). The biggest (i.e. the fastest) cases are presented; hence the distance for which the terminal velocity is reached in the case of smaller bubbles is within the same range. The terminal velocities obtained were verified using a second ordinary camera (30fps) that captured much longer trajectories. The uncertainty in the measurements was less than 5%.

The bubble shapes obtained for this experimental setup were oblate ellipsoids with aspect ratios (major to minor semiaxis ratio) χ, that varied between 1 to 1.3. In order to evaluate the effect of confinement on the drag coefficient, the terminal velocity U_f and the major and minor bubble's semiaxis $\hat{R}$ and $\hat{r}$ were measured for different bubble sizes and wall separations. The density and viscosity of the fluid were measured for each liquid.

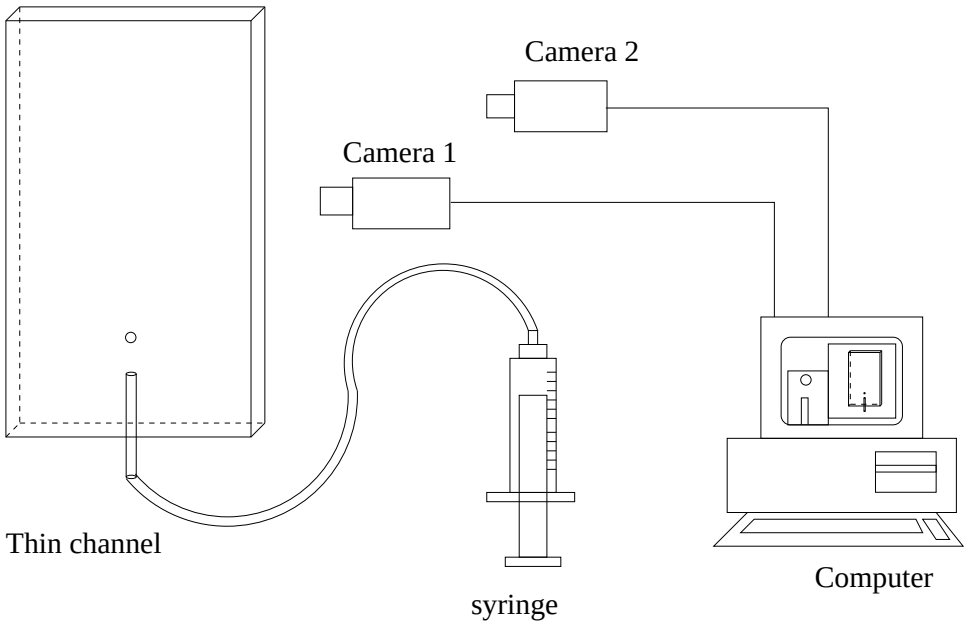

Figure 5.7: Experimental setup.

The experimental drag coefficient was evaluated from a steady force balance between buoyancy and drag:

$$F_D = \rho g(\frac{4}{3}\pi\hat{R}^2\hat{r}) \tag{5.41}$$

Using the definition of drag coefficient:

$$C_D = \frac{F_D}{\frac{1}{2}\rho U_f^2 A} \tag{5.42}$$

where $A = \pi\hat{R}^2$ is the projected area of the bubble, we have

$$C_D = \frac{8}{3}\frac{\hat{r}g}{U_f^2} \tag{5.43}$$

The values of the drag coefficient were normalized with the corresponding value of an unconfined bubble. The experimental drag coefficient was divided by the predicted value for an oblate ellipsoid(Moore[48]):

$$Cd^* = \frac{C_D}{C_{DMoore}} \tag{5.44}$$

where C_{DMoore} is:

$$C_{DMoore} = \frac{48}{Re}G(\chi)\left\{1 + \frac{H(\chi)}{Re^{1/2}} + O(Re^{-5/6})\right\} \tag{5.45}$$

where the function $G(\chi)$ is defined as

$$G(\chi) = 1/3\chi^{4/3}(\chi^2-1)^{3/2}[(\chi^2-1)^{1/2} - (2-\chi^2)sec^{-1}\chi]/[\chi^2 sec^{-1}\chi - (\chi^2-1)^{1/2}]^2 \tag{5.46}$$

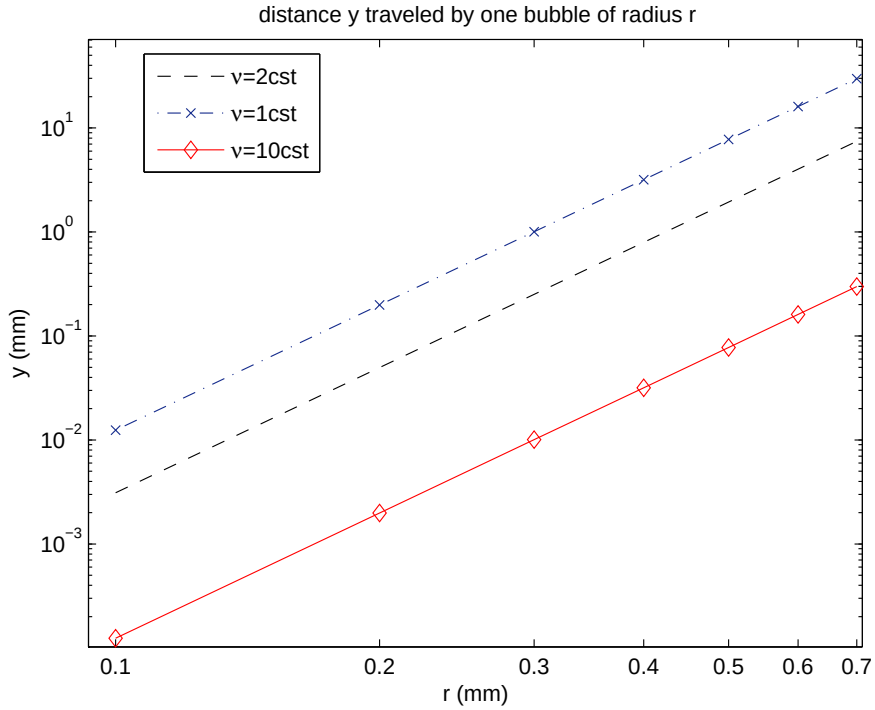

Figure 5.8: Distance traversed by an air bubble before attaining its final rise velocity

Here the function $H(\chi)$ was obtained performing a numerical interpolation of TABLE 1 from reference [48].

5.4 Numerical Investigation

The analytical calculation of the drag for the case of a confined bubble is a difficult task.The simplification considered in section 5.2 results in predictions that do not account for the non-slip condition at the wall. Moreover, some variables cannot be measured directly. Simulations can provide, in this case, a solution to validate and evaluate flow measurements.

The simulations were performed using the numerical code JADIM. This code has been extensively validated on several fluid dynamics and heat transfer problems in the past[39]. The code solves the full Navier-Stokes equations for a fluid with constant viscosity and density.

5.4.1 The JADIM code

The equations that describe the physical problem of interest are the conservation of mass, momentum and energy. They are coded in an absolute reference frame following an Eulerian flow description for an incompressible newtonian fluid. The dynamic viscosity μ, density ρ and kinematic viscosity $\nu = \mu/\rho$ are considered to be constants. These equations are represented in orthogonal curvilinear coordinates so they are adaptable to different ge-

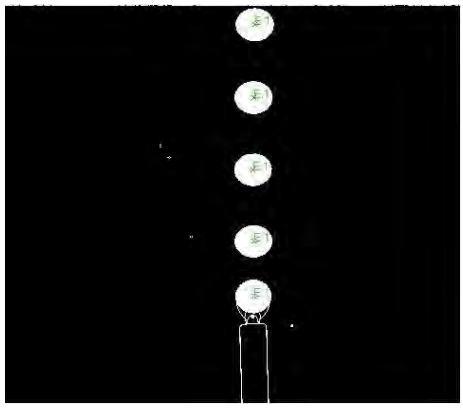

Figure 5.9: Sequence of positions for a bubble in transitory motion (250fps). The 1mm capillary edge can also be observed.

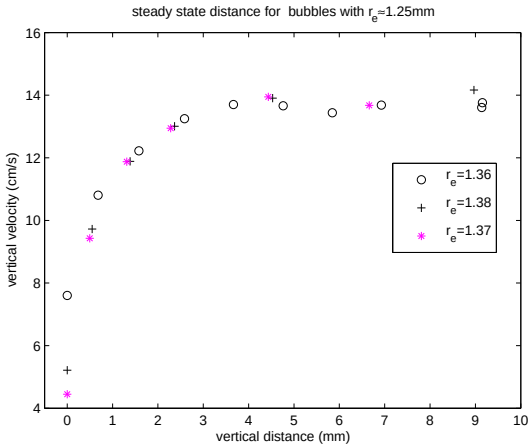

Figure 5.10: velocity vs. distance traveled for different values of the equivalent radius r_e (250fps)

ometries (like spherical obstacles, or any other axisymmetrical form, canals, ducts, etc...). This coordinate frame choice also allows for the solution of the equations in presence of deformable interfaces, so it gives direct access to normal and tangential magnitudes (velocity components, pressure, ...). The orthogonality property implies the restriction to a diagonal metric tensor, which means substantial simplification of the equations, the counterpart being naturally the orthogonal grid generation on every calculation point. The equations are formulated in the primitive speed-pressure variables, so it is possible to write down in an immediate form the limiting conditions, and to give access directly to speed, pressure, stresses, etc, over the domain boundaries. The discretization method is finite volumes, which is particularily adapted to the preservation of properties. The methodology is associated to a semi-implicit resolution algorithm with a fractional step. The precision in time and space is $O(\Delta t^2, \Delta x^2)$, to insure a good description for non-stationary flows.

5.4.2 Grid parameters

The grid used for the calculations must be orthogonal and the location of boundaries must coincide with the constant curvilinear lines by means of a bijective transformation between cartesian and curvilinear coordinates. The grid to be fed to JADIM is one of the most important (if not the most) inputs of the program. If this grid is correctly defined, as one chooses to increase the number of the grid points in a denser mesh, the results of the simulation should converge to the correct result (comparing with a benchmark problem whose analytical solution is known). For example, the distance between grid points in a given direction is a parameter that could influence in a very drastic form the outcome of the simulation. The grid parameters are not independent of each other; their functional relation could be very complex, so in general it is not possible to analyze the influence of one parameter's variation separately. There are many different grid parameters that have been observed to be of relevance in the particular case of a bubble confined between two walls. In figure 5.11 one quarter of the computational domain is depicted, due to axial symmetry. The y axis is parallel to the wall, at a distance $R/2$ from the center of the bubble, R being the distance between walls. The bubble's surface projection in the $x-y$ plane is divided into $Nang$ arc elements, and an equipotential intersects the unit circle ($r = a$) at each of these subdivisions. The domain is divided into nxp nodes in the x direction, and nyp in the y direction, following the streamlines and equipotentials respectively. Different combinations of the various parameters were tested, taking initial values of the parameters from previous works where JADIM was successfully applied to similar problems[40].

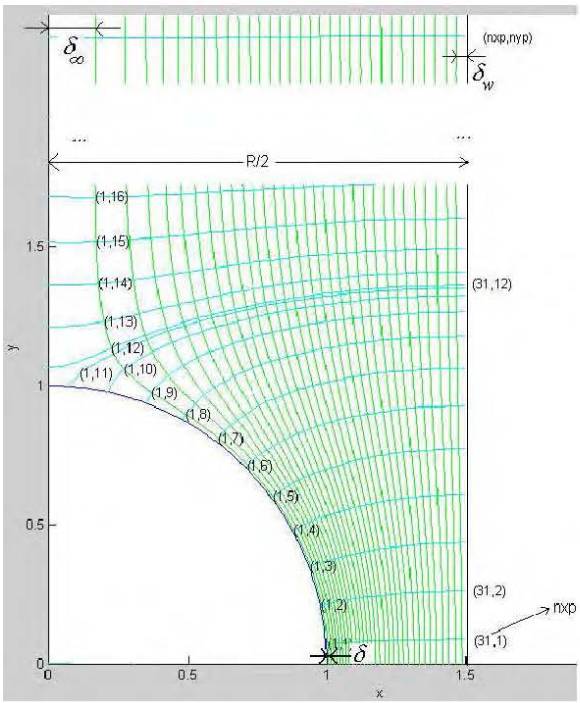

Figure 5.11: grid parameters

5.4.3 3D and 2D grids

Two types of grids were tested in numerical simulations: the *3D grid* was calculated from an approximate solution of the Laplace equation for three identical bubbles rising in a quiescent liquid at the same speed U in 3D (see section 5.2, being the planes through the midpoints between the central bubble and both lateral bubbles an approximation of two symmetry planes, i.e. vertical walls). The *2D grid* was generated from an approximation of the potential flow solution for a cylinder confined between two walls separated a distance R, aligned perpendicular to a uniform flow. This 2D potential complied exactly with the boundary conditions on the surface of the bubble and walls, and had an error of $O((a/R)^2)$ far from the boundaries. This grid has the advantage of a much smaller parameter δ_∞ than the equivalent 3D grid, as shown in figure 5.12, which also implies a better behavior in terms of smoothness in the transition from one streamline to the next on that region of the flow field.

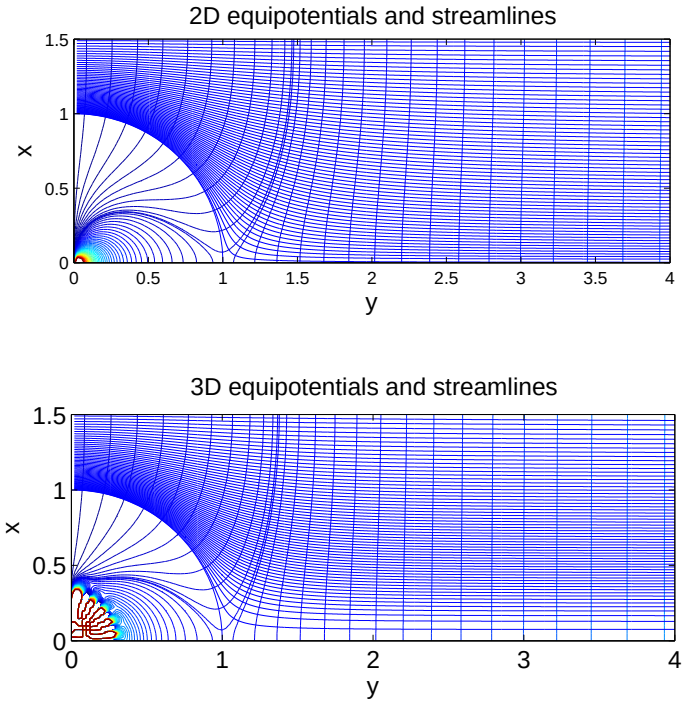

Figure 5.12: 2D and 3D equipotentials and streamlines for the an equivalent set of parameters (δ, nxp, nyp). At the lower rigth region of the graphs, the difference between the δ_∞ parameter is apparent. For the 2D grid its value is 0.02, while for 3D it is 0.07.

5.4.4 Potential and converged simulations

JADIM can report the hydrodynamic forces on the bubble for different times, in order to study the transient or steady state of the flow field. When the simulation runs until a

steady state has been reached, the solution is equivalent to a bubble ascending in a quiescent liquid at constant velocity. This situation is comparable with the theory developed by Moore[47] as in Figure 5.13. This running mode will be refered to as *converged* simulations, and is achieved by setting the number of time steps to a large value ($O(2500)$ for Re of $O(100)$). When the number of time steps is very small ($O(10)$), the viscous effects have not yet been able to transport momentum from the surface of the bubble (advection) to the bulk flow. At this moment the bubble does not have a boundary layer nor a wake, so the flow is irrotational and the drag calculated from the potential flow approximation is exact[31]. This simulation mode will be refered to as *potential* simulations, since its results should be comparable with Levich's[43], where the viscous effects in the boundary layer are disregarded. The intermediate situation corresponds to the transient behavior of the hydrodynamic interaction between the bubble and the walls, and is a very complicated matter that is beyond the scope of this investigation. This distinction is important since it would allow for the measurement of the wake and boundary layer contribution to the drag.

5.4.5 Validation

The first validation tests consisted in comparing Moore's prediction for the drag coefficient with that of a bubble between two walls, separated at a large distance from each other. The latter case must tend asymptotically to equation 5.45 as $s \to 0$. Tests were performed for different values of Re and δ. As the grid parameter δ decreases, the errors are smaller, and the simulated drag coefficient tends towards the theoretical result, as illustrated in figure 5.13. The initial values for the parameters nxp, nyp, N_{ang} were set based on previous experiences with JADIM (see [40] and references therein), and were modified in such a way that the particular conditions of the problem were satisfied.

The second validation set consisted in testing the code with higher confinement parameter values $s = 1/20, 1/10, 1/5, 1/4, 1/3$ and $1/2.6$. The grid parameter δ varied from 0.005 to 0.0001. For the tests to be successful, as δ decreases (so the mesh is increasingly denser), the resulting drag must converge to a constant value. This convergent behavior was achieved for values of the confinement less or equal to $s = 1/2.6$ in converged simulations. Potential simulations were less consistent, showing a difference of approximately 10% between 2D and 3D grids with respect to the Levich drag ($C_D = 48/Re$). A convergent behavior was observed for values of δ up to $s = 1/4$ only. The numerical simulation results are presented in the next section, and compared with the experimental results.

5.5 Results

The results of the experiments and simulations are expressed in terms of a normalized drag coefficient C_D/C_{DMoore}, obtained for different values of $s = a/R$. The drag resulted to be strongly dependent on the confinement parameter s. Results will be presented for two cases: rectilinear and oscillating trajectories.

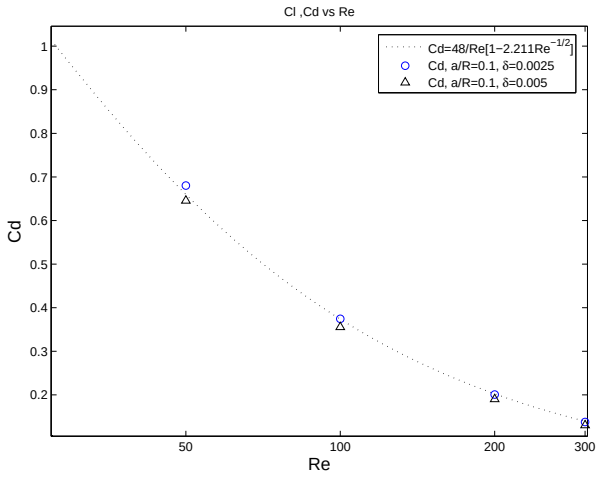

Figure 5.13: Drag coefficient for $a/R = 0.1$ as a function of Re. Comparison of the simulation with the prediciton of Moore, 1962 ($a/R \to 0$)

5.5.1 Rectilinear trajectories

The experimental, theoretical and numerical results are presented in Fig.5.14. The vertical axis represents the normalized drag C_D/C_{DMoore}, and the horizontal axis corresponds to the dimensionless distance between walls s. The crosses represent the experimental data, while the triangles represent numerical simulations. These results correspond to a range of Reynolds numbers between 30 and 100 approximately. For these experiments the trajectory of the bubble is rectilinear, and the bubble remains at the center of the channel. As s increases from $s = 0$ (unconfined case, where the normalized drag tends to unity) to $s = 1/2$ (the most confined configuration) the drag increases monotonically reaching nearly two times the unconfined drag. Although there is some scattering of the experimental data, these results are in reasonable agreement with simulations. For most experiments the drag coefficient is slightly larger than the numerical results. The numerical drag can be fitted to

$$C_D = C_{DMoore}[1 + 8s^3 + O(s^4)] \tag{5.47}$$

Note that this expression is different from that obtained by Kok (eq. 5.2). Although the functional dependence is correct, the $O(s^3)$ coefficient is different. This may be a result of the fact that only two bubbles (one wall) were considered. Also, the potential flow assumption does not satisfy the non-slip condition at the wall. The fact that a potential calculation fails is also a consequence of the omission of vorticity. Vorticity has a key role on the dissipation, and hence on the drag. The relationship between drag and vorticity has been object of study in the past. For a body in motion, immersed in a steady fluid, the vorticity is generated at the body surface. The drag is then dependent on this vorticity field, and it can be shown that (see [57]):

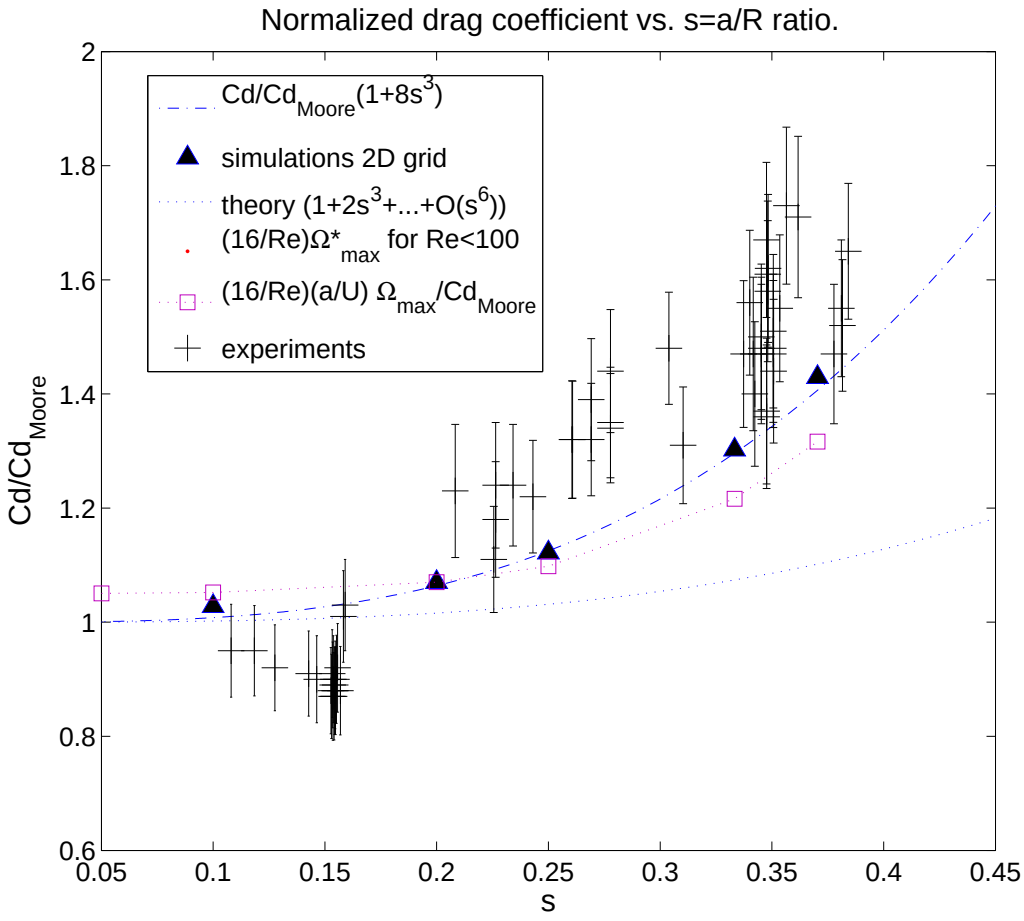

Figure 5.14: Comparison between experimental and numerical normalized drag coefficients for non oscillating bubbles.

$$D = \int_V u \times \omega dV \tag{5.48}$$

where D is the drag force, V the volume of the surrounding fluid, u the velocity field and $\omega = \nabla \times u$ is the vorticity field.

The drag for Stokes flows can be expressed as a function of the maximum vorticity Ω_{max} as follows:

$$D = -4\pi\mu a^2 \Omega_{max} \tag{5.49}$$

Legendre extended this relation to the case of finite Reynolds numbers[41]. Combining the Levich drag $D = -12\pi\mu aU$, with the maximum vorticity $\Omega_{max} = 3U/a$, gives the same result as in eq. 5.5.1. Legendre performed numerical simulations using the JADIM code, and verified that this holds true for values of the Reynolds number up to 500. By combining equation 5.5.1 with the definition of drag coefficient (eq. 2.71), the drag coefficient as a function of the maximum vorticity is:

$$Cd = \frac{16}{Re}\frac{a}{U}\Omega_{max} \tag{5.50}$$

Simulations were performed for different values of the confinement s, obtaining the maximum normalized vorticity $\Omega^*_{max} = \Omega_{max}\frac{a}{U}$ for spherical confined bubbles (for $s = 1/3$, $\Omega^*_{max} \approx 3$). This new drag can be compared with the experimental and numerical results, and is plotted in Figure 5.14, also normalized with the Moore drag coefficient. The comparison with experiments and simulations shows that the vorticity generated by the presence of the walls only do not fully explain the difference. Other source of vorticity is the oblatness of the bubbles. Legendre calculated the maximum vorticity for unconfined ellipsoidal bubbles, for different aspect ratios and Reynolds numbers. This information is plotted in fig. 5.15. The maximum normalized vorticity due to confinement is plotted in Figure 5.16. This information could be used in a combined fashion to estimate the drag, as will be the case in the following subsection.

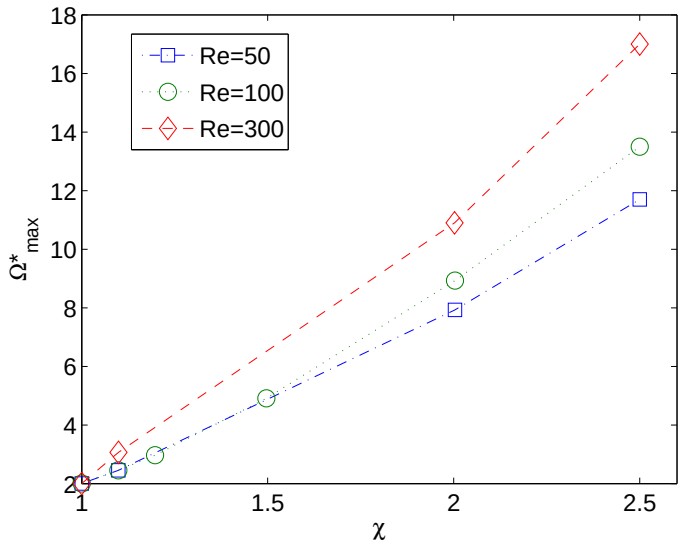

Figure 5.15: Maximum normalized vorticity Ω^*_{max} for different aspect ratio and Reynolds numbers.

The slight difference between the experimental and numerical results could be a result of the slightly oblate nature of the bubbles in the experiments.

5.5.2 Oscillating trajectories

As already mentioned in section 5.1, when a single bubble rises through a liquid driven by buoyancy, its trajectory can be rectilinear or oscillating, depending on the values of the relevant parameters[14]. The transition from rectilinear to oscillating trajectory has motivated several researchers to produce many theoretical, numerical and experimental investigations (see [49] and references therein). It has been reported that the onset of this transition occurs at Reynolds numbers of approximately 660, Weber number of approx-

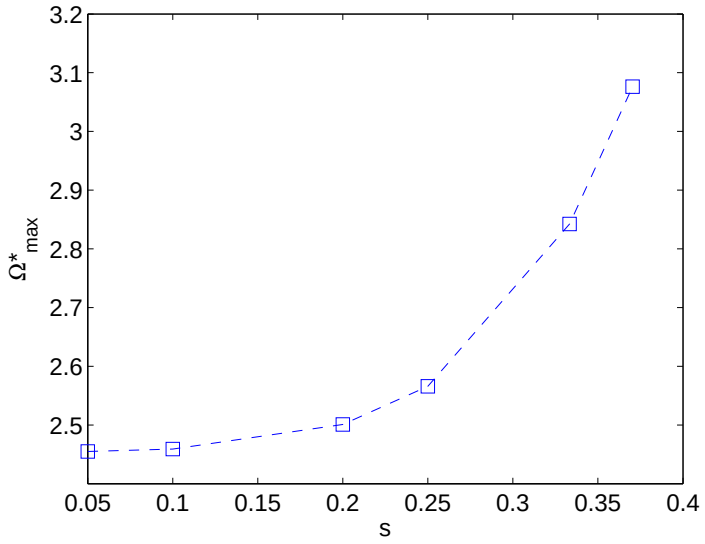

Figure 5.16: Maximum normalized vorticity Ω^*_{max} for different values of the confinement s.

imately 3, and aspect ratios of 1.8[18]. Nevertheless, small amounts of surface contamination can dramatically lower this threshold to Reynolds numbers of approximately 200. Weber numbers of the order of three had also been reported. The reason for this *path instability* is vortex shedding, according to Mougin and Magnaudet [49]. Kelley[28] performed an experimental investigation on bubbles rising in a Hele-Shaw-type channel, and also reported a critical Reynolds number of $O(10^2)$ for path instability, but his bubble wakes resemble more those of cylinders (with Kármán vortex street type phenomena) than the ones observed in free rising bubbles. De Vries[17] analyzed the wake structure of oscillating bubbles and obtained Schlieren images of wake structures for straight rising and zigzagging bubbles. The wake of the latter presented two long thin counter-rotating vortices, which had also been described by the numerical simulations of Mougin and Magnaudet. Shew, Poncet and Pinton[62] investigated the dynamics of millimeter sized air bubbles rising through still water using precise ultrasound velocity measurements combined with high speed video. They calculated the lift and drag indirectly, and hypothesized that this double threaded vortex structure is produced in a similar fashion as the wing-tip vortices present in airplane wings or rudders. They offer an explanation of the zigzag oscillations based on solid measurements and observations: the instability occurs when the two trailing vortices appear. Just as in the airplane wing-tip vortices, the bubble experiences lift because of velocity and pressure differences on both sides of its surface. As the angle between the path and vertical grows, the driving force (buoyancy) decreases and so does the velocity. At lower speeds the bubble cannot mantain the wake production, so the path curvature decreases and the wake dissipates. Since the lift vanishes under these conditions, the bubble starts accelerating due to buoyancy and the cycle starts over again with a vorticity sign reversal. This would anticipate a wake structure somehow intermittent when path instability occurs. Direct observations of the wake structures by Brücker[9]

and by ourselves (see next section) support this hypothesis.

For the case of confined bubbles the onset of oscillations has not been studied to date. We found that this onset occurs at Reynolds numbers lower than expected, compared to the case of unconfined path instability. Bubble trajectories were zigzagging for Reynolds number of approximately 100. Bubbles seem to be attracted towards the walls and even bounce back and forth from one wall to the other. The distance travelled by the bubble before the oscillation starts varies greatly, since any disturbances on the flow (like the presence of other bubbles or the wake left by previous experiments) can trigger the instability. Fig. 5.17 a) shows the positions of bubbles rising through the gap of the thin channel. For low Reynolds numbers the trajectories are straight even in the presence of other bubbles. Fig. 5.17 b) shows bubbles rising at higher Reynolds numbers, which oscillate. The zigzag paths occur in the direction of the gap (viewed from one side of the channel). The aspect ratio for oscillating bubbles varied between 1.1 and 1.8.

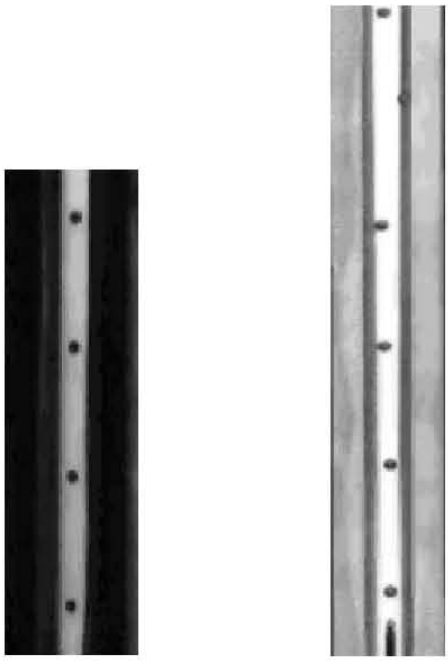

(a) **(b)**

Figure 5.17: Streams of bubbles viewed laterally through the gap between the glass sheets: a) For low Re ($Re \approx 40$) trajectories are rectilinear even in presence of other bubbles. b) For high Re ($Re \approx 110$), bubbles describe zigzag paths in the direction of the gap separation. Any disturbance on the flow triggers the instability.

5.5.3 The drag for oscillating bubbles

Experiments were performed with zigzagging bubbles on the same channel, and the drag was measured using the mean rise velocity $\bar{U}$ instead of the terminal velocity because fluctuations in the vertical direction are considerable. Fig. 5.18 shows the evolution of

vertical rise velocity, which oscillates greatly due to perpendicular motion induced by the instability. Interestingly, trajectories were always rectilinear when viewed from the front of the channel (as in Figure 5.9 on section 5.3), so bubbles seemed to experience consecutive cycles of acceleration and deceleration while ascending in a straight path. The effect of these oscillations on the drag is illustrated on Fig. 5.19, where the normalized drag coefficient C_D^* is plotted for different values of s. Measurements for non oscillating bubbles (already shown in Fig. 5.14) are marked as crosses. Circles and squares correspond to zigzagging bubbles. The drag is much larger for the latter case, reaching almost twice the corresponding value for rectilinear bubbles at the same s. This is a very significant effect that should be accounted for whenever a combination of high Reynolds number and confinement is found (say $s \geq 0.1$). The small dots in figure 5.19 represent the drag, calculated with the formula 5.5.1, with the maximum vorticity estimated from the addition of the vorticity resulting from two sources: excentricity and confinement (see figs. 5.16 and 5.15). Althoug the dots are scattered, it is clear that this estimation gives the correct order of magnitud of the drag for non oscillating bubbles, nevertheless it is unable to predict the drag for the oscillating case. The dispersion of the data is also higher in the oscillating case due to enhanced velocity fluctuations. The oscillating trajectories appearance restricts substantially the validity range for the drag obtained numerically and theoretically.

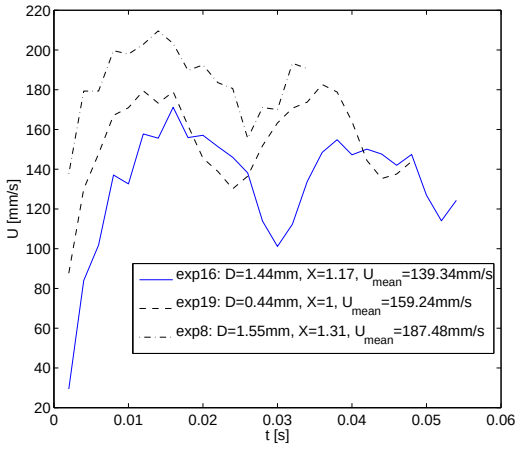

Figure 5.18: Vertical rise velocity for oscillating bubbles. The aspect ratio χ, major diameter D and mean velocity U_{mean} is shown.

5.5.4 Wall Instability

The presence of a wall near a rising bubble has already been analyzed by several authors. Takemura and Magnaudet[67] studied experimentally the lift force of contaminated and clean bubbles rising near a wall. The authors compiled several previous studies, and composed an expression for the lift force based on sound experimental, theoretical and numerical grounds (taking into account both the low and high Reynolds number limit

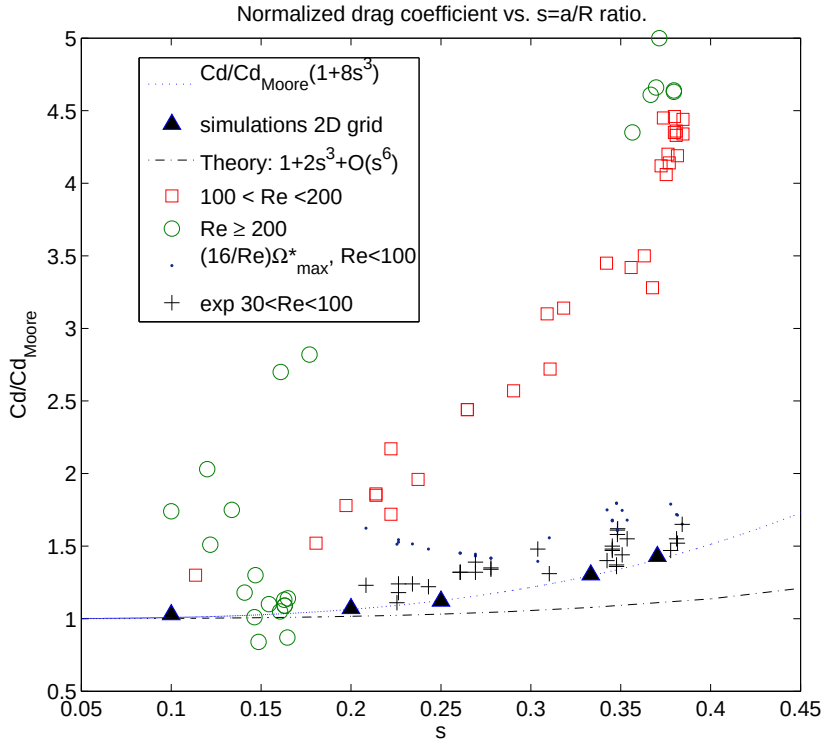

Figure 5.19: Normalized drag as a function of s for bouncing bubbles.

cases and the dynamic effects of vorticity). This expression was validated by their own experimental measurements and compared with other researchers reported results. The resulting lift is dependent on the distance to the wall and the Reynolds number. This dependency can be explained heuristically as follows: for low Reynolds numbers, viscous forces are dominant over inertial terms, and the resulting lift force between bubble and wall is repulsive (see [22]). Let us now consider a bubble rising between two vertical walls under a low Re condition: if its trajectory deviates from the centerline between the walls, the repulsive forces from both walls would tend to repel the bubble back to the centerline. This stabilizing effect makes it reasonable to expect that the confined rectilinear trajectory would be stable for low Reyolds numbers. On the other hand, for high Reynolds numbers the dominant forces are inertial in nature, and the resulting lift force is attractive[32, 70]. Again, if the bubble is rising between two vertical walls, these attractive forces would tend to drift the bubble away from the centerline. It is then expected to have a more unstable behavior for the confined bubble compared with the unconfined case for large Reynolds numbers.

In order to test this hypothesis, a plot of s as a function of Re was composed. Figure 5.20 shows regions of stability for the different cases: the onset of unconfined path instability is located at Reynolds numbers of order $O(600)$ as is pointed out in the figure by a label that reads "path instability (clean bubbles)". For dirty bubbles this region would be bounded by the line labeled "path instability (dirty bubbles)" at $Re \approx 200$.

Considering the interaction between a bubble and one wall,we used Takemura and Magnaudet's prediction for the lift force experienced by a single bubble rising near a wall[67]. Fig. 5.20 contains a contour line that corresponds to zero lift from such expression. To the right (left) of such line, the lift is attractive (repulsive). If a bubble was placed between two walls in a region of repulsive forces, the central rectilinear trajectory would be stable, as explained before. Our experimental data showed that this region is stable as expected (to the left of "two-wall stable" region). However, the region in which we observe stable trajectories extends for larger values of Re than those predicted by the expression of Takemura and Magnaudet.

The difference could be explained by the fact that vorticity has the effect of inducing repulsive forces for high confinement[67]. That effect would result in a zero lift contour located at higher Reynolds numbers than expected for the one wall case (being stronger as s increases). This is indeed the case for our experimental observations, as shown in Fig. 5.20.

In the case of high Reynolds numbers, our experimental data has revealed oscillating trajectories for confined bubbles at $Re \approx 100$ (the region labeled "2-wall unstable" in Fig.5.20), displaying a more unstable behavior than the unconfined case (path instability). This is in agreement with the explanation for high Reynolds number already presented (inertial effects produce attractive lift, which results in unstable trajectories). We consider that this unstable behavior is due predominantly to wall effects on the Reynolds number range $100 < Re < 200$. It must be noted that the boundary for stable trajectories ($Re \approx 100$) is an approximation; its exact shape is unknown.

5.5.5 Wake structure

Experimental measurements using particle image velocimetry were conducted to study the qualitative behavior of the wake for both oscillating and rectilinear trajectories. We were able to visualize the velocity fields in the planes parallel to the walls and parallel to the gap. It was not possible to obtain images on a plane perpendicular to the mean bubble velocity (see Fig. 5.21).

As mentioned previously, the wake behind a single bubble is formed by two thin vortical threads following its motion. In the case of confined bubbles these threads are aligned in a plane perpendicular to the walls. As a consequence, they are only observable through the gap in the middle of the confining walls (from the point of view of the camera to the right in fig. 5.21). Figure 5.22 shows a comparison between the wakes of bubbles rising under different conditions: to the right, we can observe the double threaded wake for a bubble with $Re \approx 100$. This bubble is in the onset of an unstable trajectory. Nevertheless, this structure is very similar to the ones observed for lower Reynolds number. The difference is that for the *two-wall unstable* region there is some interaction between both vorticity threads. In the figure, near the upper right corner we can observe a narrowing in the separation between both threads. This phenomenon was not observed for lower Reynolds number bubbles. To the left of the figure, we show the wake of a bubble that has developed the instability to its full extent. It is clear that this region where both wakes interact has

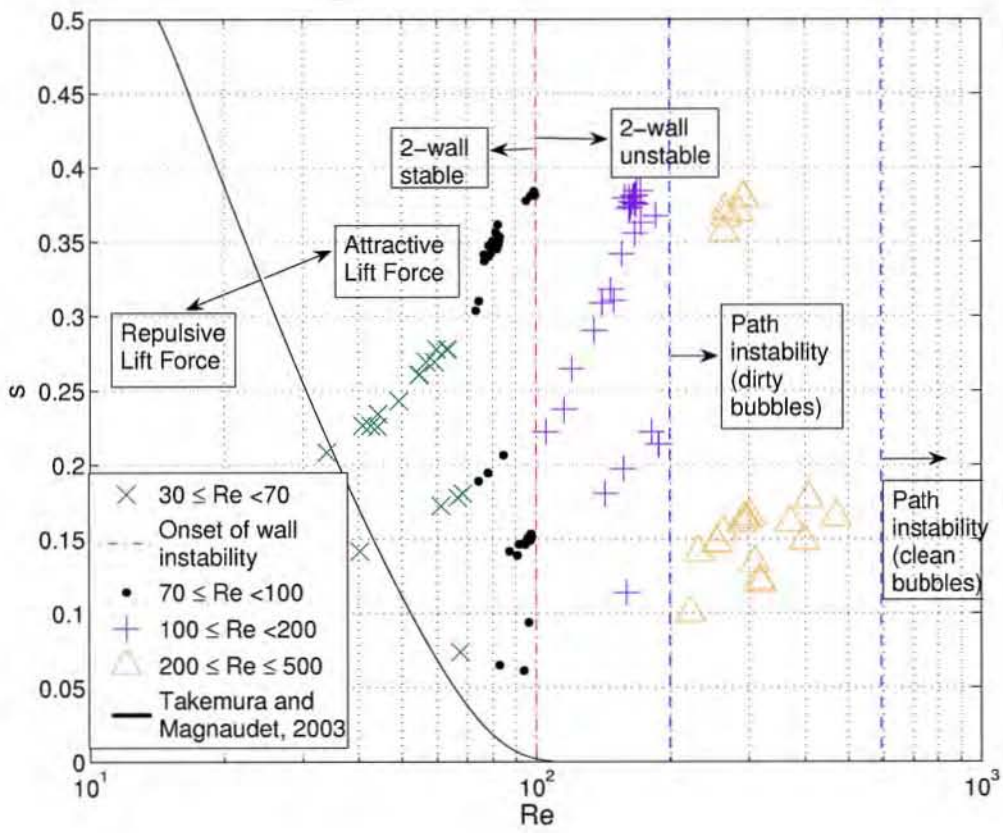

Figure 5.20: Regions of stability in the $Re-s$ plane. Comparison between path instability, wall instability and the single wall case.

collapsed the parallel thin vortical structures into a different shape (a tooth-like shape). This could also be interpreted as an interconnection between both vortex filaments into a single hairpin-like structure, as described by Brücker[9], who also attributes the unconfined path instability to vortex shedding. The way these threads interact reminds us the Crow instability in trailing vortices behind airplanes. The newly created structure has some periodicity, which we were able to observe. However, we were not able to measure it precisely, due to the temporal limitations of our PIV system.

Figure 5.23 shows the measured vorticity field (color contours) and velocity field (arrows) for one oscillating bubble. From this viewpoint (observation through the glass sheets as with the camera on the left of Fig. 5.21) the wake and bubble velocity field looks very similar to that of a stable bubble. We can observe a single long wake moving in the direction of the bubble's velocity.

When the measurements are performed through the gap between the walls, the differences between stable and unstable behavior become apparent: as explained before, in figure 5.24, the structure of the vorticity field is intermittent, as it would be if the vortical threads were spiraling. Nevertheless, frontal views as in figure 5.23 do not give any evidence of such twisting of the vortical threads. We hypothesize that these shapes result

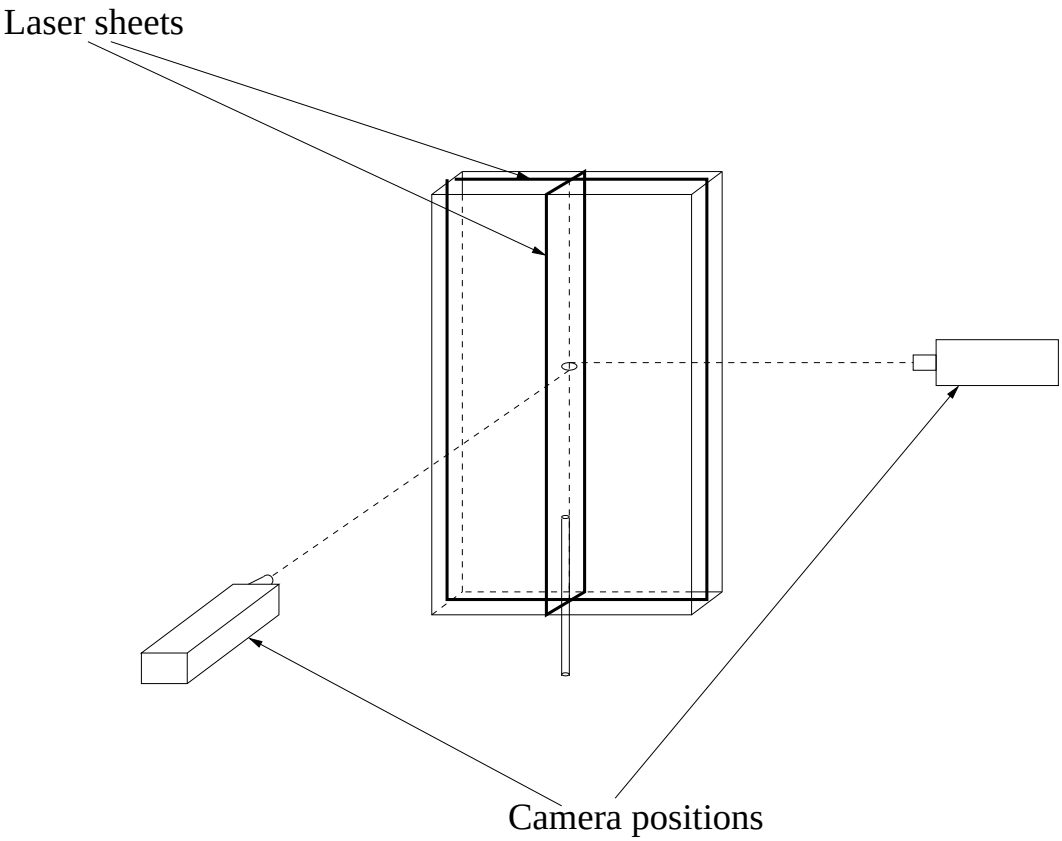

Figure 5.21: Experimental setup for piv measurements.

from periodic shedding of vortical structures[9] and also from interactions between trailing vortices as occurs between trailing vortices in airplane wings; a phenomenon known as the *Crow Instability*.

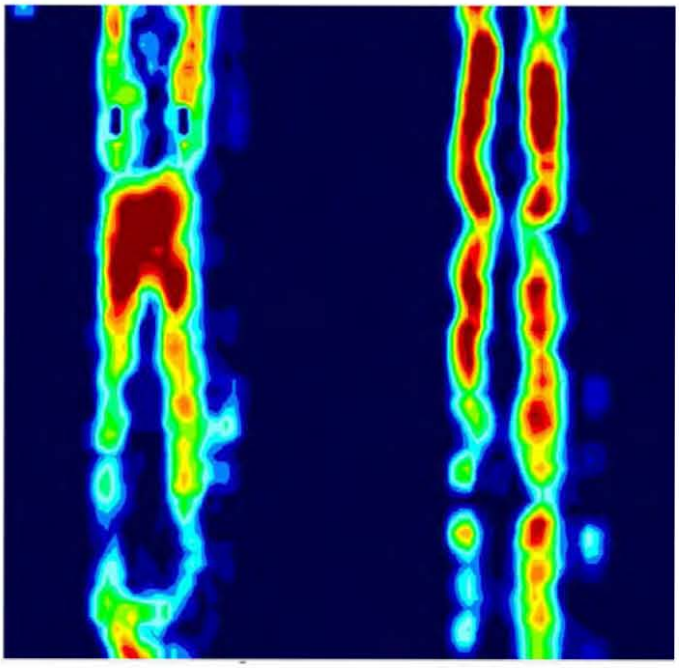

(a) $Re \approx 500$ (b) $Re \approx 120$

Figure 5.22: Comparison between the wake of an oscillating bubble (a) and that of a bubble on the instability onset (b). In these contours the colors represent the fluid speed on the plane of the laser sheet (perpendicular to both walls and the horizontal plane).

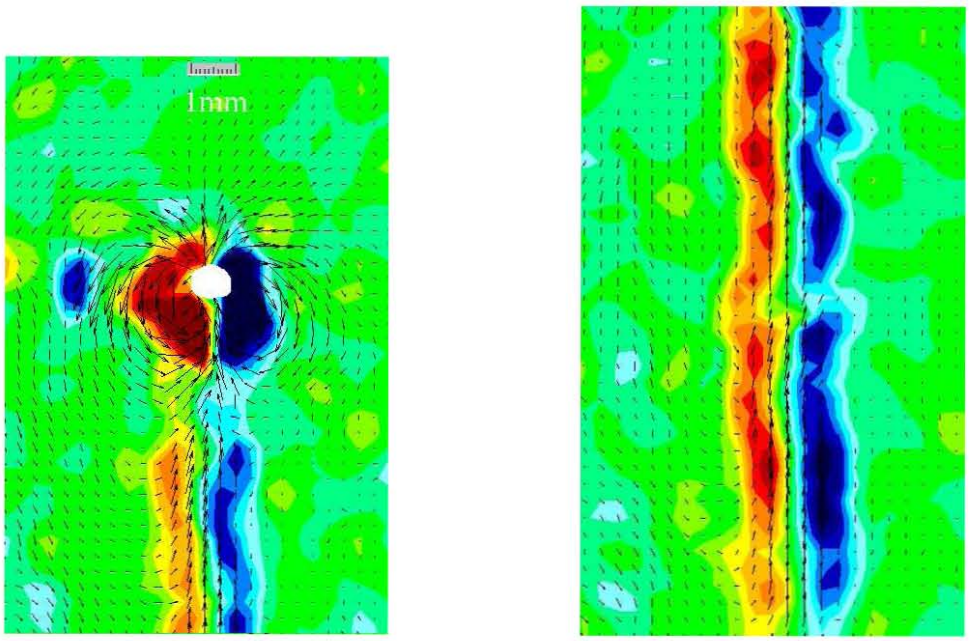

(a) **(b)**

Figure 5.23: Frontal view for an unstable bubble ($Re > 150$). Color contours represent different values of vorticity and arrows represent the fluid's velocity. (a) and (b) were taken for two different instants in time with a fixed camera (125ms between frames).

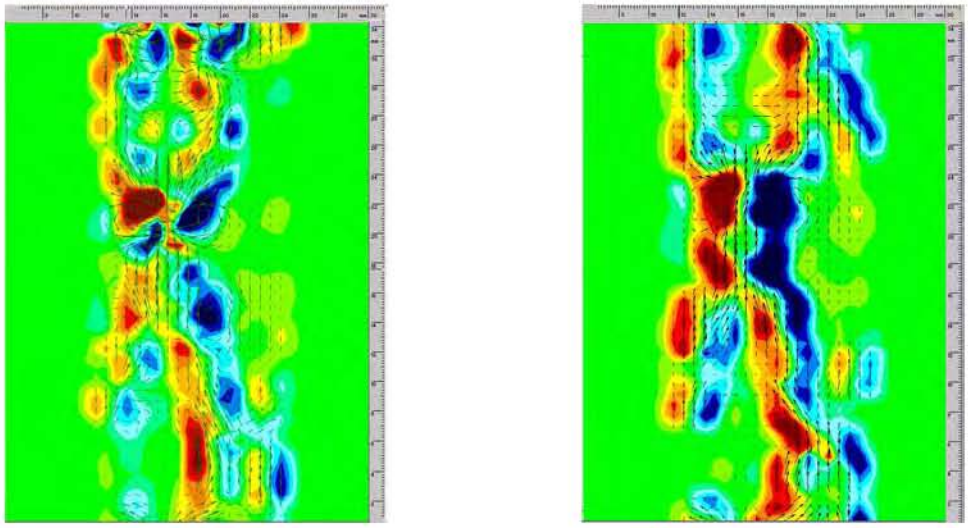

(a) **(b)**

Figure 5.24: Lateral view for an unstable bubble.($Re > 150$). Color contours represen different values of vorticity and arrows represent the fluid's velocity. Time between expo sitions 125ms.

Chapter 6

Conclusions

In conclusion, the results of this study are in agreement with those of previous works[61, 63, 10]: bubbles form clusters that tend to be aligned horizontally. It was also observed that the cluster formation is immediately followed by their breakup. This situation is contrary to the potential flow predictions. A better understanding of the forming-breaking process can only be achieved if the viscous effects are taken into account. The experimental technique proposed here allows us to obtain other important measurements such as bubble trajectories, velocity fluctuations, diffusion, etc. It was observed tha horizontal clustering starts at very low volume fractions. It reaches a maximum, and as the volume fraction continues to increase, horizontal clusters dissappear gradually. The onset of this fading process coincides with a peak in the radial distribution function. The maximum ammount of clustering was observed to vary with the Reynolds number. It tends to be smaller as the Reynolds number decreases. Clusters mean terminal velocity was shown to be lower than individual bubbles. This is due partly to inertial hydrodynamic interactions. Clusters breakup causes their mean lifespan to be shorter as the volume fraction increases. Velocity fluctuations in the vertical and horizontal directions were obtained, and have a general behavior which is in agreement previous reported investigations. In our opinion, velocity fluctuations are correlated with clustering breakup.

Since the geometry of the experiment involves bubble-wall interactions, it is important to properly evaluate the effect they have on the flow parameters and field. The effect of confinement on the drag coefficient was studied through theoretical modelling, numerical simulations, and experiments. It was found that the drag coefficient depends on the dimensionless distance $s = a/R$, where a is the bubble radius and R is the distance between walls. The form of this dependency fits closely the form $C_d/C_{d\infty} = [1 + 8s^3 + O(s^4)]$ for the case of non-oscillating bubbles. A theoretical drag was obtained using the viscous dissipation and expanding the velocity potential in series of Legendre polynomials. The dimentionless theoretical drag is: $C_d/C_{dLevich} = 1 + 2s^3 + ... + O(s^6)$. This theoretical drag is much smaller than the experimental and numerical results. The reason for this disagreement is that the theoretical analysis ommited viscous effects and vorticity.

For $Re \leq 100$, the numerical and experimental results agree well. The drag increases monotonically as s increases, reaching almost twice the unconfined drag coefficient. For

larger values of the Reynolds number, the bubble trajectory becomes unstable, in the sense that it begins to oscillate. In fact the bubble bounces back and forth from one wall to the other. This instability is different from that observed in freely rising bubbles, known as *path instability*. The difference lies in the fact that in the confined case there is a strong wall influence. The oscillations have a strong effect on the drag, causing it to increase considerably. An attempt to calculate the drag using the maximum vorticity was made. For the non oscillating case the estimated drag was of the correct order. Eventhough the combined effects of confinement and excentricity were taken into account, the drag for oscillating bubbles was underestimated.

The confinement effect on the stability of the bubble trajectory can be summarized as follows: for low Reynolds numbers, viscous forces are dominant over inertial terms, and the resulting lift force between bubble and wall is repulsive (see [22]), resulting in a stabilizing effect. On the other hand, for high Reynolds numbers the dominant forces are inertial in nature, and the resulting lift force is attractive[32, 70]. These attractive forces would tend to drift the bubble away from the centerline trajectory, resulting in a destabilizing effect. The source of this unstable behavior is different from that reported for unconfined bubbles at large Re (path instability), as it occurs at lower values of Re. The wall-induced instability is a result of the combined effects of wall-induced lift and vortex shedding. Although we have achieved an explanation of the experimental observations, a more in extensive investigation needs to be carried out in the future.

Chapter 7

Future Work

Clustering is an interesting phenomenon that is far from being completely understood. There are many topics that are still open, related with both clustering and confinement:

- To simulate pairwise interactions by the methodologies given by discrete element techniques [63, 77] considering potential flow interactions as calculated by Legendre[40], and wake effects as given by Van Wijngaarden[70].
- To perform measurements on the liquid phase (PIV) on a confined bubbly flow, to further study qualitatively and quantitatively the effect of clustering on velocity fluctuations.
- To study numerically the wall instability, by placing the bubble slightly off-centered, and then calculate the lift force. The sign of such lift would give us information on the stability of the central trajectory. Another possibility is to study the stability by perturbing the flow using standard perturbation techniques.
- To investigate the potential that governs bubble interactions through the use of the radial probability distribution $g(r)$.

Appendix A

Gauss Theorem

Let the closed surface S enclose the volume V, and let X be a scalar or vector function of position. Then, if dV is an element of volume V, and dS is an element of the surface S,

$$\int_V (\nabla X) = -\int_S \vec{n} X dS \tag{A.1}$$

where $\vec{n}$ is a unit vector in the direction of the normal to dS drawn into the interior of the region enclosed by S.

A.1 Proof

By drawing any closed surface, the volume enclosed V will be divided into elements of volume. If dV be such an element, we shall have approximately [46]

$$(\nabla X) dV = -\int_{\delta V} \vec{n} X dS \tag{A.2}$$

the integral being taken over the surface of the volume , and by summation for all the elements:

$$\int_{(V)} (\nabla X) dV = \lim_{\delta V \to 0} \sum \nabla X \delta V = -\sum \int_{\delta V} \vec{n} X dS \tag{A.3}$$

On the common boundary of any two neighbouring elements, the inward normals to each element are of opposite sign. Thus the surface integrals over boundaries which are shared by two elements of volume cancel out and we are left with the surface integral over S.

Appendix B

Grid parameters

- C_{grow}: Smoothness parameters in x and y axis. The curvilinear grid used to solve the simulations does not have a uniform separation between streamlines or equipotentials. These distances may vary depending on the need to capture specific phenomena that occur, for example, near the surface of the bubble, where the curvature and velocity gradients are important. In these regions it is recommendable to set a small distance between the mesh nodes. For regions where the opposite situation is known to occur, it is customary to use larger distances between nodes. This saves calculation time since far from the bubble the velocity gradients and curvatures are increasingly small. Establishing upper and lower bounds for this parameter assures a smooth transition in the curvilinear coordinate space, preventing numerical instabilities. Previous research with similar problems showed that the range

$$0.8 \leq C_{grow} \leq 1.2 \tag{B.1}$$

  must be used[40]. The values of the smoothness factor for x and y could be different, to account for the very dissimilar upper bounds for each direction.

- nxp: Number of pressure points in the x direction (from the surface of the bubble to the wall). This is the number of streamlines. Once this number is established, an iterative procedure will calculate the position of the nxp pressure points from the bubble's surface to the wall. The distance between these points grows according to a smoothness factor C_{growx}, such that $x_p(i) = x_p(i-1) + \Delta_{xp}(i)$, being $\Delta_{xp}(i) = C_{growx}\Delta_{xp}(i-1)$ at each step. This procedure calculates this uniformly growing series in such a way that $x_p(nxp) = x_w$, where x_w is the position of the wall.

- nyp: Number of pressure points in the y direction (from the surface of the bubble to the end of the grid). This is the number of equipotentials. Once this number is known, an iterative procedure analog to the one that calculates $nxp(i)$ generates the points where the equipotentials intersect the plane $x = 0$. The first point in this series depends on the difference between the value of the potential in the corner (0,1) -the intersection between the bubble and the plane $x = 0$- and the previous

equipotential (labeled as 11) over the surface of the bubble. The series ends at a given distance from the bubble, such that the results of the simulation are insensitive to this upper bound. Legendre [39] sets this value as approximately fourty times the bubble's radius $y_{max} \approx 40a$ (a is the bubble's radius) for $Re >> 1$ ($O(100)$), since for lower Reynolds numbers a larger grid is required.

- N_{ang}: Number of circular sectors that divide the bubble's transversal projection. In figure 5.11, there are eleven intersections between the bubble's surface and the equipotentials, labeled (1,1), (1,2), ..., (1,11), so in this case $N_{ang} = 11$.

- δ: Distance from the bubble to the first streamline. This is a very important parameter, because its size captures the flow phenomena in the vicinity of the bubble. The boundary layer, of order $O(Re^{-1/2})$, establishes an upper bound for its magnitude. In previous numerical studies[45, 40], it has been found that a value of $\delta < 0.005a$, is a good initial test value for this parameter.

- δ_∞: This is the distance from the plane $x = 0$ to the nearest streamline, far from the bubble. This parameter captures the flow in the vicinity of the plane of symmetry that passes through the middle of the bubble between the two walls. The wake and the stagnation point lie in the vicinity of this region.

- δ_w: The distance between the wall and the nearest streamline far from the bubble. This parameter allows to capture the flow dynamics near the wall. The last two parameters are generally taken to be consequence of the choice for the preceeding parameter set.

- *timesteps*: The final number of steps of time Δt that the simulation runs. If this value is large ($O(2500)$ for Re of $O(100)$), the stationary state is achieved. For the case of a bubble rising in a quiescent liquid, this corresponds to a bubble reaching a constant rise velocity.

Dependencies between these parameters are complex, and an analytical expression for the variations among them is not available.For example, let us assume that the value of δ must decrease, from $\delta = 0.005$ to $\delta = 0.0025$, in order to improve the approximation for the drag coefficient, as in figure 5.13, while maintaining the number of nodes nxp constant. Since the distance between streamlines in the y direction must increase smoothly, such distances in the vicinity of the bubble must now be smaller. But in order to keep nxp constant, C_{growx} must increase.

To illustrate these relationships, some test grids were generated, and table B.1 was composed. For distances between walls R greater than five, the number of nodes in the x direction had to be increased, because the smoothness factor limit for constant nxp would be violated. Although the value for δ_w is high for bigger distances to the wall, the behavior of the solution tends to the undisturbed bubble of Moore as R/a increases.

There are many other parameters that may affect the grid generation results significantly, that depend on the particular type of grid and numerical procedures. An example

δ_∞	δ_w	δ	R	C_{grow}	nxp
0.2213	0.0096	0.005	3	1.1417	30
0.1767	0.0412	0.005	4		30
0.1588	0.0791	0.005	5		30
0.136	0.3080	0.005	10		60
0.1859	0.0280	0.0025	3		30
0.1432	0.0630	0.0025	4	1.1756	30
0.1256	0.1095	0.0025	5		30
0.1043	0.3815	0.0025	10		60
0.1678	0.0370	0.0015	3		30
0.1267	0.08	0.0015	4		30
0.0095	0.1320	0.0015	5	1.2003	30
0.00884	0.4630	0.0015	10		60

Table B.1: Different typical values for the grid parameters. 3D approximate solution o the potential.

of this would be the number N of terms in the approximation of the 3D potential ϕ i equation 5.3, or the stepsize for the integration of the streamlines equation from the velo ities in x and y. By means of the variation of these addtional parameters it is possible t improve δ_∞ to a value near 0.04, setting the stepsize to 0.005 and calculating the potenti ϕ with 25 terms in the series, for a $\delta = 0.0006$. The cost of this improvement is of course a considerable increase in calculation time.

Appendix C

Sample programs in matlab

C.1 Program that detects the bubbles center only:

```
%this program is important because it allows the recognition of bubbles
%that are clustered, even touching each other.

areas=[];
s=struct('x',{},'y',{},'Area',{});
%,'MajorAxisLength',{},'MinorAxisLength',{});

% in case you want to discard certain onject sizes
areaminima=0;%
areamaxima=1000%

%reads all images in the directory and puts it in an array

d=dir('*.jpg');

for k=1:length(d);


I = imread(d(k).name);
k


% adjust image level and convert to binary

I2=imadjust(I,[0.1,.65]);
bw=im2bw(I2);
bw2=imcomplement(bw);
```

```
%fill holes. This fills everything but the little bubble center.
%this allows for the distinction between bubbles centers even when
%bubbles are touching each other



ii=find(bw2==0); locations=ii(1); lleno=imfill(bw2,locations);
comp=imcomplement(lleno);


%this part does the recognition and properties measurement.

[labeled,numObjects] = bwlabel(comp,8); bubble =
regionprops(labeled,'Area','Centroid','BoundingBox','Orientation',
'MajorAxisLength','MinorAxisLength','FilledArea','ConvexImage');%,'PixelList')

grandes=find([bubble.FilledArea]>areaminima & [bubble.FilledArea]<areamaxima);
bubble=bubble(grandes);

centroide=[bubble.Centroid];
%caja=[bubbles.BoundingBox];
%area=[bubbles.Area]



x=centroide(1:2:length(centroide));
y=centroide(2:2:length(centroide));

%imshow(comp)
%Shows the results over the original picture (if you wish)

imshow(I)
hold on
plot(x,y,'rx')

        for ii=1:length(x)
         text(x(ii),y(ii),['E:' num2str(ii)],'Color',[0 1 0])
        end


hold off
```

```
%figure

maximo=max([bubble.FilledArea]);



% saves properties in an array of type structure

s(k).x=x;
s(k).y=y;
s(k).Area=[bubble.FilledArea];
s(k).MajorAxisLength=[bubble.MajorAxisLength];
s(k).MinorAxisLength=[bubble.MinorAxisLength];


%saves results to movie frames
M(k)=getframe;
end

%play the movie
movie(M)
```

C.2 Program that recognizes clusters and their properties

This program recognizes objects of certain sizes and aspect ratios. It can also be used to recognize individual bubbles or clusters, depending on the chosen sizes and aspect ratios.

```
s=struct('x',{},'y',{},'Area',{});%,'MajorAxisLength',{},'MinorAxisLength',{})



areaminima=5;

areamaxima=180;%/home/student/bfigueroae/experiments/agua1000fps2/fv7cm

Xmin=.9;
Xmax=1.55;
d=dir('*.jpg');

for k=1:length(d);

I = imread(d(k).name);
k
```

```
I2=I;

I=imadjust(I,[.2 .9]);

\%this part separates the background. This background is the
\%complement of the ''glued'' bubbles.

background=imopen(I,strel('disk',1));%8));
bw=background;

bw = im2bw(background);


comp=imcomplement(bw);
comp=immultiply(comp,Mascara);

[labeled,numObjects] = bwlabel(comp,8);
bubble = regionprops(labeled,'Area','Centroid','BoundingBox','Orientation','M

\% here we separate what we want (clusters or bubbles)

grandes=find([bubble.FilledArea]>areaminima &
[bubble.FilledArea]<areamaxima &
[bubble.MajorAxisLength]./[bubble.MinorAxisLength]>=Xmin &
[bubble.MajorAxisLength]./[bubble.MinorAxisLength]<=Xmax);
bubble=bubble(grandes);

centroide=[bubble.Centroid];
%caja=[bubbles.BoundingBox];
%area=[bubbles.Area]



x=centroide(1:2:length(centroide));
y=centroide(2:2:length(centroide));

imshow(comp)
%imshow(I)
hold on
plot(x,y,'rx')
```

```
        for ii=1:length(x)
         text(x(ii),y(ii),['E:' num2str(ii)],'Color',[0 1 0])
        end


hold off


%figure

maximo=max([bubble.FilledArea]);

%hay que usar algun arreglo raro porque son de distintos nUmeros de
%burbujas las imagenes.
%llevar a cabo operaciones con Xant y Xact

    if k>0
        %operaciones de calculo de velocidad
    end

%bubbleant=bubble;
%xant=x;
%yant=y;
s(k).x=x;
s(k).y=y;
s(k).Area=[bubble.FilledArea];
s(k).MajorAxisLength=[bubble.MajorAxisLength];
s(k).MinorAxisLength=[bubble.MinorAxisLength];


text(10,10,['fr:' num2str(k)],'Color','Magenta')
M(k)=getframe;
end


movie(M)

%velocidades
```

C.2.1 Program that calculates radial distribution function

This program uses the array s to calculate distances between individual bubbles and the
it calculates the distribution for different radii. The results are averaged in time.

```
\%load results from other programs

load Msingle
rm=mean( sqrt([s(fr).Area]/pi) );
load Msinglets

g_rtemp=[];
rstemp=[]




r1inicial=40;
%load M


for kk=1:5 \%do the calculation with the five centermost bubbles

clear g_r
clear rs



d=dir('*.jpg');



for fr=1:length(s)

\%total image area

    x=[s(fr).x];
    y=[s(fr).y];
    A=[s(fr).Area];

I = imread(d(fr).name);
fr
```

```
\% Mascara is a mask in case there are bad quality image regions.

sizex=size(I,2);
sizey=size(I,1);
porcentajeMascara=1;%default
Area=sizex*sizey*porcentajeMascara;%when a mask is used. see procMascara
r1=r1inicial;
deltar=.25*r1;

Nin=[];

\%this part looks for the centermost bubble
%este ciclo es para buscar la burbuja mAs cercana al centro
    while isempty(Nin)
        A1=pi*r1^2;
        Nin= find( (x-sizex/2).^2+(y-sizey/2).^2<r1^2);

        if not(isempty(Nin))

        centro=Nin(kk);
        xc=x(centro);
        yc=y(centro);
        % ellipse(r1,r1,0,sizex/2,sizey/2)
        % plot(x(centro),y(centro),'r*')

        else
        r1=r1+deltar;
        end

    end


    r2=deltar;
\%here we calculate the distances to the centermost bubble

        distancias=(  (x-xc).^2 + (y-yc).^2  ).^(1/2);

        distancias=distancias( find(ne(distancias,0))  );
        %exclude the test point
```

```
        Numero=round(max(distancias)/rm);
        paso=round(Nmax/N);
        binscenters=1:paso:Nmax;
        binscenters=binscenters*rm;

\%and an histogram is constructed:

        [bins,binscenters]=hist(distancias,binscenters);
        anchobins=binscenters(2)-binscenters(1); areabins=(
        (binscenters+anchobins/2).^2 - (binscenters-anchobins/2).^
        )*pi; %dN/dV/(N/V) g_r(fr,:)=[0
        bins./areabins/(size(x,2)/Area)];



        rs(fr,:)=[0 binscenters/rm];
        %plot(rs(fr,:),g_r(fr,:));



end
figure


 g_rtemp=[g_rtemp;g_r];
 rstemp=[rstemp;rs];
 %plot(mean(rstemp),mean(g_rtemp))
end%kk
%figure

\%results averaged in time.

 plot(mean(rstemp),mean(g_rtemp))
%    load g_racum
%    g_racum=[g_racum;mean(g_r)];
%    save g_racum.mat g_racum
```

C.3 Program that calculates the angles between bubbles

This program saves all the angular measurements between bubbles, using the individual centroid coordinates.

```
clear all
distancias_centro=[];
angulos_centro=[];


load Msingle
rm=mean( sqrt([s.Area]/pi) );
load Msinglets;%M3



d=dir('*.jpg');

if length(s)>100
numfinal=100
else
numfinal=length(s)
end

for fr=1:numfinal

    x=[s(fr).x];
    y=[s(fr).y];
    A=[s(fr).Area];


fr



Nbubbles=length(x)

    for centro=1:Nbubbles
        xx=x(centro+1:length(x));
        yy=y(centro+1:length(y));

       distancias=( (xx-x(centro)).^2 + (yy-y(centro)).^2 ).^(1/2);
       angulos=atan2(yy-y(centro),xx-x(centro));
       %angulos=[angulos(1:centro-1)
       angulos(centro+1:length(angulos))]; distancias=distancias(
       find(ne(distancias,0)) );%exclude the test point
```

```
        %rm=mean( sqrt([s(fr).Area]/pi) );

        distancias_centro=[distancias_centro distancias/rm];
        angulos_centro=[angulos_centro angulos];

    end




end

\%saves in a huge angles database:
save todos_vs_todos.mat distancias_centro angulos_centro
```

C.4 Routine that calculates the conditional angle PDF

```
\%calculate angles with previous program
multiple_angle_histogram


\%builds histograms for different radial range:

[a,b]=hist(angulos_centro(find(distancias_centro>0 &
distancias_centro<=5)),30) ancho=b(2)-b(1) p=a/sum(a)/ancho
figure;plot(b/pi,p,'r-') hold on

[a,b]=hist(angulos_centro(find(distancias_centro>5 &
distancias_centro<=10)),30) ancho=b(2)-b(1) p=a/sum(a)/anch
plot(b/pi,p,'b-.')

[a,b]=hist(angulos_centro(find(distancias_centro>20 &
distancias_centro<=25)),30) ancho=b(2)-b(1) p=a/sum(a)/anch


\%plots the results


plot(b/pi,p,'g--')

axis([-1/2 1/2 0 .8])
```

```
legend('0<r*<5','5<r*<10','20<r*<25')
title('\alpha=0.114')
xlabel('\theta/\pi');ylabel('PDF'); hold off
saveas(gcf,'anglePDF.fig')
```

Bibliography

[1] Arfken, G.B., Weber, H.J.: Mathematical methods for physicists, fourth edition, *Academic Press, Inc*, 1995.

[2] Basset, A.B.: On the Motion of two spheres in a liquid *Proc. Lond. Math. Soc.*,**xviii**, 369, 1887.

[3] Bairstow,L., Cave,B.M., Lang,E.D.: The two-dimensional slow motion of viscous fluids.. *Proc. Roy. Soc.*,**A705**, 394, 1922.

[4] Batchelor, G.K.: An introduction to fluid dynamics. *Second Edition*, Cambridge University Press, 1970.

[5] Biesheuvel, A. and Van Wijngaarden, L.: The motion of pairs of gas bubble in a perfect liquid. *J. Eng. Math.*, **16**, 349–365, 1982.

[6] Blanco Alvarez, A.: Quelques aspets de l'écoulement d'un fluide visqueux autour d'une une bulle déformable: une analyse par simulation directe. *Thése de Doctorat, Inst. Nat. Polytech. de Toulouse.*, Toulouse, 1995.

[7] Blasius, H.: Grenzschichten in Flssigkeiten mit kleiner Reibung, Leipzig, 1907

[8] Bowley, R., Sánchez, M.: Introductory statistical mechanics, *Clarendon Press, Oxford*, Great Britain, 1996.

[9] Brücker C.: Structure and dynamics of the wake of bubbles and its relevance for bubble interaction. *Physics of Fluids*, **11-7**, 1781–1796, 1999.

[10] Bunner, B., Tryggvason, G.: Dynamics of homogeneous bubbly flows. Part 1. Rise velocity and microstructure of the bubbles. *J.Fluid Mech.*, **466**, 17–52,2002.

[11] Bunner, B., Tryggvason, G.: Dynamics of homogeneous bubbly flows. Part 2. Velocity fluctuations. *J.Fluid Mech.*, **466**, 53–84,2002.

[12] Calmet, I.: Analyse par simulation des grandes écheles des mouvements turulents et du transfert de masse sous une interface plane. *Ph. D. Thesis*, Inst. Nat. Polytech. de Toulouse, Fr., 1995.

[13] Canuto, C., Hussaini, M.Y., Quarteroni: Spectral methods in fluid dynamics. *Springer*, 1988.

[14] Clift, R., Grace, R.J. Weber, M.E.: Bubbles, drops and particles. *Academic*,1978.

[15] Crow, S.C.: Lifespan of trailing vortices in a turbulent atmosphere *J. Aircraft.*, **13**, 476–482, 1976.

[16] Currie, I.G.: Fundamental mechanics of fluids. *Second Edition*, McGraw-Hill,1974.

[17] de Vries, A.W.G.: Path and wake of a rising bubble. *Ph.D. Thesis*, University of Twente, 2001.

[18] Duineveld, P.C.: The rise velocity and shape of bubbles in pure water at high Reynolds number, *J. Fluid Mech.*, **292**, 325–332, 1995.

[19] Fabre, J. and Legendre,D.: Ecoulements Diphasiques, *cours ENSEEIHT/INPT, Toulouse, France*, 2000.

[20] Faxen,H.: Der widerstand gegen die bewegung einer starren kugel in einer zahen flussigkeit, die zwischen zwei parallen ebenen wanden eingeschlossen ist. *Ann. Phys.*, **68**,89,1922

[21] Faxen,H.: dissertation, *Arkiv. Mat. Astron. Fys.*, **17 No. 27**, Uppsala Univ., 1921

[22] Happel J., Brenner H., Low Reynolds number hydrodynamics: *Dordrecht: Kluwer Academic*, 1991.

[23] Hicks, W.M.: On the Motion of Two Spheres in a Fluid *Phil. Trans.*, **171**, 455–492, 1879.

[24] Hobson, E.W.: The theory of spherical and ellipsoidal harmonics. , Cambridge University Press, 1931.

[25] Jeffrey, D.J.: Conduction through a random suspension of spheres. *Proc. Roy. Soc.*,**A335**, 355, 1973.

[26] Kang, I.S. and Leal L.G.: The drag coefficient for a spherical bubble in a uniform streaming flow.*Phys. Fluids*, **32**, 233–237, 1987.

[27] Kang, S.A., Sangani, A.S., Tsao, H.-K. and Koch, D.L.: Rhelogy of dense bubble suspensions. *Phys. Fluids*, **9**, 1540–1570, 1997.

[28] Kelley, E., Wu, M.: Path instabilities of Rising Air Bubbles in a Hele-Shaw Cell, *Phys. Rev. Lett.*, **79-7**, 1265–1268, 1997.

[29] Kirchhoff, G.R.: Theorie der Wärme, *Vorles. ü. Math. Phys*, second edition, 229–248, 1894.

[30] Koch, D.L.: Hydrodynamic diffusion in dilute sedimenting suspensions at moderate Reynolds numbers. *Phys. Fluids*,**A(5)**, 1141–1155, 1993.

[31] Kok, J.B.W.: Dynamics of gas bubbles moving through liquid, *Ph.D. Thesis, University of Twente*, 1989.

[32] Kok, J.B.W.: Dynamics of a pair of gas bubbles moving through liquid (Part I). *Eur. J. Mech., B/Fluids*,**12** no. 4, 515–540, 1993.

[33] Kumaran, V. and Koch, D.L.: The effect of hydrodynamic interactions on the average properties of a bidisperse suspension of high-Reynolds-number, low Weber number bubbles. *Phys. Fluids*, **5**, 1123–1134, 1993.

[34] Kumaran, V. and Koch, D.L.: The rate of coalescence in a suspension of high Reynolds number, low Weber number bubbles. *Phys. Fluids*, **5(5)**, 1135–1140, 1993.

[35] Kushch, V.I., Sangani, A.S., Spelt, P.D.M. and Koch, D.L.: Finite-Weber-number motion of bubbles through a nearly inviscid liquid. *J. Fluid Mech.*, **460**, 241–280, 2001.

[36] Lamb, H.: Hydrodynamics. *Sixth Edition*, Cambridge University Press, 1932.

[37] Landweber L. and Miloh, T.: Unsteady Lagally theorem for multipoles and deformable bodies. *J. Fluid Mech.*, **96**, 33–46, 1980

[38] Le, H., Moin, P.: An improvement of fractional step method for the incompressible Navier-Stokes equations. *J. Comp. Phys.*, **92**, 369–379, 1991.

[39] Legendre, D.: Quelques aspects des forces hydrodynamiques et des transferts de chaleur sur une bulle sphérique, *Ph. D. Thesis*, Institut National Polytechnique de Toulouse, 1996.

[40] Legendre, D., Magnaudet, J., and Mougin, G.: Hydrodynamic interactions between two spherical bubbles rising side by side in a viscous liquid. *J. Fluid Mech.*, **497**, 133–66, 2003.

[41] Legendre, D.: A note on the vorticity produced on a clean spherical bubble. *Private communication*, 2006.

[42] Levich, V.G.: The motion of bubbles at high Reynolds numbers.*Zh. Eksptl.*, 1949.

[43] Levich, V.: Physico-chemical hydrodynamics. *New York, Prentice Hall*, 1962.

[44] Lin, T.J., Reese, J., Hong, T. and Fan, S.: Quantitative analysis and computation of two-dimensional bubble columns, *AIChE Journal*, **42(2)**, 301–318, 1996.

[45] Magnaudet, J. and Eames, I.: The motion of high-Reynolds-number bubbles in inhomogeneous flow. *Annu. Rev. Fluid Mech.*, **32**, 659–708, 2000.

[46] Milne-Thomson, L.M., Theoretical Hydrodynamics, *Dover Publications Inc.*, First Edition, New York, 1968

[47] Moore, D.W.: The boundary layer on a spherical gas bubble. *J. Fluid Mech.*, **16**, 161–176, 1962.

[48] Moore, D.W.: The velocity of rise of distorted gas bubbles in a liquid of small viscosity. *J. Fluid Mech.*, **23(4)**, 749–766, 1965.

[49] Mougin.G, Magnaudet,J.: Path instability of a rising bubble, *Phys. Rev. Lett.*, **88-1**, DOI: 10.1103/PhysRevLett.88.014502 , 2002.

[50] Wertheim, M.S.: Exact solution of the Percus-Yevick integral equation for hard spheres, *Phys. Rev. Lett.*, **10-8**, 1963.

[51] Poiseuille, J.L.M.: Recherches expérimentales sur le mouvement des liquides dans les tubes de très petits diamètres, *Mém. des Sav. Étrangers*, **ix**, 1846.

[52] Prandtl, L.: Ueber Flssigkeitsbewegung mit kleiner Reibung. *Vier Abhandlungen zur Hydrodynamik.*, Göttingen, 1927.

[53] Richter, A. and Naudascher, E.: Fluctuating forces on a rigid circular cylinder in confined flow. *J. Fluid Mech.*, **78**, 561–576, 1976.

[54] Risso, F. and Legendre, D.: Velocity fluctuations induced by high-Reynolds-number rising bubbles. *ERCOFTA Bulletin*, **56**, 41–458, 2003.

[55] Rivero, M.: Etude par simulation numérique des forces exercées sur une inclusion sphérique par un écoulement accéleré, *Thése de Doctorat, Inst. Nat. Polytech. de Toulouse*, Toulouse, 1991.

[56] Ryskin, G. and Leal, L.G.: Numerical solution of free-boundary problems in fluid mechanics. *J. Fluid Mech.*, **148**, 1–17, 1984.

[57] Saffman, P.F.: Vortex Dynamics. *Cambridge University Press*, 1992.

[58] Salesse, A., Larue de Tournemine, A., Roig, V.: Development of bubble cluster detection and identification method. *Exp. Therm Fluid Sci.*, **26**, 163–171, 2002.

[59] Sangani, A.S., Zhang, D.Z., Prosperetti, A.: The added mass, Basset, and viscous drag coefficients in nondilute bubbly liquids undergoing small-amplitude oscillatory morion. *Phys. Fluids A*, **3**, 2955–2970, 1991

[60] Sangani, A.S., Didwania, A.K.: Dynamic simulations of flows of bubbly liquids at large Reynolds numbers. *J. Fluid Mech*, **250**, 304–337, 1992.

[61] Sangani. A.S. and Didwania, A.K.: Dynamic simulations of flows of bubbly liquids at large Reynolds numbers. *J.Fluid Mech.*, **250**, 307–337, 1993.

[62] Shew W.L., Poncet S., Pinton J.F., Path instability and wake of a rising bubble, *International conference on Chaos and Non-Linear Dynamics Dynamics Days*, University of Maryland, 2006.

[63] Smereka, P.: On the motion of bubbles in a periodic box. *J.Fluid Mech.*, **254**, 79–112, 1993.

[64] Smythe, W.R.: Flow around a sphere in a circular tube. *The Physics of Fluids*, **4(6)**, 756–759, 1961.

[65] Spelt, P.D.M. and Sangani, A.S.: Properties and averaged equations for flows of bubbly liquids. *App. Sci. Res.*, **58**, 337–386, 1998.

[66] Stokes, G.G.: On some cases of fluid motion *Camb. Phil. Trans.*, **viii**, 1843.

[67] Takemura,F., Magnaudet,J.: The transverse force on clean and contaminated bubbles rising near a vertical wall at moderate Reynolds number. *J. Fluid Mech.*, **495**, 235–253,2003.

[68] Thomson, W. and Tait, P.G.: Treatise on Natural Philosophy, *Nat. Phil.*, 264, 1867

[69] Tzeng, J.-W., Chen, R.C. and Fan, S.: Visualization of flow characteristics in a 2-D bubble column and three-phase fluidized bed. *AIChE J*, **39**, 733, 1993.

[70] Van Wijngaarden, L.: Bubble interactions between bubbles in liquid. *J. Fluid Mech.*, **77**, 27–44, 1976.

[71] Van Wijngaarden, L.: Bubbles interactions in liquid/gas flows. *Appl. Sci. Res.*, **38**, 331–339, 1982.

[72] Van Wijngaarden, L.: On Pseudo Turbulence, *Theoret. Comput. Fluid Dynamics*, **10**, 449–458, 1997.

[73] Van Wijngaarden, L., Kapteijn, C.: Bubble deformation in bubbly liquids and its effect on the stability of voidage waves. In *Mathematical approaches in Hydrodynamics*, Ed. T. Miloh, 38–49, SIAM, 1990.

[74] Van Wijngaarden, L.V.: The mean rise velocity of pairwise-interacting bubbles in liquid, *J. Fluid Mech.*, **251**, 55-78, 1993.

[75] Van Wijngaarden, L: Bubble velocities induced by trailing vortices behind neighbours. *J. Fluid Mech*, **541**, 203–229, 2005

[76] Versteeg, H.K., Malalasekera, W.: Computational Fluid Dynamics *Pearson Education Ltd.*, **6** ,1995. 1995.

[77] Wassgren, C.R.: Vibration of granular materials. *Ph.D. Thesis*, California Institute of Technology, 1997.

[78] Younge, K., Christenson, C., Bohara, A. : A model system for examining the radial distribution function. *Am. J. Phys.*, **72**, 1247–1250, 2003.

[79] Yurkovetsky, Y. and Brady, J.F.: Statistical Mechanics of bubbly liquids. *Phys. Fluids*, **8(4)**, 881–895, 199

[80] Zenit R., Koch, D.L. and Sangani, A.S.:Measurements of the average properties of a suspension of bubbles rising in a vertical channel. *J.Fluid Mech.*, **429**, 307-342,2001.